NASA/TP—2005-214053

Reaction Control System Thruster Cracking Consultation: NASA Engineering and Safety Center (NESC) Materials Super Problem Resolution Team (SPRT) Findings

Rebecca A. MacKay
Glenn Research Center, Cleveland, Ohio

Stephen W. Smith
Langley Research Center, Hampton, Virginia

Sandeep R. Shah
George C. Marshall Space Flight Center, Marshall Space Flight Center, Alabama

Robert S. Piascik
NASA Engineering and Safety Center, Langley Research Center, Hampton, Virginia

December 2005

The NASA STI Program Office . . . in Profile

Since its founding, NASA has been dedicated to the advancement of aeronautics and space science. The NASA Scientific and Technical Information (STI) Program Office plays a key part in helping NASA maintain this important role.

The NASA STI Program Office is operated by Langley Research Center, the Lead Center for NASA's scientific and technical information. The NASA STI Program Office provides access to the NASA STI Database, the largest collection of aeronautical and space science STI in the world. The Program Office is also NASA's institutional mechanism for disseminating the results of its research and development activities. These results are published by NASA in the NASA STI Report Series, which includes the following report types:

- TECHNICAL PUBLICATION. Reports of completed research or a major significant phase of research that present the results of NASA programs and include extensive data or theoretical analysis. Includes compilations of significant scientific and technical data and information deemed to be of continuing reference value. NASA's counterpart of peer-reviewed formal professional papers but has less stringent limitations on manuscript length and extent of graphic presentations.

- TECHNICAL MEMORANDUM. Scientific and technical findings that are preliminary or of specialized interest, e.g., quick release reports, working papers, and bibliographies that contain minimal annotation. Does not contain extensive analysis.

- CONTRACTOR REPORT. Scientific and technical findings by NASA-sponsored contractors and grantees.

- CONFERENCE PUBLICATION. Collected papers from scientific and technical conferences, symposia, seminars, or other meetings sponsored or cosponsored by NASA.

- SPECIAL PUBLICATION. Scientific, technical, or historical information from NASA programs, projects, and missions, often concerned with subjects having substantial public interest.

- TECHNICAL TRANSLATION. English-language translations of foreign scientific and technical material pertinent to NASA's mission.

Specialized services that complement the STI Program Office's diverse offerings include creating custom thesauri, building customized databases, organizing and publishing research results . . . even providing videos.

For more information about the NASA STI Program Office, see the following:

- Access the NASA STI Program Home Page at ***http://www.sti.nasa.gov***

- E-mail your question via the Internet to help@sti.nasa.gov

- Fax your question to the NASA Access Help Desk at 301–621–0134

- Telephone the NASA Access Help Desk at 301–621–0390

- Write to:
  NASA Access Help Desk
  NASA Center for AeroSpace Information
  7121 Standard Drive
  Hanover, MD 21076

NASA/TP—2005-214053

Reaction Control System Thruster Cracking Consultation: NASA Engineering and Safety Center (NESC) Materials Super Problem Resolution Team (SPRT) Findings

Rebecca A. MacKay
Glenn Research Center, Cleveland, Ohio

Stephen W. Smith
Langley Research Center, Hampton, Virginia

Sandeep R. Shah
George C. Marshall Space Flight Center, Marshall Space Flight Center, Alabama

Robert S. Piascik
NASA Engineering and Safety Center, Langley Research Center, Hampton, Virginia

National Aeronautics and
Space Administration

Glenn Research Center

December 2005

Acknowledgments

This paper is the result of considerable effort from a number of dedicated NASA civil servants and support service contractors. The first author would like to thank her coauthors, particularly for their hard work and continuous support throughout this investigation, as well as for their insight into environmental cracking mechanisms. The first author also wishes to acknowledge Mr. Robert H. Titran (retired, Glenn Research Center (GRC)) for sharing his 30 years of refractory metals experience and for being the first to suggest that the thruster cracking was more likely the result of hydrogen embrittlement; Mr. David R. Hull (GRC), Mr. James W. Smith (QSS, GRC), and Mr. Terry R. McCue (QSS, GRC) for their dedication and for their considerable expertise provided during the failure analyses of S/Ns 120 and 132; Dr. Hugh R. Gray and Dr. Michael V. Nathal (GRC) for encouragement and helpful suggestions; Dr. Binayak Panda and Mr. Gregory A. Jerman (Marshall Space Flight Center) for their expertise and technical support during the failure analyses; and Mr. Terence Kelly (Boeing White Sands), Mr. Michael Tarkanian (Boeing Huntington Beach), and Dr. Sherwin Yang (Boeing Rocketdyne) for their cooperation and technical support.

Trade names or manufacturers' names are used in this report for identification only. This usage does not constitute an official endorsement, either expressed or implied, by the National Aeronautics and Space Administration.

Available from

NASA Center for Aerospace Information
7121 Standard Drive
Hanover, MD 21076

National Technical Information Service
5285 Port Royal Road
Springfield, VA 22100

Available electronically at http://gltrs.grc.nasa.gov

Reaction Control System Thruster Cracking Consultation: NASA Engineering and Safety Center (NESC) Materials Super Problem Resolution Team (SPRT) Findings

Rebecca A. MacKay
National Aeronautics and Space Administration
Glenn Research Center
Cleveland, Ohio 44135

Stephen W. Smith
National Aeronautics and Space Administration
Langley Research Center
Hampton, Virginia 23681

Sandeep R. Shah
National Aeronautics and Space Administration
George C. Marshall Space Flight Center
Marshall Space Flight Center, Alabama 35812

Robert S. Piascik
NASA Engineering and Safety Center (NESC)
Langley Research Center
Hampton, Virginia 23681

Summary

The shuttle orbiter's reaction control system (RCS) primary thruster serial number (S/N) 120 was found to contain cracks in the counter bores and relief radius after a chamber repair and rejuvenation was performed in April 2004. Relief radius cracking had been observed in the 1970s and 1980s in seven thrusters prior to flight; however, counter bore cracking had never been seen previously in RCS thrusters. Members of the Materials Super Problem Resolution Team (SPRT) of the NASA Engineering and Safety Center (NESC) conducted a detailed review of the relevant literature and of the documentation from the previous RCS thruster failure analyses of the 1980s. It was concluded from the review that the previous failure analyses lacked sufficient documentation to support the conclusions that stress corrosion cracking or hot-salt cracking was the root cause of the thruster cracking and lacked reliable inspection controls to prevent cracked thrusters from entering the fleet. The NESC team identified new materials characterization and mechanical tests focused specifically on determining (a) the environmental cracking damage mode (root cause) in the niobium RCS thrusters and (b) the likelihood of growth of environmental cracking while in service (after manufacturing). To this end, the NESC team, comprising the NASA Glenn Research Center (GRC), the NASA Langley Research Center (LaRC), and the Marshall Space Flight Center (MSFC) researchers, performed detailed materials characterization on thruster hardware (S/Ns 120 and 132), as well as pertinent testing and characterization of niobium alloy specimens. The NESC team also pursued technical interchanges and conducted testing and evaluations with Safety and Mission Assurance and the Orbiter Materials and Processing group to address concerns with thruster repair and rejuvenation processes at the White Sands Test Facility (WSTF) that have the potential of embrittling the thruster material under certain conditions.

The purpose of this report is to summarize the major findings and to provide the supporting documentation for the RCS thruster cracking consultation by the NESC team. The following findings will be shown and substantiated:

(1) RCS thruster intergranular cracking (IGC) is due to hydrogen embrittlement.

(2) Thruster IGC was produced during manufacturing and was the result of processing the thrusters in the presence of fluoride-containing acids.

(3) Appreciable environmental crack propagation does not occur after manufacturing.

(4) The thruster material was not significantly affected by the sodium hydroxide immersion during the repair and rejuvenation processes at WSTF.

(5) A recommendation was made to audit the thruster repair and rejuvenation processes at WSTF to eliminate steps that have the potential of allowing additional hydrogen uptake and inducing hydrogen embrittlement.

Section 1: Introduction and Background to Thruster Cracking

Thirty-eight primary reaction control system (RCS) thrusters are located in forward and aft positions of each shuttle orbiter. These thrusters are used to provide attitude (pitch, yaw, and roll) maneuvers, as well as translation maneuvers along the orbiter axis. Thruster serial number (S/N) 120 was undergoing a chamber repair and rejuvenation in early 2004 at White Sands Test Facility (WSTF) as a result of coating spallation. After the chamber repair, the chamber and nozzle assembly was electron beam welded to the old injector. During the post-weld, dye-penetrant inspection of the new chamber-to-injector weld, cracks were found in the counter bores and subsequently in the relief radius of the niobium (formerly known as columbium (Cb)) alloy C–103 injector. No cracks had ever been detected before in the counter bore locations, although cracks were detected between 1979 and 1982 in the relief radius of seven injectors (refs. 1 and 2). Figure 1 (ref. 3) is a schematic diagram of a longitudinal cross section of the injector; the locations of the relief radius and counter bores are indicated on opposite sides of the niobium injector flange. The thruster cracking is shown by the dye penetrant indications in figures 2 and 3 (ref. 4) for the counter bores and relief radius, respectively, in S/N 120. It is evident from figure 3 that a large fraction of the circumference of the relief radius was cracked in S/N 120. The initial concern was that hot combustion gases could leak to the outside of the thruster and affect the shuttle orbiter in a Criticality 1/1 (i.e., loss of vehicle with no redundancies) failure mode (ref. 3) if the cracks had propagated entirely through the injector wall to the acoustic cavities.

The prior failure analyses from 1982 concluded that the cause of the relief radius cracking in the RCS thrusters was stress corrosion, as a result of the use of a preweld etchant that contained hydrofluoric acid (HF) and the fit-up stresses from torquing the bolts that secure out-of-flat flanges (ref. 1). The excess etchant was believed to have run through the bolt holes and to have become entrapped in the relief radius, since the mounting flange could not be lifted to adequately rinse the relief radius after the etchant was used. The prior failure analyses also report that the cracks were intergranular all the way to the crack tip, that CbF_3 was present on the crack surface, and that all cracks initiated during manufacturing, specifically during the 316 °C (600 °F)/48-hr air bakeout of the chamber insulation (ref. 1). In this prior investigation, the CbF_3 reaction product was incorrectly identified, and should have been identified as NbF_5 (refs. 5 and 6). The prior failure analyses testing reproduced the IGC in C–103 when the preweld etchant was dried on a niobium test specimen; the specimen was then covered with a titanium plate to entrap the etchant, stressed in tension, and heated to 316 °C (600 °F)/48 hr to simulate the elevated temperature bakeout manufacturing process. It should be noted that the thruster failure was described later as "hot fluoride salt stress corrosion cracking" in a summary article on the RCS thruster failure (ref. 7), although the term "hot salt" was not used to describe the thruster failures in the original failure analysis documentation.

S/N 120 was submitted in its entirety to the M&P organization at Boeing Huntington Beach (HB) for failure analysis in June 2004. The portion of S/N 120 that was set aside for destructive analysis is shown in figure 4 (ref. 4); the remainder of the injector was left intact with the combustion chamber and was used in nondestructive evaluation (NDE) development efforts. The Boeing HB failure analysis (ref. 8) concluded that the injector cracking was intergranular and that the overall appearance of the cracking in S/N 120 was similar to what was described in the failure analyses conducted in the early 1980s. The presence of carbon, oxygen, and fluorine was found on the fracture surfaces, although the age of the cracks could not be determined. The chemical analysis, grain size, and hardness of the bulk material (refs. 4 and 8) met the original material specifications, which are given in table I (ref. 9). In addition, no evidence of overload by ductile rupture or of fatigue rupture was found (ref. 4).

The detailed review of the relevant literature and of the documentation from the previous RCS thruster failure analyses of the 1970s and 1980s provided little evidence in support of stress corrosion cracking (SCC) or hot-salt cracking in niobium alloys. Furthermore, it was concluded that the previous failure analyses lacked sufficient documentation to support the conclusions that SCC (ref. 1) or hot-salt cracking (ref. 7) was the root cause of the thruster cracking. Since a large fraction of the thruster fleet was manufactured during the time when the HF-containing, preweld etchant was used, a large fraction of the thruster fleet is presumed to have cracking damage already present. No reliable NDE technique is currently available for detecting relief radius or counter bore cracking during an in situ examination of the thrusters installed on orbiter vehicles. Thus, the NASA Engineering and Safety Center (NESC) team questioned if the environmental damage mode had been truly identified in the RCS thrusters and if the thrusters could operate safely with environmental cracking damage modes. Specific recommendations were made by the NESC team, which included additional materials characterization and mechanical testing to determine (1) the root cause of the thruster cracking and (2) the likelihood of growth of existing thruster cracks while "in service" (after manufacturing). It should be noted that the Shuttle Program Office agreed with the NESC team recommendations and funded the testing and characterization that supported this work. Researchers at Glenn Research Center (GRC), Langley Research Center (LaRC), and Marshall Space Flight Center (MSFC) performed detailed materials characterization on the thruster hardware and mechanical testing on the niobium C–103 alloy to reproduce the intergranular failure and to

determine if crack propagation was likely. The purpose of this report is to present the major findings and supporting documentation for the RCS thruster cracking consultation by the NESC Materials SPRT.

Section 2: Root Cause Analyses and Testing

2.1 Literature Review

The prior failure analyses from 1982 concluded that the thruster cracking was caused by stress corrosion (ref. 1); this was later described as hot-salt cracking (ref. 7). A detailed literature review was conducted that showed little evidence for SCC or hot-salt cracking in niobium, and in fact, there was an absence of literature on SCC and hot-salt cracking in niobium. The only literature found in an exhaustive search that described SCC in niobium was two papers that described the RCS thruster case from the 1980s (refs. 7 and 10). Discussions with refractory metals experts (refs. 11 to 13) and the review of the literature show that niobium was well known to be susceptible to hydrogen embrittlement (refs. 14 to 28), as well as to interstitial contamination from oxygen and nitrogen. This result provided the impetus for electrochemical testing (see section 2.4) to verify that hydrogen production at niobium surfaces was thermodynamically viable and to determine the environmental conditions under which thruster cracking would likely occur.

Both intergranular stress corrosion and hot-salt cracking require a susceptible grain boundary chemistry, which has not been observed in the literature for niobium. Niobium alloys generally have very homogeneous microstructures and therefore very little variation in chemistry near the grain boundaries would be available to drive a localized corrosion process via SCC or hot-salt cracking. Specifically, grain boundary segregation would need to be present in the form of either grain boundary precipitates or solutes at the grain boundaries for preferential anodic dissolution of material at the grain boundaries to occur (refs. 28 to 31). If segregation at the grain boundaries is not present in a material, SCC or hot-salt cracking would be highly unlikely. Grain boundary segregation can be readily detected by electron microprobe analysis. Therefore, based on the literature review, electron microprobe analysis was required to determine root cause and was incorporated into the characterization plan.

2.2 Electron Microprobe Analyses

Electron microprobe dot maps, line scans, and point analyses were generated to determine the location of specific elements within the intergranular cracks and within the uncracked microstructure. Dot maps enabled broad areas of the microstructure to be analyzed, so that general trends in composition could first be established for numerous locations within the thruster material. Line scans are generally more sensitive to small chemistry variations than dot maps and were used to confirm dot map data across cracks and grain boundaries. Point analyses provide the most quantitative data of these three microprobe techniques and were performed to determine if grain boundary segregation was present, once the general trends were clearly understood.

The following sections of S/N 120 were analyzed by microprobe in order to substantiate root cause of thruster failure: (a) relief radius crack near bolt hole J and uncracked region adjacent to cracking; (b) counter bore and relief radius cracks of bolt hole H and uncracked region adjacent to cracking; (c) small counter bore cracks of bolt hole K and uncracked region adjacent to cracking; and (d) small counter bore cracks of bolt hole M and uncracked region adjacent to cracking. These bolt holes are identified in the injector section that was set aside for failure analysis (fig. 4).

2.2.1 Relief Radius Crack Near Hole J

A large relief radius crack near bolt hole J was selected for initial microprobe examination, and the specific areas (A to E) examined along the crack and away from the crack are indicated in figure 5. The full depth of the intergranular crack in this location is not known because the tip of the major crack was not contained within the cut section provided by Boeing HB. Area dot maps were obtained at magnifications of 200× and 1000× near the relief radius surface (area A), as well as ~1.8 mm (0.07 in.) away (areas B and C) from the surface, in an effort to determine if any qualitative differences in the distributions of elements were present as a function of distance from the relief radius surface. Uncracked areas (near D and E) were also examined to detect the presence of precipitates or higher concentrations of solutes, if any, along grain boundaries away from cracks. Such features, if present, would indicate a predisposition to SCC or hot-salt cracking.

Figure 6(a) shows a backscattered electron (BSE) image of the crack near the surface of the relief radius. BSE imaging clearly delineates the cracks and reveals atomic number differences within the microstructure. The major cracks follow the grain boundaries in the material; finer cracks are also observed to run nearly parallel to the relief radius surface along the grain boundaries beneath the deformed layer from machining. Figures 6(b) to (d) show the dot maps for niobium, hafnium, and titanium, respectively, for the same field of view. The qualitative concentration levels are given for each element in the keys to the right of the figure; the brighter areas in the dot maps indicate more elevated levels of each respective element. Careful examination of figure 6(b) shows that the niobium levels lining the surfaces of the cracks are reduced from the levels within the general microstructure; this result is from the niobium being tied up in the oxide on the crack surfaces. Hafnium and titanium are not evident within

the cracks (figs. 6(c) to (d)). Figures 6(b) to (d) also show that the grain boundaries in uncracked areas are not delineated by the major elements (niobium, hafnium, and titanium). The most prominent feature in figures 6(a) to (d) is the macroscopic banding that occurs for these major elements. It is apparent that slightly elevated concentrations of hafnium and titanium reside in bands wherever the niobium is somewhat leaner, and vice versa. This was consistently observed in other areas of the injector and represents the residual forged macrostructure.

Figure 7 represents the same near-surface area as that presented in figure 6 and contains dot maps for fluorine, carbon, oxygen, and nitrogen. These elements were examined to confirm the presence of elevated levels of fluorine, carbon, and oxygen that were found on the crack surfaces in the prior failure analysis (refs. 4 and 8) and also to examine for the presence of these elements along grain boundaries in uncracked regions, since oxygen and nitrogen are known to cause embrittlement in niobium materials (refs. 11, 12, 14, 16, 18, and 24). Hydrogen cannot be detected by the electron microprobe. Figure 7(a) shows that fluorine is present along the cracked intergranular surfaces and along part of the relief radius surface, as indicated by the bright blue-green levels. Carbon and oxygen are more readily discernable within the crack (figs. 7(b) and (c)). Some of these levels of carbon and oxygen may have been enhanced by the limited infiltration of the mounting medium from the relief radius surface, although carbon and oxygen are also elevated near the crack tip, where infiltration of the mounting medium did not occur. Thus, the elevated levels of carbon and oxygen on the intergranular fracture surfaces in these areas of S/N 120 are consistent with previously reported scanning Auger results (refs. 4 and 8). Elevated levels of nitrogen were typically not apparent along the cracks (fig. 7(d)). It is important to note that the microprobe dot maps do not indicate a presence of fluorine, carbon, oxygen, and nitrogen outside the cracks, since no elevated levels of these elements were observed outside the cracks that were above background levels. Thus, no local segregation of fluorine, carbon, oxygen, and nitrogen was present outside the cracks. Dot maps were also obtained for zirconium, tantalum, and tungsten; these elements were not found within the cracks and were not found to be segregated within the uncracked microstructure.

Similar results were obtained from regions further in from the machined surfaces along the main crack and at terminations of side branches (figs. 8 to 11). Again, niobium levels within the cracks were reduced when compared to the general microstructure, which is the result of niobium oxide on the crack surfaces. Hafnium and titanium were again not found within the cracks. Fluorine, carbon, and oxygen were clearly present along the intergranular cracks to the crack terminations, with oxygen being observed as a continuous film along the entire crack surface. Fluorine and carbon were not consistently observed as a continuous film along the intergranular cracks.

Microprobe line scans were also conducted across relief radius cracks. Line scans provide counts as a function of distance for each element selected and are more sensitive to small variations in chemistry than microprobe dot maps. The line scans were performed normal to the intergranular cracks in polished cross sections so that data could be obtained from within the crack itself and from material just outside of the crack. An example of the position of a typical line scan is indicated by the white arrow superimposed in figure 8(a), and figure 12 provides an example of typical data obtained from such a line scan. Figure 12(a) provides gray scale image counts across the crack that was analyzed; the crack width is indicated in this figure where the gray scale counts drop off precipitously to zero. Figures 12(b) and (c) represent the analyzed data for fluorine and oxygen, respectively, as a function of distance across the intergranular crack. It may be seen that the number of counts for each element increases significantly within the crack relative to background levels. These line scans confirm the dot map data that indicate that higher concentrations of fluorine and oxygen were present within the cracks and that these elements did not extend beyond the cracks into the parent material.

Microprobe dot maps were also obtained in regions far removed from the intergranular cracks to examine the material for the presence of any precipitates or higher concentrations of solutes. Features such as these would indicate that the C−103 may be predisposed to SCC or hot-salt cracking. An example of an uncracked region away from the relief radius crack is shown in figure 13. The BSE image in figure 13(a) delineates several grains in the field of view at a magnification of 1000×. No precipitates or elevated levels of the major elements are evident on the grain boundaries, although a few hafnium oxides are observed within some of the grains. The banded macrostructure is visible, particularly in figures 13(c) to (d), and the hafnium oxides are observed within a hafnium-rich band. Dot maps of fluorine, carbon, oxygen, and nitrogen in figure 14 also reveal no elevated concentrations of these elements above background levels. These results were confirmed in other uncracked regions of S/N 120 near bolt holes H, K, and M.

2.2.2 Hole H Relief Radius

The relief radius in the vicinity of bolt hole H contained several shallow cracks, which were only up to several grains deep in from the surface (fig. 15). These cracks were located near the end of the large relief radius crack indication that was revealed by the dye penetrant inspection in figure 3 for S/N 120. A box superimposed on the image in figure 15 highlights a crack along the injector flange; microprobe analyses were performed on this area to determine if shallow cracks yielded

similar results to those obtained on deeper cracks (i.e., near hole J). The selected crack in figure 15 completely surrounded a grain which subsequently fell out during metallographic polishing. The void that was left behind enabled a unique opportunity for the analyses of broad surfaces of grain boundaries. Figures 16(a) to (d) show the BSE image for the analysis area and the dot maps for fluorine, oxygen, and carbon, respectively. It is evident from these data that high concentrations of fluorine, oxygen, and carbon were present on the broad grain boundary surfaces of the shallow crack, which is consistent with the results from the polished cross sections of the deep relief radius crack near bolt hole J. Microprobe line scans also confirmed the presence of elevated levels of fluorine and oxygen within the shallow intergranular cracks.

2.2.3 Hole K Counter Bore

Dye penetrant results from reference 4 indicated that the counter bore of hole K was crack free. However, scanning electron microscopy revealed the presence of numerous small cracks (up to 30 µm (0.001 in.) deep) along the counter bore surface of hole K; these were the most shallow cracks observed in S/N 120. These shallow cracks extended through the ~8 µm (0.0003 in.) thick, cold-worked machining layer at the surface. Some cracks proceeded inward along grain boundaries, as in figure 17(a), while other cracks proceeded inward along a transgranular path through grain interiors (fig. 17(b)). Microprobe dot maps revealed that both the intergranular and transgranular cracks were oxidized, as evidenced by the higher concentrations of oxygen along the crack surfaces, compared to that within the uncracked microstructure (fig. 17(c)). However, based on an analysis of 10 individual cracks, none of these cracks were observed to contain fluorine. An example of this is shown in figure 17(d). The reason for the consistent lack of fluorine in these shallow counter bore cracks is not known. It may be speculated that these shallow cracks did not result from exposures to HF during manufacturing but instead resulted from exposure to another source of hydrogen. A lack of fluorine was also exhibited by C–103 specimens believed to have been embrittled by hydrogen during C-ring testing (section 2.3). In contrast, the significantly deeper counter bore cracks in S/N 120 from holes M (ref. 4) and H, for example, did contain significant concentrations of fluorine, carbon, and oxygen on the intergranular crack surfaces. So in general, it may be stated that the IGC in the counter bores had similar features to those in the relief radius, except for the very shallow (~30 µm (0.001 in.)) counter bore cracks.

2.2.4. Quantitative Point Analyses

Uncracked regions of S/N 120 were examined quantitatively for the determination of chemical segregation, if any, to the grain boundaries. Electron microprobe data were obtained using point analyses in the vicinity of the relief radius and counter bore of bolt hole J, the counter bore of bolt hole K, and the relief radius and counter bore of bolt hole M. Figure 18 shows a representative area examined in the counter bore region of bolt hole K; an overall grain size of ~50 µm (0.002 in.) is evident in the field of view. Superimposed on the image in figure 18 are the specific locations that were used for the point analyses obtained from 20 grain boundaries and 20 neighboring grain interiors. The means and 95 percent confidence intervals of the levels of the major elements, niobium and hafnium, are presented in figures 19(a) and (b), respectively. The means for the grain interiors and the grain boundaries are indicated in the figures by the filled circles and unfilled squares, respectively. It is evident in figures 19(a) and (b) that the major element levels in the grains and along the grain boundaries are nearly identical and that their confidence intervals overlap. Thus, the data clearly indicate that the compositions of the major elements are statistically equivalent for the grain boundaries and grain interiors.

Figure 19(c) shows the compositional levels for the minor elements and interstitials from the same region of the hole K counter bore. The data clearly indicate no difference in the carbon, zirconium, titanium, oxygen, and tantalum contents between the grain interiors and the grain boundaries. Tungsten was not specifically examined in this sample because the element was not found to segregate in other areas of S/N 120. Additionally, fluorine and nitrogen were examined but were not detected in any of the uncracked regions and thus were not included in the plot. The analyzed levels for carbon and oxygen are higher than those obtained from the C–103 bulk chemical analyses, because the microprobe standards for carbon and oxygen were not within the range of these interstitials in C–103. To obtain more appropriate standards for carbon and oxygen would have required the procurement and analysis of additional standards, and this was beyond the scope of this particular investigation. However, the determination of relative differences in carbon and oxygen between grain boundaries and grain interiors is sufficient for the identification of grain boundary segregation. The results demonstrate that there is no difference between the chemistries of the grains and grain boundaries in the injector material. Additional point analyses data from the relief radius and counter bore of bolt hole J and the relief radius and counter bore of bolt hole M substantiated the results from the counter bore of hole K. Thus, the major, minor, and interstitial elements are not segregated within the C–103 thruster material, and therefore, cracking by intergranular stress corrosion or by hot-salt cracking is highly unlikely.

2.2.5 Summary and Conclusions for Microprobe Analyses

Cracking by intergranular stress corrosion or by hot-salt cracking is highly unlikely, because no grain boundary segregation was present in the thruster material. As a result, the root cause identified in the prior failure analyses (ref. 1) and

subsequent reviews (refs. 7 and 10) of the thruster case study cannot be substantiated by the current work.

(1) The C−103 thruster material was determined to be homogeneous, and no grain boundary precipitates were observed.

(2) Quantitative data obtained from over 100 data points from relief radius and counter bore regions show that the concentrations of the elements at the uncracked grain boundaries were statistically equivalent to those within the grain interiors.

(3) Electron microprobe data from dot maps, line scans, and point analyses indicate that oxygen, carbon, and fluorine were present within the intergranular cracks, which is consistent with the Auger results from Boeing HB (refs. 4 and 8).

(4) No elemental segregation was observed in the parent material ahead of the crack tips.

2.3 Testing Attempts to Reproduce Hot-Salt Cracking

2.3.1 Testing Procedure

One of the root causes reported in a review article to be responsible for the IGC observed in the niobium injectors was termed "hot-salt cracking" (ref. 7). In the fall of 2004, Boeing Rocketdyne made an attempt to reproduce hot-salt cracking in the laboratory on C−103 test coupons (ref. 32). This approach was intended to introduce hot fluoride salts to the niobium material while precluding the introduction of hydrogen. C-ring test specimens were machined and prepared by dipping their preloaded tensile surfaces into molten NbF_5 at 93 °C (200 °F). Since NbF_5 is hygroscopic (ref. 32), the hot-salt application was performed in an argon glove box. Samples were cooled to ambient temperature and were exposed isothermally in air for 48 hr at temperatures of 149, 235, and 316 °C (300, 455, and 600 °F) under stresses ranging from 103 to 207 MPa (15 to 30 ksi). The 149 and 235 °C (300 and 455 °F) temperatures were selected for C-ring testing because they represent typical injector temperatures in the vicinity of the cracking, with 235 °C (455 °F) being the maximum under normal operating conditions; 316 °C (600 °F) was selected to simulate the 48-hr insulation bakeout that thrusters undergo during manufacturing. Optical and scanning electron microscopy (SEM) was performed at Boeing Rocketdyne on the C-ring samples, and residue from the C-ring surfaces was collected and analyzed by x-ray diffraction. Microscopy revealed shallow IGC only in the 316 °C/207 MPa (600 °F/30 ksi) specimen. X-ray diffraction identified the specimen surface residue to be NbO_2F, which was reported to have resulted from a chemical reaction between NbF_5, oxygen, and residual moisture in the air (ref. 32). Boeing Rocketdyne requested that GRC conduct microprobe analyses on their tested specimens. The remainder of this section will describe the results generated at GRC.

2.3.2 Microstructural Examination

All of the C-ring specimens tested at 149, 235, and 316 °C (300, 455, and 600 °F) were metallographically prepared and examined by SEM. It was confirmed that IGC was present only in the 316 °C/207 MPa (600 °F/30 ksi) specimen, and an example of the morphology of the cracks is given in figure 20. As may be seen in the figure, the cracking was shallow with most cracks observed to extend up to a depth of only about two grains (~50 μm (0.002 in.)) in from the surface. Additional cracks are also observed to run parallel to the surface, beneath the cold-worked layer from machining. Depth profiling of the IGC was performed by controlled polishing iterations, each of which removed 0.25 mm (0.01 in.) of material. Scanning electron microscopy was performed after each of three polishing iterations to determine the depth and location of cracks. It was found that each iteration removed the previously observed cracks and revealed new cracks in different locations, which demonstrated that the intergranular cracks were neither deep (in from the surface) nor long (into the plane of polish). The one exception to this was a single crack that intercepted the saw cut along the specimen edge; this crack was considerably deeper (~600 μm (0.024 in.)) than all of the other cracks and was considerably longer since it was observed after each polishing iteration. It is interesting to note that all of the cracks observed were located within 2.4 mm (0.094 in.) from the cut ends of the specimen (fig. 21), which may suggest that the affected material became cracked under the action of the cutting process at Boeing Rocketdyne. Otherwise, some cracks should have initiated along the tensile surface in the middle of the specimen.

Electron microprobe dot maps and point analyses were obtained from polished cross sections of the 316 °C (600 °F) C-ring specimen. Figure 22(a) shows a typical, surface-connected crack in the 316 °C (600 °F) specimen, and dot maps for fluorine, carbon, and oxygen from the same specimen area are presented in figures 22(b) to (d), respectively. Again, brighter regions in the dot maps are indicative of higher concentrations of that element. Although elevated levels of fluorine reside on the specimen tensile surface from the fluoride salt that was originally deposited on it, it is clear that neither fluorine nor carbon is observed within the crack. This is a very different result from that obtained with the intergranular cracks in S/N 120, where fluorine and carbon were readily detected within the intergranular cracks. The lack of fluorine and carbon in the C-ring specimen was verified by other dot maps that were obtained from deeper cracks in the C-ring specimen and from other portions of this same crack located further away from the surface. In contrast, elevated levels of oxygen are consistently observed within the C-ring cracks and along the specimen tensile surface, as seen in figure 22(d).

To confirm the comparative levels of carbon, fluorine, and oxygen within the C-ring test specimens, a point analysis technique was also performed by microprobe. This technique involves the accumulation of counts for a specific element over a 10-sec duration at each location examined. Count rates obtained from the 316 °C (600 °F) C-ring specimen are displayed in figure 23 for several locations within a crack near a triple point, in the C−103 adjacent to the edge of the crack, and away from the crack within the C−103 parent material. Background count rates at the carbon, fluorine, and oxygen peak positions were also obtained within the C−103 parent material for comparison. The count rate data confirm the dot map results; carbon and fluorine were not evident within the C-ring cracks, although elevated levels of oxygen were again found within the C-ring cracks. This is unlike the thruster cracks that were shown in sections 2.2.1 and 2.2.2 to contain elevated levels of carbon, fluorine, and oxygen. To demonstrate that this point analysis technique was capable of detecting carbon and fluorine, if present, count rates were also collected for an intergranular crack from S/N 120. These data are presented for comparison in figure 24; it is clearly evident that elevated levels of carbon, fluorine, and oxygen were able to be detected by this technique within the S/N 120 crack. Hence, based on polished cross sections of the C-ring cracks, fluorine was not evident within the intergranular cracks, even though fluoride salts were applied directly to the C−103 tensile surface.

Although most intergranular cracks were very shallow in the 316 °C (600 °F) C-ring specimen, a sizeable crack (~600 μm (0.024 in.) deep) was intercepted along the specimen cut end. This crack was deep enough to fracture open in order to view any products present on the intergranular surface. The opened crack is shown in figure 25(a), and a higher magnification of the grains is given in figure 25(b). The higher magnification shows a relatively clean-looking fracture surface, which appears to have no reaction products present. A typical Energy Dispersive Spectroscopy (EDS) scan obtained from the C-ring fracture surface is displayed in figure 25(c); the scan shows high niobium peaks and a sizable hafnium peak, which represent the major elements in C−103. The oxygen peak observed is small and barely discernable above background levels, which is typical of baseline C−103. No fluorine peak is evident, and this result was confirmed in numerous locations. For comparison, figures 26(a) to (c) display intergranular crack surfaces, as well as a representative EDS scan, obtained from S/N 120. It is clearly evident in figure 26(b) that the S/N 120 fracture surfaces contain numerous reaction products, including nodules that resemble opened popcorn kernels, as well as layers of oxide scale. A typical EDS scan in (fig. 26(c)) shows significant chemistry differences compared to the 316 °C (600 °F) C-ring specimen described above. S/N 120 fracture surfaces typically exhibit high oxygen peaks, as well as a noticeable fluorine peak, in addition to peaks for niobium and hafnium.

The fractography conducted on the opened crack surfaces from the C-ring test specimen and S/N 120 demonstrates the significant differences between the laboratory-tested material and the flight hardware. These are important distinctions because the cracking in the C-ring test was used to infer crack initiation by hot-salt cracking in S/N 120 (ref. 33). However, the absence of fluorine-containing reaction products on the C-ring cracks does not support the hot-salt cracking mechanism. Instead, the C-ring testing provides support for hydrogen embrittlement, because the crack surfaces do not contain reaction products, similar to those from hydrogen-assisted cracking (ref. 34). Although the initial intent of these tests was to introduce a salt (NbF_5), while eliminating all sources of hydrogen, the elevated temperature exposures were performed in laboratory air. As a result, the NbF_5, which is a highly hygroscopic compound (ref. 32), appears to have absorbed water, thereby providing a source of hydrogen to affect the mechanical behavior of the C−103 material. Thus, the C-ring testing and the detailed microprobe analyses did not substantiate the root cause identified in review articles (refs. 7 and 10) of the RCS thruster case history. Further evidence that supports hydrogen embrittlement being the root cause of the IGC in the RCS thrusters will be provided in sections 2.4 and 2.5. Section 2.4 will present electrochemical characterization data showing that hydrogen production in C−103 is thermodynamically assured in the presence of HF-containing etchants. Section 2.5 will demonstrate through mechanical testing and resultant fractography that intergranular failure is observed in niobium materials when charged with appropriate levels of hydrogen.

2.3.3 Summary and Conclusions From C-Ring Testing

The C-ring test results did not support the hot-salt cracking mechanism, which was identified in review articles (refs. 7 and 10) as being the root cause of the IGC in the RCS thrusters. Instead, the C-ring test specimens had fracture surfaces with characteristics similar to those from hydrogen-assisted cracking.

2.4 Electrochemical Characterization

Based on the results from the literature review, the IGC observed in the RCS thrusters was most likely due to environmentally assisted cracking that was initiated during the processing of these components. To better understand the chemical interactions that may have affected the mechanical behavior of these components, a series of electrochemical characterization tests were developed. These tests consisted of open circuit measurements and the development of polarization

curves, which can be used to determine the electrochemical reactions that were likely to occur during the processing of the RCS thrusters when the C−103 is exposed to a specific environment. In addition, electrochemical scratch tests were used to interrogate the electrochemical processes that occur on a material as the native oxide is ruptured, which is a necessary process to produce environmentally assisted cracking in materials, such as niobium, that develop a native oxide. Once the likely electrochemical processes and the test conditions that create these processes are identified, exposure conditions for representative mechanical tests can be created.

The critical environment appears to be produced by the niobium etchant used during processing. This etchant consisted of HF, HNO_3, and H_2O in equal proportions. Niobium and niobium alloys are known to be attacked by HF (refs. 18 and 35 to 37) but are resistant to HNO_3 (refs. 18 and 35) due to the formation of an adherent oxide film. Consequently, a dilute HF solution was used in the electrochemical characterization tests, instead of the niobium etchant, in order to isolate the effects of the HF and to simulate the dilute acid condition that would be anticipated to collect in occluded regions of the injector after rinsing with water. In these characterization tests, HF was diluted to a pH ≈ 3.5. A neutral solution (1 wt% sodium chloride (NaCl) in H_2O) was also evaluated to compare the response of the C−103 material in a relatively benign environment to that observed in the dilute HF solution.

All C−103 specimens were extracted from a partially machined injector that was manufactured during the same approximate timeframe as injectors that have seen service on the shuttle orbiters. The Ti-6Al-4V specimens were extracted from a flight hardware flange that was bolted to thruster S/N 120. The Ti-6Al-4V was included in the testing to determine if the couple created from the Ti-6Al-4V flange contacting the C−103 thruster was likely to affect the electrochemical processes occurring on the exposed C−103 surfaces.

2.4.1 Open Circuit Measurements

Electrochemical tests were initially performed to obtain open circuit measurements of C−103 and Ti-6Al-4V; values of the open circuit potential (E_{OC}) dictate what electrochemical processes can occur on each material containing a native oxide, excluding any outside influences. The Ti-6Al-4V component was black in color due to the production of a thick oxide film that developed during processing. Open circuit potentials were obtained for the Ti-6Al-4V with this thick oxide film and for Ti-6Al-4V with an air-grown film produced after polishing the specimen. Electrochemical testing indicated little difference in the open circuit potentials for the titanium alloy with either oxide film, and thus all testing for Ti-6Al-4V was performed subsequently on specimens that were polished to a 600-grit finish. After removal of the oxide film, specimens were immediately immersed in the selected electrochemical solution, and testing was begun. Additional tests were performed using a deaerated solution to determine if there was an effect observed from the removal of dissolved oxygen in the electrolyte; deaeration was obtained by bubbling argon through the solution for at least 30 min prior to the introduction of the specimen. However, it was found that the state of aeration had little effect on the open circuit potential for either material in the solutions examined. Thus, all results presented will be for aerated solutions. In addition to the measurement of open circuit for each material, couple potentials were also measured by electrically coupling samples of each material and immersing them into the selected solution. For the couple measurements, the C−103 and Ti-6Al-4V specimens were sectioned to expose nearly equal surface areas of each material to the solution. All open circuit measurements were made by measuring the specimen potential relative to a saturated calomel electrode (SCE).

The E_{OC} data are provided in table II for C−103, Ti-6Al-4V, and the C−103/Ti-6Al-4V couple in aerated solutions of dilute HF and of 1 wt% NaCl in H_2O (neutral solution). The reversible potentials (E_r) for water reduction for each of the aerated electrolytes are also given in table II. The values of E_r represent the potential at which the reduction of water will produce a hydrogen fugacity of 1 atmosphere (ref. 38). For potentials less than E_r, the fugacity will be greater than 1 atmosphere. Comparison of the data in the table shows that the open circuit potentials for C−103, Ti-6Al-4V, and the couple in the dilute HF solution are more negative, or more cathodic, with respect to the E_r for water reduction in the dilute HF solution. However, the open circuit potentials in the neutral NaCl solution are more positive, or more anodic, relative to the E_r for water reduction in the neutral solution. This suggests that hydrogen is more readily produced, via the reduction of water, on the surface of each material in the dilute HF solution than that which will be produced in a neutral solution. Table II also shows that the E_{OC} for Ti-6Al-4V is 0.598 V cathodic to the E_{OC} measured for the C−103 in the dilute HF solution, which suggests that a greater amount of hydrogen can actually be produced on the surface of the Ti-6Al-4V than on the C−103 surface in the dilute HF solution. When the Ti-6Al-4V is coupled to the C−103 material, the E_{OC} is observed to lie between the E_{OC} values for each separate material. This suggests that if the Ti-6Al-4V is coupled to the C−103 component, a greater amount of hydrogen production may occur on the surface of the C−103 material than if the Ti-6Al-4V flange were not present.

2.4.2 Electrochemical Scratch Testing

Niobium and titanium alloys produce a native oxide in the presence of oxygen and/or water. Consequently, electrochemical tests generally interrogate these oxide films and do not result in a complete understanding of the reactions that occur on the base material. This is of particular concern when addressing environmentally assisted cracking events, since the

native oxide may be breached in service due to mechanical rupture or abrasion of the film and the critical electrochemical processes that may affect material behavior may be exacerbated when the film is ruptured. To interrogate such a situation, C−103 specimens were prepared in metallographic mounts. One surface of the mounted specimen was polished through 600 grit to provide a fresh surface of the C−103 coupon. Conductive wires were spot welded to the back of C−103 specimens. The polished surface was then coated with a nonconductive film and immersed in either the dilute HF or the 1 wt% NaCl solution. The location of the spot weld was such that it would not be exposed to the electrolyte. The nonconductive film and native oxide were then ruptured with a diamond scribe to expose fresh base metal to the solution. A high-speed data logger (250 Hz) was used to acquire potential versus time data during the scribing of the surface. By measuring the potential transient created, a better understanding can be obtained of the electrochemical processes occurring at the crack tip as the oxide film is ruptured during crack growth.

The potential transients obtained from the scratch tests of the C−103 material in the dilute HF solution are shown in figure 27. Because this test measures a rapid transient in behavior, a minimum of three measurements was performed for each test condition to ensure that an accurate representation of the electrochemical process was obtained. The average scratch potentials for C−103 immersed in the dilute HF and the neutral NaCl solutions are given in table III; scratch potentials ($E_{scratch}$) represent the minima observed in the curves in figure 27. The $E_{scratch}$ for C−103 were found to be more negative, or more cathodic, compared to the E_{OC} for the C−103 in the same electrolyte. The measured scratch potentials suggest that hydrogen can readily form on the fresh surface of C−103 as the oxide film is ruptured. Hydrogen production can be quantified by calculating the hydrogen fugacity (f_{H_2}) for a given potential, as shown in equation (1) (ref. 38).

$$\log\left(f_{H_2}\right) = -\frac{E - E_r}{30} \tag{1}$$

where E is either the measured E_{OC} or the measured $E_{scratch}$, and E_r is the reversible potential for the reduction of water. Values of potential in equation 1 are in units of millivolts (mV) and fugacity is in atmospheres. The fugacities calculated for the scratch potential and open circuit potentials for C−103 in the dilute HF and 1 wt% NaCl are also provided in table III. The resulting fugacity at a bared C−103 surface is shown to be more than 15 orders of magnitude greater that on the native oxide surface for either solution.

In summary, it has been shown that the open circuit potentials for both the Ti-6Al-4V material and the C−103/Ti-6Al-4V couple are cathodic in the dilute HF solution, with respect to the open circuit potential for the C−103 material. The couple potential suggests that cathodic processes and hydrogen production can occur on the C−103 surface in the presence of the Ti-6Al-4V flange that may not occur without this flange or at distances sufficiently far away from this flange to be unaffected by the couple. However, when the native oxide is ruptured, the electrochemical processes in both the dilute HF and the NaCl solutions are highly cathodic, relative to the processes operative with an intact native oxide. Furthermore, the measured scratch potential is similar in sign and magnitude to that of the open circuit potential for the C−103/Ti-6Al-4V couple. Consequently, if the native oxide becomes ruptured in service, the Ti-6Al-4V flange does not need to be present nor involved in the electrochemical processes for hydrogen production to occur and affect the environmentally assisted cracking in the C−103 thrusters.

2.4.3 Electrochemical Polarization

To determine the overall electrochemical behavior for the C−103 material, polarization curves were generated. By evaluating the electrochemical response over a large range in potential, a better understanding of how electrochemical processes are affected by outside influences, such as coupling a piece of C−103 to Ti 6Al-4V or rupturing the oxide film from a niobium alloy, can be determined. Here, two measurements (one cathodic and one anodic with respect to the open circuit potential) were acquired for each solution in the aerated condition. The tests consisted of polishing a specimen to a 600-grit finish, exposing the specimen to the selected solution, allowing an open circuit condition for 1 hr, and then performing a controlled potential scan at a rate of 0.167 mV/sec, while monitoring the current. For each anodic scan, the initial potential was set to be 40 mV cathodic to the open circuit potential, while the cathodic scan was initiated at 40 mV anodic to the open circuit potential. These starting conditions for the electrochemical scans made it possible to have a small section of data from each test under the same conditions, which was used to validate the results.

The polarization curves acquired in the dilute HF and the neutral (1 wt% NaCl in H_2O) solutions are compared in figure 28. Here, the open circuit potentials (approx. −0.4 to −0.6 V_{SCE} in fig. 28) are approximated by the lowest measured current values. All data at higher values of potential indicate anodic processes (i.e., dissolution and oxidation), while all data at lower values of potential indicate cathodic processes (i.e., water reduction). A large passive region is shown to start with a "knee" in the data at approximately −0.25 V_{SCE}, and the passive region remains stable with no significant increase in current for more than 2 V in potential, suggesting a protective passive film is present over a large range of potential. However, it should be noted that the current density throughout the passive region is more than 1 order of magnitude higher in the HF solution than for the neutral solution, indicating significant anodic processes are occurring throughout the passive region. Comparison of the two polarization curves in figure 28 also

reveals a higher exchange current density (i_o) and a lower E_{OC} are observed in the HF solution compared to that in the neutral solution. This indicates that the C−103 material is more electrochemically active in an HF solution than in the neutral aqueous solution. In the cathodic region in figure 28, the current density is slightly higher in the HF solution; however, the shapes of the two curves are similar, suggesting similar cathodic processes (i.e., water reduction) will occur in either of the two solutions.

The polarization curve generated for the C−103 exposed to the dilute HF solution has been isolated in figure 29 for further discussions. The current values cathodic to the E_{OC} are observed to be much higher than in the anodic region, suggesting a larger rate of reaction for cathodic reactions compared to the anodic reactions. The values of the open circuit and scratch potentials have also been superimposed in figure 29. These results indicate that at the open circuit (at least near the titanium flange) and scratch potentials in this system, cathodic processes are expected to dominate the electrochemical processes of this system. This observation implicates the role of hydrogen in the environmentally assisted cracking processes observed for the thruster components. These electrochemical tests clearly show that atomic hydrogen is readily produced on the bared C−103 surfaces exposed to aqueous solutions. Additionally, the relatively high cathodic currents in figure 29 indicate that the amount of hydrogen that can be produced via water reduction may be significant. While these characterization tests demonstrate that atomic hydrogen is readily formed on the surface of the C−103 material, the tests do not shed any light on how this hydrogen production may affect the C−103 material. For example, it would be instructive to determine if the hydrogen being produced readily adsorbs onto the C−103 surfaces, then absorbs into the material and diffuses into the bulk (ref. 39). Therefore, mechanical screening tests were subsequently performed to determine how the C−103 material behaves when it is charged with hydrogen.

2.4.4 Summary and Conclusions for Electrochemical Characterization

Hydrogen can readily form on the surface of the C−103 thrusters when exposed to an HF-containing etchant. The hydrogen is produced via the water reduction reaction. The driving force for hydrogen production is very high on the surface bared of the native oxide film.

(1) The presence of HF increases the electrochemical activity of C−103.

(2) C−103 is not susceptible to rapid dissolution, even in dilute HF solutions. However, the presence of dilute HF can result in increased electrochemical processes.

(3) The production of H is thermodynamically assured on the surface of bared C−103 when moisture is present.

(4) Coupling Ti-6Al-4V to C−103 may increase the production of hydrogen in dilute HF relative to the amount of hydrogen produced on C−103 without titanium being present.

(5) The hydrogen fugacity on a bared C−103 surface in dilute HF is ~2×10^{15} atm.

2.5 Environmentally Assisted Cracking (EAC) Screening Tests

A series of uniaxial tension and bend tests were designed to determine how the exposure to environment and temperature can affect the mechanical behavior of the C−103 material. All uniaxial tension specimens were run by exposing the specimen to a dilute etchant solution and applying a constant potential. Each potential was selected based on the electrochemical tests presented in section 2.4. By applying a constant potential to the test specimen, the electrochemical processes for each test can be controlled so that specific damage processes can be evaluated. These tests are designed to screen specific environmentally assisted cracking processes (i.e., dissolution-based SCC or hydrogen embrittlement). Once these processes were understood, bend specimens were designed that more accurately reflect the loading and exposure conditions observed in service. Mechanical test specimens were obtained from a partially machined injector (see fig. 30) that was manufactured during the same approximate time frame as injectors that have seen service on the shuttle orbiters.

2.5.1 Uniaxial Tension Testing

Uniaxial tension specimens were machined with a gage section measuring approximately 5.1 by 5.1 mm (0.2 by 0.2 in.), as seen in figure 31. The specimens were notched with a brass wire via electron discharge machining (EDM) in order to provide a local stress concentration at the midsection of each specimen. The notch was machined across the width of one face and measured between 0.5 and 0.63 mm (0.02 and 0.025 in.) in depth. Each test specimen was placed in an electrochemical cell with the gage section submersed in a dilute HF solution (diluted to a pH ≈ 3.5), while the threaded specimen ends were outside of the solution and placed into an adaptor of a load frame. With this testing setup, the specimen gage section could be within an electrochemical cell while being stressed under constant load. A reference and platinized counter electrode were also immersed within the solution of the electrochemical cell. The reference electrode, counter electrode, and specimen were connected to a potentiostat to allow each test to be performed under a constant potential condition. Durations of exposure were selected at 24, 48, and ~90 hr, although some specimens failed during exposure under applied load. A list of testing conditions is provided for each specimen in table IV. Due to the low conductivity of the test solution, 1 wt% NaCl was added to the test solution initially to

ensure that the desired electrochemical potential was in fact the potential generated at the surface of the test specimens. There were no significant differences between the tests conducted with or without the NaCl.

The range of potentials examined was based on the electrochemical tests described in the previous section (see fig. 29). As seen in table IV, several tests were performed with the applied potential between –600 mV_{SCE} and –1 V_{SCE}. These values of potential were selected to interrogate the effect of cathodic processes on the mechanical behavior of C–103. The scratch potential should be the most cathodic potential established on the surface of the thruster material, unless it is affected by an outside influence not considered in this study. Thus, initially tests were performed at –900 mV_{SCE}, which is slightly cathodic to the measured scratch potential in the dilute HF solution (see fig. 27). Then the potentials were increased toward E_{OC} until little to no embrittlement was observed. At –600 mV_{SCE}, there was limited embrittlement, and as a result, no additional cathodic potentials were selected near this range. However, an additional test was performed at –100 mV_{SCE} to examine the potential for aqueous dissolution-based SCC. The potential of –100 mV_{SCE} was determined based on the anodic polarization of C–103 (see figs. 28 and 29). Here, –100 mV_{SCE} is slightly anodic to the passive knee, which is considered to be a region that is highly susceptible to SCC (ref. 40). In addition to examining the influence of the etchant solution, the potential effects of the thermal bakeout used in the manufacture of the thruster components (316 °C (600 °F) for 48 hr) was studied by removing several of the exposed specimens from the electrochemical exposure cell and placing them into air furnace under load. Upon completion of these tests, all specimens were strained to failure, and examination of the fracture surfaces was subsequently conducted using SEM.

Two of the test specimens (specimens 1 and 2) failed during the exposure process, as indicated in table IV. These test specimens exhibited highly embrittled fracture surfaces with little observed ductility, an example of which is given in figure 32. Smooth terrace features along with visible slip bands and fluted features are clearly visible in figure 32(b), indicating a predominantly cleavage fracture. Although there was some IGC visible on this fracture surface, the predominant fracture process was transgranular cleavage, which is distinctly different from the intergranular fracture observed in service. Specimen 2 was statically loaded to approximately 177 MPa (25.6 ksi), with an applied potential of –750 mV_{SCE}, and failed after only 26.5 hr. Similar failures were observed for specimen 1, which had an applied stress of approximately 198 MPa (28.8 ksi) and an applied potential of –900 mV_{SCE}; failure occurred in this specimen in less than 40.5 hr. As the exposure time was decreased for the same applied potential (specimen 3 in table IV) or the potential was increased to more anodic potentials (–600 mV_{SCE} for specimen 4 in table IV), the fracture surfaces suggested that the outer specimen surfaces were less ductile than the central portion of the specimens. However, there were no indications of intergranular or cleavage fracture, thereby indicating only a moderate embrittlement was induced from the exposure process for specimens 3 and 4. It should be noted that specimen 4 was also baked out prior to mechanically overloading the specimen. This bakeout was not performed for specimens 1 through 3, and the potential effects of the bakeout process will be discussed below for specimens 5 through 9. Although the distinct change in fracture mode observed for specimens 1 and 2 suggest that these specimens were readily embrittled by the absorption of hydrogen into the C–103 material, the cleavage fracture morphology produced in these tests did not resemble the intergranular fracture produced in service. Consequently, additional tests were performed to fully characterize the damage processes experienced during the processing of the cracked thruster components.

Five test specimens were examined by exposing the specimens to the dilute HF solution at –1 V_{SCE} for 90 hr either using a small tensile load (specimens 5 and 6) or zero load during exposure (specimens 7, 8, and 9), as seen in table IV. Predominantly brittle fracture was observed when these specimens were strained to failure following exposure (specimens 5, 7, and 8), while predominantly ductile fracture was observed (specimen 6) if the exposure was followed by a heat treatment of 316 °C (600 °F) for 17 hr. Specimen 9 had a relatively small region (~0.25 mm (0.01 in.)) around the outer periphery of the specimen gage that exhibited 100 percent IGC, while the majority of the fracture surface was ductile (see fig. 33). These features on the fracture surfaces suggest that hydrogen was absorbed within the bulk of the specimens during the –1 V_{SCE} exposures and that the hydrogen was highly mobile in the C–103 material even at room temperature and with no external loading. Additionally, the intergranular features on specimen 9 suggest that at 316 °C (600 °F) the absorbed hydrogen can readily diffuse and repartition within the C–103 microstructure, resulting in intergranular fracture.

To interrogate the potential role of SCC in the damage of the C–103 material, a specimen (specimen 10 in table IV) was loaded to 221 MPa (32 ksi) and exposed to the dilute HF solution for more than 90 hr at an applied potential of –100 mV_{SCE}. The potential of –100 mV_{SCE} was chosen to represent the most susceptible condition for SCC processes in the dilute HF solution, based on the electrochemical testing presented previously in section 2.4.3. Following the 90 plus hours of exposure, uniform corrosion of the surface was observed on the surface of the specimen (see fig. 34); however, no cracking was observed.

These results show that the RCS thruster material can suffer from hydrogen embrittlement when exposed to a hydrofluoric acid containing etchant similar to that used during the processing of the RCS thruster. It should be noted that the electrochemical characterization tests presented earlier in section 2.4

also indicate that hydrogen can be produced under certain conditions with C−103 in water, although the solution is not as electrochemical active without the HF present. However, the uniaxial tension testing in the dilute HF solution did not reproduce the considerable IGC observed in the thruster material. This suggests that while the absorption of hydrogen within the bulk of the C−103 is affecting the cracking processes in the thrusters in service and in these uniaxial test specimens, the absorbed hydrogen level and/or loading conditions used in these tests were not sufficient to replicate the exact fracture mode observed in service. A change in fracture mode for hydrogen embrittlement processes based on absorbed hydrogen level and loading condition has been previously reported for other material systems (refs. 19 and 41).

2.5.2 Bend Testing

A total of four bend specimens was examined to more accurately reflect the exposure of etchant solution and the mechanical loading (i.e., bending versus uniaxial tension) observed in the relief radius region for the thruster components. The procedures used in this testing were based on previous tests performed at Johnson Space Center (ref. 42) in collaboration with this study. Rectangular test specimens having a minimum thickness of 2.5 mm (0.1 in.) were machined. In the middle of one broad surface of the specimen, an indentation was made using a Rockwell ball indenter. As illustrated by the schematic in figure 35, each specimen was then placed in a three-point bend fixture such that a tensile stress of 276 MPa (40 ksi) was applied at the indentation; the stress was calculated without consideration of the reduced cross-sectional area at the indentation and without consideration of any change in the residual stress produced from the indent. The applied stress was selected to be consistent with the stress calculated (ref. 33) for the relief radius in previous studies and approached the reported values for the 0.2-percent yield strength (ref. 35) for C−103. The niobium etchant (HF, HNO_3, and H_2O in equal proportions) was then diluted by 50 percent, and a few drops of it were placed on the specimen to cover the indentation mark. A sheet of Ti-6Al-4V was then placed over the indentation, and the entire specimen was sealed in a cell to maintain the air at a relative humidity (RH) in excess of 70 percent, thereby limiting evaporation of the diluted etchant. Each specimen was exposed to this condition for a minimum of 36 hr. The environmental cell was then removed, and each specimen was baked in air for 48 hr at 316 °C (600 °F), while maintaining the applied bending load. After each specimen cooled to room temperature, wires were spot welded in close proximity to the indentation on each specimen, in order to monitor crack growth using a direct current potential difference (DCPD) method (ref. 43). After wire attachment, the environmental cell was reintroduced to expose each specimen again to a moist air environment (>70-percent RH), with exposure times varying from 7 to 45 days. Following this exposure process, each specimen was overloaded in bending to reveal any cracking that may have occurred during the environmental exposure.

Significant cracking (>0.36 mm (0.014 in.) in depth) was observed in each of the four bend specimens, and the resultant fracture surfaces were 100 percent intergranular in nature, as shown in figure 36. In addition to the intergranular nature of the cracking, “popcorn” features were evident on the fracture surfaces (figs. 37(a) and (b)). These popcorn features are consistent with those observed on the intergranular cracks in the RCS thrusters, and details of these observations in S/N 120 and 132 will be described in sections 3.1 and 3.2, respectively. The similarities in the microstructural observations between the test specimens and in-service hardware suggest that the simulated damage processes are consistent with those produced during the processing of the thruster components that have experienced environmental cracking.

The DCPD measurements did not resolve any crack extension during the high humidity exposures following bakeout, even for the specimen tested for 45 days. Figure 37 contains a series of micrographs at the tip of one of the intergranular cracks produced in bend specimens. The popcorn features observed on the fracture surface of the test specimens are found in abundance across most of the environmental crack (figs. 37 (a) and (b)). Only a small region (i.e., five grains in length at the crack tip) of relatively clean grains have been observed in each specimen studied (see fig. 37(c)). This observation is consistent from specimen to specimen, is independent of exposure time, and is consistent with observations for cracks produced in S/N 132. Most importantly, these observations suggest that the IGC produced in each specimen was present prior to the high humidity exposures, and significant crack growth (greater than 0.08 mm (0.003 in.)) will not occur in service following the bakeout process without the introduction of additional etchant.

2.5.3 Summary and Conclusions for Mechanical Testing

The IGC observed in the RCS thruster components is due to hydrogen embrittlement. When exposed to a dilute HF solution, a bending load, and elevated temperature (316 °C (600 °F)), IGC consistent with that observed in service has been produced.

(1) Dissolved hydrogen can result in various fracture modes for C−103, which are dependent upon the absorbed hydrogen level and loading condition.

(2) C−103 does not suffer from dissolution-based SCC under the range of conditions examined in this study.

(3) No significant crack propagation is expected to occur in service for the RCS thrusters, even under exposures to moist air environments after the elevated temperature bakeout, as long as additional HF-containing compounds are not introduced to the components.

Section 3: Fractography of RCS Thruster Hardware

The first failure analysis conducted on RCS thruster S/N 120 was performed at Boeing HB in June 2004, the results of which were described previously in section 1. The fracture surfaces that were opened and examined at Boeing HB, along with the remaining pieces after machining the injector half shown in figure 4, were supplied to GRC for subsequent examination by the NESC Materials SPRT. The purpose of this additional fractography by the NESC Materials SPRT was to verify fracture damage modes on the actual hardware and to employ additional microscopy techniques in an effort to look for evidence of crack propagation.

3.1 Observations in S/N 120

The failure analysis on S/N 120 was initially conducted on the half of the injector (fig. 4) that included bolt holes H through O. The other half of S/N 120 that included bolt holes P through G was set aside for NDE development, although it was used later in May 2005 to investigate repair and rejuvenation processes at WSTF. A schematic diagram of S/N 120 in figure 38 identifies the approximate thruster locations from which crack depth data were obtained, as well as the organizations that produced these data. Ten out of sixteen counter bores (A through P) were cracked in S/N 120, and these are indicated in the figure by the filled red circles; unfilled circles indicate that the counter bores were uncracked. For the relief radius cracking, dye penetrant inspection indications from Boeing HB (ref. 4) and WSTF are shown in the schematic by the blue and green lines, respectively. The former was obtained in 2004 on the entire thruster circumference, whereas the latter was obtained in 2005 only on the injector half that included bolt holes P through G. Dye penetrant inspections obtained at WSTF indicated more extensive cracking than those from reference 4.

The crack depth data are summarized in figure 39 as a function of angle around the circumference of the thruster; the blue diamonds in the figure representing the relief radius cracking and the pink squares representing the counter bore cracking. More data have been obtained for the depth of relief radius cracking than that for the counter bore cracking. Figure 39 indicates significant cracking around the circumference, although the depths of cracking are highly variable. No apparent relationship was evident between the depth of the cracking and the position around the circumference. Assembly stresses are believed to contribute to the relief radius cracking as a result of the bolting together of nonflat flanges. The cracking in S/N 120 is relatively shallow compared to another thruster, S/N 132; crack depth profiles will be presented for S/N 132 in section 3.2. It is unknown how these crack depths compare to those in the thruster fleet.

Relief radius cracks in S/N 120 were opened up to view the intergranular fracture surfaces in order to confirm that the cracking was produced during manufacturing in the presence of fluoride-containing acids. Scanning electron microscopy, EDS, and Electron Spectroscopy for Chemical Analysis (ESCA) were performed on the opened crack faces. The reaction product chemistries, morphologies, and densities were examined from the crack mouth to the crack tip for the following portions of S/N 120: the relief radius cracking between bolt holes I and J; the relief radius cracking between bolt holes J and K; and the relief radius cracking near bolt hole L. Similar results were obtained from each of these areas; much of the data that will be presented was obtained from the relief radius cracking between bolt holes I and J, unless otherwise noted. These bolt holes are identified in figures 4 and 38.

3.1.1 Relief Radius Cracking Observations.

The cracking on the relief radius surface was observed in the SEM prior to the lab opening of the cracks. Figure 40(a) shows the relief radius surface and its proximity to bolt hole J. It is evident from figure 40(b) that the relief radius cracking is not a single crack but a series of multiple cracks with separate initiations. Many cracks appear interconnected and branching is evident, whereas other cracks are observed to overlap without joining. The relief radius cracking between bolt holes I and J was subsequently opened and revealed an intergranular fracture surface with no change in fracture mode observed at the crack tip. An overall image of the intergranular surface is shown in figure 41(a); the deepest part of the intergranular crack in this area was measured to be 2.5 mm (0.097 in.). A deeper crack (5.0 mm (0.195 in.)) was also opened 19° away in a clockwise direction around the circumference near bolt hole J and is shown in figure 41(b); this montage of BSE images reveals that the cracking occurs over slightly different elevations as a result of the separate crack initiations at the relief radius. The intergranular surface is oxidized across its depth, as indicated by the darker appearance of the intergranular crack relative to the lighter lab fracture, which is freshly exposed C−103. Although the major crack direction is oriented vertically in the montage in figure 41(b), locally the cracking may progress in different direction as cracked ligaments link together; this observation is supported by the appearance of lighter areas (circled in fig. 41(b)) within the major intergranular cracked region.

The higher magnification in figure 41(c) reveals more clearly the intergranular nature of the fracture surface, as well as the presence of products on the grain facets. Although predominantly intergranular, the fracture surfaces contain secondary cracks that are transgranular (fig. 41(d)). These transgranular cracks were also present in polished mounts of other sections of the relief radius cracking in S/N 120, which demonstrates that the secondary cracks were not associated with lab opening procedures. Most of the transgranular cracks

observed were very shallow, as seen in the polished section in figure 41(e). Microprobe line scans were performed traversing across the intergranular crack in figure 41(e), into the adjacent regions containing the secondary cracking, and into the grain interior. No chemical differences were detected between the regions containing the transgranular cracking and the neighboring C–103 material. Thus, the transgranular cracks extended beyond the niobium oxide and reaction products on the intergranular surfaces and penetrated into the C–103 parent material. Secondary cracking may be a signature of hydrogen-assisted cracking.

It is evident from the representative views in figures 41(c) and (d) that "bumps" and cracked nodules were prevalent on the intergranular crack surfaces. The cracked nodules resembled opened popcorn kernels that appeared to be residing on top of the intergranular fracture surface. Some grain facets had higher densities of the popcorn than others, but nonetheless popcorn is observed from the crack mouth to the crack tip. Quantitative analyses of the popcorn density showed no distinct changes in the popcorn density on S/N 120 crack surfaces as a function of distance to the crack tip; these data will be discussed in detail later in section 3.3 in this report. EDS scans were obtained from various features on the intergranular surface at the mouth, tip, and the midpoint of the crack. Figure 42(a) shows a secondary electron image of the crack tip and the adjacent overload area ahead of the crack, and figure 42(b) is the corresponding BSE image. Secondary electron images provide more topographical information about a given area, whereas BSE images additionally provide indications of atomic number differences in the features within the field of view. EDS scans were obtained from locations labeled "C," "D," and "E" in figures 42(a) and (b); most of the EDS scans were taken at an accelerating voltage of 6 keV, which enables more of a surface analysis to be performed because the characteristic x-rays generated are confined to near-surface depths. A representative EDS scan of the popcorn nodule, labeled "C," is given in figure 42(c); the popcorn was found to contain high oxygen and fluorine peaks, in this case with roughly a 2:1 peak ratio, respectively. A peak for carbon was also exhibited adjacent to the niobium M line; and niobium (L line) and hafnium peaks are also evident in the EDS scan. Numerous popcorn nodules were analyzed across the fracture surface, and very similar results were obtained. The popcorn was identified as most likely being NbO_2F, based on semiquantitative analyses, which is an expected reaction product that forms after NbF_5 is exposed to moisture in the air (ref. 32) at elevated temperatures. It is not clear if the carbon evident in the EDS scans is tied up chemically in the popcorn or if carbon was introduced as a contaminant after popcorn formation.

Single crystals of niobium have been shown in the literature to form oxide nodules (ref. 44) that have a very similar appearance to the popcorn observed on the S/N 120 crack surfaces. Pure niobium initially forms a protective oxide film that has a rippled or bumpy texture; the film becomes nonprotective as oxidation proceeds due to a breakaway oxidation phenomenon, which is characterized by the formation and growth of isolated patches of locally thick oxide. Small cracks form in the locally thick oxide scales, which enable more oxygen to diffuse into the niobium substrate beneath the scale. This significantly increases the rate of oxidation beneath these cracked areas and promotes the formation of nodules or popcorn at these locations. Reference 44 also demonstrates that crystallographic orientation influences the rate of oxidation in single crystal niobium, which is consistent with the observation in S/N 120 that some grain facets have more popcorn formation than others. It will be shown later in section 3.3 that popcorn does form during the oxidation of C–103 at thruster manufacturing bakeout conditions (48 hr in air at 316 °C (600 °F)) but only if fluorine is present.

The oxide scale on the intergranular surfaces near the popcorn was also analyzed for comparison to the popcorn. The EDS scan in figure 42(d) for location D (in fig. 42(a)) shows high oxygen and similar niobium and hafnium peaks compared to the popcorn. Although fluorine was detected in the oxide scale, its peak height was typically much lower than those for oxygen and niobium (L line) in the oxide scale. The fluorine content in the oxide scale is also lower than that in the popcorn. It should be noted that the carbon peak was not evident at location D, and this was a typical result for the light regions on the oxidized intergranular surface in figure 42(b). However, the EDS scans were significantly different when obtained from the darker regions (location E) on the fracture surface of figure 42(b); darker regions in BSE images indicate the presence of lower atomic elements. In these areas, the carbon peak was one of the strongest peaks observed; sodium and magnesium peaks were also exhibited (fig. 42(e)). The presence of sodium is often considered to be a contaminant that may be the result of handling issues.

Other dark regions were also observed with BSE imaging, especially along changes in elevation seen on the fracture surfaces, such as in valleys created between grain facets as seen in figure 43(a). Dominant carbon and fluorine peaks were observed in the EDS spectra for these dark areas (figs. 43(b) and (c)). The carbon- and fluorine-rich material did not appear to be tied up in the oxide because the material was observed to vaporize under the electron beam in the SEM. Subsequent analyses conducted on the cutting fluid used in sectioning this sample prior to the lab opening show a distinctly different chemistry from that shown in figures 43(b) and (c). It is possible that the dark carbon- and fluorine-rich material on the fracture surface is residual Krytox (DuPont, Wilmington, DE) or residual dye penetrant material. Krytox is believed to have been used as a lubricant for the counter bore bolts, and detailed ESCA analyses (section 3.4) confirmed that a compound with a signature similar to Krytox was present on the intergranular surfaces of S/N 120. Krytox is reported to react with

niobium oxides (ref. 45); subsequent reactions can cause the release of trace amounts of HF (ref. 46), which could result in IGC in a manner similar to that which is believed to have occurred with the preweld etchant during the 316 °C (600 °F) thruster bakeouts.

Other morphological features were also present in isolated areas on the intergranular crack surfaces. Examination near the crack mouth (fig. 44(a)) revealed the presence of cubic-shaped products and some regions that looked like "mud-flats." EDS scans in figures 44(b) and (c) show that both of these areas were also rich in oxygen, fluorine, carbon, and niobium. Strong sodium peaks were also evident in the mud-flat areas. The cubic-shaped and mud-flat products were confined to localized areas in the crack mouth. Acicular morphologies, rounded particles, and clusters were also observed across the intergranular fractures; examples of these features are shown in figure 45. The acicular products may be oxides, since EDS indicated large oxygen peaks, although other reaction products, or contaminants and debris that may have been swept into existing cracks could not be ruled out. The small surface bumps, uncracked rounded particles, and clusters are likely different variants of popcorn nodules in various stages of development. The EDS scans confirm the microprobe data, which indicate that oxygen, fluorine, and carbon are clearly present on the intergranular cracks of S/N 120. This is also consistent with scanning Auger results (refs. 4 and 8) from the crack surfaces and machined injector surfaces in which higher concentrations of fluorine, carbon, and oxygen were found for a 1 to 2 μm depth before returning to nominal levels.

The opening of the intergranular crack also enabled a depth profile to be obtained through the oxide scale in a uniquely positioned grain on the fracture surface. The intergranular surfaces were cracked nearly all the way around this particular grain, except for one remaining ligament that kept the grain attached to the opened fracture surface (fig. 46(a)). During the lab opening, one of the grain facets fractured, which revealed fresh C−103 in an orientation that was normal to the electron beam in figure 46(b); the freshly exposed C−103 is lighter in color than the oxidized scale on the intergranular surface. The positioning of the grain provided a longitudinal cross section of the surface products and enabled a depth profile to be obtained through the oxide scale from the top intergranular surface down to the C−103 substrate. Figure 46(c) shows a higher magnification view of the oxide scale and C−103 substrate; D, E, and F represent the locations for the EDS scans shown in figures 46(d), (e), and (f), respectively. Comparison of the EDS data shows that the top layer in figure 46(d) contained the highest fluorine level. Lower fluorine levels are evident at location E, which is approximately midway between the oxide surface and the C−103 substrate, and the EDS scans (fig. 46(e)) from location E were dominated by the oxygen and niobium peaks. The material just under the oxide scale in location F appeared to be consistent with baseline C−103 that had been slightly oxidized (fig. 46(f)); a small oxygen peak is evident but the fluorine peak is not above background levels. Thus, it appears that the fluorine content decreases through the depth of the surface product as the niobium base alloy was approached.

These depth profile results by EDS were repeated in three other locations, and the observed trends were very consistently repeated. In addition, an x-ray line scan was obtained from the surface of the oxide scale through to the freshly exposed C−103 in increments of 0.02 μm. Figure 47(a) shows that the oxygen levels are highest in the middle region, after which the oxygen drops off dramatically at the C−103 substrate. The fluorine levels are again highest near the surface and decrease through the thickness of the scale. Figure 47(b) shows that the carbon was more heavily concentrated near the surface of the oxide scale, which is consistent with scanning Auger results (refs. 4 and 8). Thus, a composition gradient is clearly present through these oxide scales with the fluorine content decreasing through the depth of the oxide as the C−103 is approached. If the IGC was caused by a dissolution process, instead of by hydrogen embrittlement, then the fluorine levels would be expected to be highest in the regions adjacent to the niobium parent material. Therefore, these data also do not support a dissolution process by stress corrosion or hot-salt cracking.

3.1.2 Conclusions and Summary of Observations for S/N 120

Cracking was intergranular from the mouth to the tip with no change in crack mode observed. No evidence was found for crack propagation after manufacturing.

(1) The intergranular crack faces contained significant oxidation with popcorn oxidation evident from the mouth to the tip. Although some grain facets exhibited more popcorn formation than others, quantitative analyses of the popcorn density showed no distinct changes in popcorn density as a function of distance to the crack tip.

(2) Fluorine, carbon, and oxygen were readily detected on the crack surfaces. Depth profiling through the reaction product scale indicated that the highest concentrations of fluorine were found at the surface and that the fluorine content diminished as a function of distance as the niobium parent material was approached.

(3) Relief radius cracking was observed to be not a single crack but a series of interconnected cracks with separate initiations. The depth of cracking was highly variable.

3.2 Observations in S/N 132

3.2.1. Background

Ultrasonic (UT) NDE inspection of RCS thruster S/N 132 on April 12, 1979, revealed relief radius cracks (ref. 47). A

partial history of S/N 132 is also documented in reference 48. After the cracks were discovered, S/N 132 was selected for use as a qualification test article. Ultrasonic inspections were performed after each round of testing with no crack growth detected, although it was not known at the time that this NDE method was unreliable. The thruster was reassembled in March 1982 with new insulation and was given a second 48-hr insulation bakeout in air at 316 °C (600 °F) (ref. 47). The thruster experienced an unstable operation during a test firing on March 23, 1983 (ref. 47), which resulted in injector temperatures exceeding 260 °C (500 °F) for a 24 sec duration with a 304 °C (580 °F) peak temperature reached (refs. 47 and 48). On August 4, 1983 (ref. 47), S/N 132 failed an external leak check, which indicated that the cracks had propagated through the injector wall to the acoustic cavity(ies). The unit was used in 2004 and 2005 for the development of NDE methods for the reliable detection and quantification of relief radius cracks. In addition, two small pieces of this injector were examined by Boeing HB in 2004 to determine if, and by what mechanism, the cracks propagated during thruster qualification testing; these results were reported in reference 48. The report concludes from the two pieces (labeled acoustic cavity (AC) numbers 14 and 16) examined that the intergranular crack propagated from the relief radius to the acoustic cavities by the same failure mechanism with no change in failure mode. The cracks were believed to have propagated during the original failure event with no evidence found for intermittent, time-delayed failure or for fatigue. The report also concludes that hydrogen embrittlement did not occur because of the presence of oxygen- and fluorine-bearing deposits on the intergranular fracture surface.

The NESC strongly recommended to the Orbiter Project Office that a destructive examination of another thruster be performed by the NESC Materials SPRT. The purpose of the examination was twofold: (1) to determine if there was any evidence for fatigue crack growth during thruster operation and (2) to define the crack front for input to the NESC Stress and Fracture SPRT in their fatigue and fracture modeling. The crack depth profile of the relief radius cracks and the symmetry of cracking would be defined quantitatively, in order to benchmark the starting crack profile for vibration load analyses. RCS thruster S/N 132 was supplied to GRC in March 2005 as a result of this recommendation. The two large sections (a 57° and a 203° piece) of S/N 132 that were destructively analyzed are shown in figure 48. The extent of this examination enabled the most comprehensive data to be obtained to date on crack depth profiles for RCS thruster hardware.

3.2.2 Crack Surface Observations

Replicas were obtained for future examination from the entire relief radius and all counter bores (half of N to P and C to K) from the two large sections prior to further sectioning. Figure 49 is a schematic diagram of S/N 132, which identifies these two sections and references these sections to the bolt hole letters and numbered acoustic cavities. Stereo optical microscopy was also performed on the two thruster sections prior to further sectioning. It was found that relief radius cracking extended around about half of the smaller section, from about AC number 10 through to the edge of AC number 14. The larger section was cracked nearly all the way around its circumference, extending from the edge of AC number 19 to 42. It should be noted that, based on the NESC analysis of the S/N 132 thruster pieces, AC numbers 14 and 16 were incorrectly identified in the failure analysis in reference 48. It is more likely that the piece labeled AC number 14 actually contained half of bolt hole A and incomplete portions of AC numbers 15 and 16; and the piece labeled AC number 16 actually contained bolt hole B and part of AC number 18. The corrected locations of these thruster pieces are shown by the cross-hatched regions in figure 49.

The NDE results that were obtained during various points in the history of S/N 132 are also indicated in figure 49. The UT inspections that were performed in the 1979–1980 time frame by Marquardt and in 2004 by Boeing HB are given by the red and green lines, respectively, in figure 49. The 2004 dye penetrant inspection results are indicated by the blue lines in the figure. There is good general agreement between the 2004 UT inspections and the 2004 dye penetrant inspections in terms of relief radius cracking locations; and these indications agreed well with the observations made by stereo optical microscopy during the destructive examination of the actual hardware. The 1979–1980 UT inspections, however, did not adequately represent the extent or location of cracking in S/N 132, which provides further evidence that the UT methods employed were neither reproducible nor reliable.

A series of 10° sections (AA through RR) were cut subsequently by wire electrodischarge machining (EDM). The sections were cut from the injector flange, inward through the acoustic cavity wall, and across the injector face to the far edge of the acoustic cavity. A perspective of this sectioning is illustrated in figure 50. The remainder of S/N 132 is shown in figure 51 after all EDM was completed; some of the relief radius was intentionally left intact with the injector face to facilitate development of NDE methods. Scanning electron microscopy was used to examine the surface of the relief radius cracks in the 10° cut sections. Figure 52 shows a montage of images taken from section GG from S/N 132. The cracking is clearly evident with multiple initiations frequently observed along the relief radius surface. Sets of arrows in the figure show examples where the cracks run parallel to each other for some distance; apparently the cracks do not shield each other under the stress states imposed. If polished cross sections were obtained at the locations indicated by the

arrows, then multiple cracks would be viewed in those polished cross sections. Section GG exhibited the typical degree of tightness of the crack at the surface. Figure 53 shows a range of tightness at the crack mouth in two different sections of the relief radius. In section QQ (fig. 53(a)), the crack is so tight that it is difficult to discern even by SEM. In contrast, section JJ contained a relatively wide open crack with little apparent branching; cracking was confined to a ledge in the relief radius for this section, and higher magnifications clearly reveal the intergranular nature of the cracking. The ledge of the relief radius is well above the root of the relief radius, part way up the injector flange (figs. 54(a) and (b)).

3.2.3 Polished Section Observations

Each EDM section had at least one side that was mounted and polished metallographically to obtain crack depth data prior to physically opening the crack. Figure 54(b) shows an example of one of these polished sections that contains a relief radius crack. The crack follows the grain boundaries, and thus some of the grains were cracked all the way around their periphery, which resulted in grains falling out during metallographic polishing. Hence, figure 54(b) shows typical polishing artifacts of pulled-out grains; the voids from these pulled-out grains do not represent actual crack widths. The micrograph also depicts the crack initiating at the relief radius surface at the previously mentioned ledge, which can be envisioned as a location where contaminants may become easily entrapped. Figure 55 shows section KK in an area where multiple cracks initiated at the relief radius; in this case, cracks with multiple branches initiated just above the relief radius ledge and another initiated at the base of the relief radius root. Again, grain pullout artifacts are observed. Between the tips of the parallel cracks in figure 55, a branch of one of the cracks, or a portion of another crack, is observed to extend well beyond the other two cracks. It is evident in figure 56 that the crack was intergranular along the entire depth and no change in fracture mode was observed in the polished sections.

Several measurements were obtained from the relief radius cracks in the polished sections; these are depicted on the metallographic mount in figure 57. Actual crack depths were measured from the point of initiation along a straight line to the crack tip. The angle of inclination was determined from the counterclockwise angle between the outer surface of the AC wall and the straight line representing the actual crack depth. Finally, the projected crack depth was measured from the point of crack initiation to a line that begins at the crack tip and runs parallel to the outer surface of the AC wall. Table V summarizes the measurements that were taken from the polished surfaces of S/N 132. The table identifies each section by letter and its location on the circumference of the relief radius, based on the number of degrees (clockwise) from AC number 1. Three sections were polished on both sides. There is an absence of data between 0° and 50° and between 107° and 155° because those parts of the injector were not available for analysis.

Table V indicates that most of the polished sections contained relief radius cracks. The percentage of the total distance of the crack to the acoustic cavity was also calculated for the projected crack depths in sections that contained acoustic cavities; some sections contained no acoustic cavities in the polished section. Table V shows that most of the projected crack depths measured were greater than 50 percent of the distance to the acoustic cavity; thus the crack depths were significant in S/N 132. Remaining ligament distances to the acoustic cavities are also provided in the table; it may be seen from these data that no cracks in the polished sections were observed to extend all the way to the acoustic cavities, although the cracks in sections OO and PP came within 0.05 mm (0.002 in.) of the distance to the acoustic cavities. Table V also indicates that the angles of the cracks were very consistent, typically between 130° and 140°. The actual crack depths and projected crack depths are displayed graphically in figure 58, where the crack measurement is shown versus the location within the thruster, based on the number of degrees clockwise from AC number 1. The dashed line in the figure represents the projected distance from the relief radius to the acoustic cavity. Figure 58 shows that cracks occur over 75 percent of the injector circumference, with the deepest cracking present in sections FF, GG, and NN. In these three sections, the crack front actually tunneled between two neighboring acoustic cavities, resulting in projected crack depths that were greater than the distance to the acoustic cavities. No pattern between the depth of cracking and location could be ascertained.

3.2.4 Measurements After Crack Opening

The polished sections were removed from the metallographic mounts, and the intergranular cracks were physically opened in the laboratory. Two-thirds of the sections were opened by placing them in a vise and hitting them with a hammer on the underside of the injector flange. Repeated hammer hits were made until the crack was opened more than 180°; at that point, vise grips were used in a limited reverse bending action to fracture the remaining ligament of material ahead of the crack. Some of the cracks were carefully back cut with a dry saw to facilitate the subsequent hammer openings. One-third of the sections were placed in a vise with a large diameter dowel in front of the relief radius; the dowel and two edges of the sample enabled the crack to be opened more gently in the vise, using a three-point bend-type arrangement. It should be noted that all S/N 132 samples exhibited fully ductile overloads ahead of the intergranular crack tip, regardless of the crack opening procedure.

The opened fracture surfaces of the intergranular cracks were examined extensively by SEM. The observations confirmed that the fracture surface was intergranular with no change in crack mode observed from the mouth to the tip of the crack (fig. 59). When multiple cracks were observed initiating on the relief radius, these cracks did not always connect subsurface to form a single crack front, as evident in figure 60. It should also be noted that, although the majority of the cracking had initiated in the relief radius, cracks were occasionally observed elsewhere in S/N 132. For example, shallow IGC was observed on the injector flange well outside of the relief radius. This was observed in polished mounts of section AA (figs. 61(a) and (b)) and after the lab opening attempt of section RR (figs. 61(c) and (d)). In both cases, the intergranular cracks extended only a few grains in from the flange surface. Cracks in this location would be consistent with the preweld etchant becoming entrapped after entering through the bolt holes, so it is not surprising to find affected thruster material in these areas.

After crack openings were performed, it was found that relief radius cracks penetrated four acoustic cavities: AC numbers 19 and 20 (both in section GG), AC number 35 (section NN), and AC number 39 (section OO). An example of this is seen in figure 62(a), where the crack front is seen to extend into AC number 39; the crack tip fell just short of AC number 40. The micrograph in figure 62(b) also illustrates how the crack tunneled between two neighboring acoustic cavities; a more pronounced example of this is depicted in figure 63, where the crack front is clearly at a maximum depth between the acoustic cavities. This crack in section FF never penetrated either acoustic cavity. The examination of cracks of various depths suggests that the crack in this region was initially uniform in depth. As the crack front approached the acoustic cavities, the crack tip driving force in the region of the acoustic cavities became reduced relative to the crack tip region between the acoustic cavities, which resulted in the development of a tunneled crack front. The most likely cause for the tunneled crack front is the introduction of compressive residual stresses about the acoustic cavities due to the machining operation. It should be noted that no residual stress measurements were made and that the proposal of residual stresses in the region of the acoustic cavities is based solely on the observation of the shape of the crack front from the examination of S/N 132.

Several measurements were made on the fracture surfaces. The fractures were oriented in two ways: with the viewing axis perpendicular to the crack face, which enabled actual crack depths to be measured; and with the viewing axis parallel to the acoustic cavity wall, which enabled projected crack depths and minimum ligament distances to be measured. In addition, ligament distances were obtained at the shortest distance from the crack front to the nearest acoustic cavity, as well as from the maximum crack depth to the nearest acoustic cavity; figure 64 illustrates that these minimum ligament distances were usually not the same. Table VI summarizes the measurements that were taken from the opened crack surfaces of S/N 132. The table identifies each section by letter and its location on the circumference of the relief radius, based on the number of degrees clockwise from AC number 1. Again, there is an absence of data between 0 and 50° and between 107° and 155°, because those parts of the injector were not available for analysis.

Table VI shows that only two sections, AA and BB, did not contain cracks; section QQ contained a very shallow crack that could not be fully opened even with careful back cutting. The remaining sections exhibited deep IGC. The column containing the minimum ligament distance to the acoustic cavities shows that three sections had cracks that penetrated all the way to the acoustic cavities, as indicated by the zero in the column. The crack profiles for the opened crack faces are depicted in figure 65; the crack measurements for maximum actual crack depth and maximum projected crack depth are shown versus the location within the thruster, based on the number of degrees from AC number 1. The dashed line in the figure represents the projected distance from the relief radius to the acoustic cavity. Figure 65 shows that cracking occurs in over 75 percent of the injector circumference, with the deepest cracking present in sections FF, GG, JJ, and NN. The crack fronts in these sections tunneled between two neighboring acoustic cavities and thus had projected crack depths greater than the distance to the acoustic cavities. Again no pattern between the depth of cracking and location could be ascertained. The cracking in S/N 132 was considerably deeper and more extensive than that observed in S/N 120, based on comparisons of figures 39 and 65. It is not known how the crack profiles of these two thrusters compare with the remainder of the thruster fleet.

3.2.5 Observations for Crack Growth in Thrusters

The fracture surfaces in S/N 132 were also examined carefully for any evidence of crack growth. Popcorn oxidation was observed along the crack front from the crack mouth to the crack tip, as seen in figures 66(a) to (c). No significant changes in the popcorn appearance were observed across the crack surface. However, regions of clean-looking grains with no popcorn were observed at the crack tip next to grains that were covered with popcorn, and an example of this is shown in figure 66(d). This clean appearance of some of the grains at the crack tip has been reported previously for S/N 132 in reference 48. Intergranular crack surfaces with no popcorn or other reaction products have also been produced by monotonic laboratory testing; this was shown previously in the C-ring specimen in figure 25(b) and in the uniaxial tensile specimen in figure 33. In contrast to S/N 132, the clean grains in the laboratory-tested specimens were observed across wide

regions of the fracture and were not confined to the crack tips. EDS spectra from the grains without popcorn have reproducibly shown that they are minimally oxidized (fig. 25(c)).

Several explanations have been proposed for the observation of clean grains at the crack tip in S/N 132. One explanation is that the crack tip is so tight that it limits oxidation at the crack tip. Although this may be feasible, the lack of bare grains at the crack tip in S/N 120 is hard to rationalize, because it would also be expected to have tight crack tips. The fact that minimally oxidized grains were observed in laboratory tests designed to reproduce the intergranular thruster failures keeps this tight crack tip theory as a strong contender. However, another possibility is that the intergranular cracks in S/N 132 grew in these very localized regions after thruster bakeout. It will be shown in section 3.3 that popcorn features develop only in the presence of fluorine and at temperatures greater than 204 to 232 °C (400 to 450 °F). If the cracks propagated during qualification testing in S/N 132, the lack of popcorn at the crack tip could be explained because the thruster temperatures during normal operations are significantly lower in magnitude and duration compared to those during bakeout, and thus popcorn would not be expected to form in those regions. Lattice dilation caused by the stress field at crack tips can enhance hydrogen permeation into these regions (ref. 49); the trapped hydrogen would be available to cause cracking under service loading at lower service temperatures, where materials are often more susceptible to hydrogen embrittlement. This cracking would be expected to have a limited extent since the original source of the hydrogen would no longer be present. However, the lack of bare grains at the crack tip in S/N 120 is again hard to rationalize because S/N 120 was the fleet leader with 29 flights and over 12 000 firings (ref. 50), although S/N 132, as a qualification test article, underwent 100 simulated missions and 26 000 firings (refs. 33 and 51). The final possibility is that the bare tip regions signify minimal crack growth during the unstable firing that occurred in S/N 132 during qualification testing. The short duration instability to a peak temperature of 304 °C (580 °F) would not have provided adequate time for significant oxidation and popcorn formation to occur. The service history and timing of the leak checks in S/N 132 are not inconsistent with this possible explanation.

The three possible explanations given above for the observation of minimally oxidized grains at the crack tip in S/N 132 cannot be ruled out. If the clean grains are interpreted as evidence for crack growth following manufacturing, the amount of crack growth would be extremely limited. Therefore, it has been concluded that no evidence was found in S/N 132 for *appreciable* crack propagation after manufacturing, with appreciable being defined as greater than 0.08 mm (0.003 in.). The lack of widely distributed clean grains at the crack tip is demonstrated in figure 67. This figure is a montage of BSE micrographs showing a typical distribution of minimally oxidized grains at a crack tip in S/N 132. It is clear that the clean-looking grains are not extensively distributed and are present only in isolated pockets along the crack front; these regions of minimal oxidation have been circled in the montage.

A few other features were noted on the fracture surfaces of S/N 132. Figure 68 shows what appears to be slip planes on some of the minimally oxidized grain facets at the crack tip. This may provide evidence for a hydrogen embrittlement mechanism, which involves sweeping hydrogen into the plastic zone through dislocation transport from the crack tip. Hydrogen becomes trapped on the dislocations at the crack tip and preferential slip occurs locally. The uptake of hydrogen at the crack tip by this mechanism has produced intergranular fracture modes in the literature (refs. 52 and 53). Other regions of the oxidized fracture surface show what appear to be striated patterns of deposits on the grain facets (fig. 69). This has been observed previously in S/N 132 (ref. 48) and in counter bore cracks of S/N 120 (ref. 54). The reason for this striated pattern is unknown at this time; it is possible that this feature may be the result of popcorn formation along the slip planes observed in figure 68.

3.2.6 Conclusions and Summary of Observations for S/N 132

No evidence was found for appreciable crack propagation after manufacturing. Appreciable is defined to be greater than 0.08 mm (0.003 in.) and corresponds to the longest lengths at the crack tips where “clean” grains were observed.

(1) Cracking was intergranular from the mouth to the tip with no change in crack mode observed.

(2) The intergranular crack faces contained significant oxidation with popcorn evident from the mouth to the tip, except for small pockets of clean, popcorn-free grains at the crack tip. These clean-looking grains were not observed in S/N 120.

(3) Extensive cracking was observed in over 75 percent of the injector circumference. Cracking was significantly deeper and more extensive in S/N 132 compared to that in S/N 120.

(4) Four acoustic cavities in S/N 132 were breached by IGC.

3.3 Oxidation Tests to Reproduce Popcorn Oxidation

3.3.1 Testing and Observations

Additional tests were conducted to determine if the popcorn oxidation observed on the intergranular fracture surfaces of the thruster hardware could be reproduced. This testing would assist in determining if the intergranular cracks seen in thruster hardware were the result of manufacturing steps alone or if the thruster cracks were likely to have grown in service. An

existing intergranular surface from previous laboratory testing on C−103 was selected as a specimen for subsequent oxidation testing, because it was a fracture surface that did not contain the numerous reaction products described in sections 3.1 and 3.2. This specimen, shown previously in figure 25, was from C-ring testing and was only minimally oxidized based on detailed electron microprobe and EDS analyses. This opened intergranular fracture surface was then exposed isothermally in air at 316 °C (600 °F) for durations of up to 100 hr. The 100-hr duration was selected as an upper limit, because thrusters undergo insulation bakeouts at 316 °C (600 °F) for 48 hr in air, and both S/Ns 120 and 132 have each undergone two 48-hr bakeouts in their processing history.

SEM and EDS were performed after each oxidation exposure of 5, 10, 20, 30, 50, and 100 hr at 316 °C (600 °F) to monitor the intergranular surface for possible changes in surface features and chemistry. After each oxidation interval, numerous grain facets on the fracture surface were examined for possible popcorn formation, since grain orientation has been shown to influence subsequent oxidation (ref. 44). Figure 70 shows the same set of grains at a triple point as a function of exposure time at 600 °F. It is evident in the figure that no popcorn or cuboidal oxide formation was observed even after 100 hr at 316 °C (600 °F), which is roughly equivalent to the exposure conditions from two thruster bakeout cycles. Figure 71(a) shows the EDS scan for the starting fracture surface, which is representative of minimally oxidized C−103 material. EDS scans obtained after 10, 50, and 100 hr at 316 °C (600 °F) are displayed in figures 71(b) to (d), respectively, and show that the biggest change in the fracture surface chemistry is observed after 10 hr, where the oxygen peak increased significantly in magnitude. Thus, the sample was oxidizing during the 316 °C (600 °F) exposures, but no other significant changes were evident. The results show that exposure times and temperatures consistent with a double bakeout cycle enable an oxide scale to form on C−103 but are insufficient for popcorn formation. It should be pointed out that the thruster is exposed to the out-gassing of water and carbon dioxide (ref. 55) from the thruster insulation material during the manufacturing bakeout, and this was not being simulated in these laboratory oxidation tests.

Air exposures were also conducted at 399 °C (750 °F) for 5 hr on the intergranular fracture surface after the 100-hr exposure at 316 °C (600 °F) and on virgin C−103 specimens with polished surfaces. This exposure temperature was selected to simulate the effects of an inadvertent temperature excursion during the manufacturing bakeout cycle and for comparison to oxidation experiments (ref. 44) on pure niobium. No popcorn oxidation formed on either the intergranular surfaces or the polished surfaces of C−103 after 5 hr at 399 °C (750 °F), which is inconsistent with the blistering observed after similar exposures in the literature were conducted on pure niobium (ref. 44). The reason for this difference in behavior is not known, although the alloying elements may have affected the oxidation rates and the breakaway oxidation phenomenon. Since the popcorn features on the thruster hardware surfaces were analyzed and were found to contain fluorine, it is believed that the absence of residual etchant on the C−103 test specimens contributes to the lack of popcorn formation. This is supported by the next set of tests performed on C−103 machined specimens and is described below.

Two polished samples of C−103 were exposed to the preweld etchant consisting of HF, HNO_3, and H_2O in equal proportions. While wet, the two samples were laid one on top of the other, forming a "sandwich" specimen with the etchant entrapped. The sandwich was held together with stainless steel wire and dried overnight before an air exposure at 316 °C (600 °F) for 24 hr. The specimen was separated subsequently for examination. Numerous reaction products with different textures and colors were observed with some locations displaying popcorn-like oxidation, as seen in figure 72. The popcorn oxidation was observed in the regions that contained dried HF deposits. Similar tests were conducted with C−103 sandwich specimens at 204, 399, and 816 °C (400, 750, and 1500 °F) for 24 hr in air. The specimens exposed to 204 °C (400 °F) produced oxidized surfaces with small bumps present on the oxide scale; the bumps were similar in size to the popcorn oxidation observed on the thruster hardware, although the bumps did not have the cracked appearance that the popcorn typically exhibited. The bumps appeared to be precursors to the popcorn oxidation, and varied in density across the specimen surfaces. In contrast, the 399 and 816 °C (750 and 1500 °F) exposures produced cracked oxide scales, but neither exposure produced popcorn oxidation. These tests suggest that a narrow range of temperature and the presence of fluorine are required to form popcorn oxidation on C−103. Specifically, for the cracked popcorn to form, it appears that a temperature greater than 204 °C (400 °F) and less than 399 °C (750 °F) are required. These data support the conclusion that the formation of popcorn oxidation on the intergranular cracks in the thruster hardware most likely occurred during the 316 °C (600 °F) manufacturing bakeout cycle.

3.3.2 Conclusions and Summary of Oxidation Testing

The intergranular cracks seen in the thruster hardware were the result of manufacturing steps alone, since popcorn features observed on the hardware IGC could only be reproduced with 316 °C (600 °F) manufacturing bakeout cycles in the presence of HF-containing etchants.

(1) A narrow range of temperature and the presence of fluorine are required to form popcorn oxidation with a cracked appearance on C−103.

(2) Normal thruster operation is not expected to form cracked popcorn oxidation because C−103 specimens exposed

to 204 °C (400 °F)/24 hr only produced oxidized surfaces with small bumps that appeared to be precursors to the popcorn oxidation.

(3) Manufacturing bakeout cycles conducted without HF-containing etchants did not produce popcorn oxidation after 100 hr of exposure.

3.4 Fracture Surface Analysis by Energy Spectroscopy for Chemical Analysis (ESCA)

3.4.1 Oxide Analysis

ESCA is a surface analysis technique that was used to identify elements and their oxidation state that were present on the fracture surface of intergranular cracks in S/Ns 120 and 132. Organic and inorganic compounds can be identified with ESCA by comparison of binding energy spectra from known compounds. Generally, the best quantitative results can be obtained with polished specimens, but the presence of elements and qualitative trends can be established on fracture surfaces. In addition, depth profiling through the surface layers can be performed with ion-milling; and again, although this can be done on a fracture surface, this technique is best accomplished on a flat specimen where a uniform amount of material removal can be accomplished.

ESCA was performed first on the surface of the relief radius crack near hole L of S/N 120. The original intent was to identify reaction products and determine their distributions across the intergranular fracture surface by taking ESCA scans at multiple locations. Figure 73 shows the fracture surface of this relief radius crack and locations A through F where ESCA analysis was performed. The dotted line superimposed on the image of the fracture surface indicates the approximate locations for the crack tip. Location C represents the lab overload area, whereas the other locations are from the intergranular crack surface. The extremities of the crack surface, as well as areas having different surface colorations, were intentionally selected for analysis, in an effort to determine if the spectra differed as a function of location, thereby indicating possible progression of the crack over time.

Figure 74(a) shows the ESCA spectra obtained from the lab overload area at location C; it is evident that four peaks are resolved for the spectra. Typical ESCA spectra from metallic niobium surfaces would be expected to show a binding energy doublet, or two peaks of equal magnitude, for Nb 3d5/2 and 3d3/2 at 202.0 and 204.7 eV, respectively (ref. 56). As the niobium surface becomes oxidized, the peaks in the spectra shift to higher binding energy values, with the higher oxides (e.g., Nb_2O_5) shifting more than the lower oxides (e.g., NbO). Comparison of the binding energy line positions for the peaks in figure 74(a) to reference spectra in the literature (refs. 56 and 57) for niobium, NbO, NbO_2, and Nb_2O_5 indicates a close match to niobium metal and Nb_2O_5. The two rightmost peaks in figure 74(a) represent the niobium doublet and the two leftmost peaks represent Nb_2O_5. Thus, based on these data, the lab overload area has a slightly oxidized niobium surface.

In contrast, the typical spectra obtained from the intergranular crack surfaces at five locations (A and B and D to F) are shown in figure 74(b), where only three peaks are resolved for those spectra. Comparison of the line positions for the peaks in figure 74(b) to the reference spectra in the literature (refs. 56 and 57) reveals a close match to NbO and Nb_2O_5; no metallic niobium doublet is evident. The rightmost peak in the figure represents NbO, the leftmost peak represents Nb_2O_5, and the middle peak has the highest magnitude from the overlap of additional peaks from NbO and Nb_2O_5. The spectra in figure 74(b) are typical for more heavily oxidized surfaces that contain a mixture of oxides (ref. 56). Thus, the intergranular crack surface has a thicker and more complex oxide scale than that of the lab overload region. Table VII lists the line positions for the low oxide (NbO) Nb3d5/2 and for the high oxide (Nb_2O_5) Nb3d3/2 obtained from locations A and B and D to F in S/N 120. It is evident that the line positions were similar across the entire intergranular crack surface from mouth to tip. Additionally, the areas under the peaks for the low and high oxides were integrated, and the resulting percentages of total volume for each oxide on the analyzed surface are also given in table VII. These data indicate that the low oxide, NbO, is consistently the majority phase in the oxide scale of the intergranular crack surface. Thus, the same oxides were found in approximately the same volume fraction across the fracture surface, which provides further evidence that the intergranular thruster cracks did not form progressively over time.

3.4.2 Analysis of Other Compounds

The ESCA spectra from the intergranular crack surfaces revealed the presence of additional peaks that were associated neither with the niobium substrate nor with the above mentioned oxides. Figure 75(a) shows spectra containing two peaks for fluorine and for oxygen and multiple small peaks for niobium, and figure 75(b) shows spectra at lower binding energies where three peaks for carbon and for niobium are seen. The rightmost peaks of fluorine and oxygen in figure 75(a) are believed to be associated with NbO_2F, a reaction product described earlier as resulting from a chemical reaction between NbF_5, oxygen, and residual moisture in the air (ref. 32). The rightmost carbon peak that is barely above background levels in figure 75(b) is likely the result of contamination from handling. The niobium peaks in figure 75(b) were resolved in figure 74(b) and were described in the previous section.

The remaining peaks for fluorine, oxygen, and carbon in figure 75 were relatively large in magnitude and were found consistently over the analyzed fracture surface of S/N 120; these peaks were not associated with a known reaction product and thus were explored in more detail. A subsequent review of

the injector processing steps revealed that a perfluoropolyether (PFPE) lubricant, Krytox 143AC, may have been applied to the bolts and/or bolt holes on the flange of the niobium injector during thruster assembly (ref. 55). Krytox 143AC was also used to lubricate the O-ring on the flow test fixture during four separate flow tests that were performed after various machining steps during manufacturing (ref. 55). Krytox material contains fluorine, oxygen, and carbon, and as a result of the unknown fluorine, oxygen, and carbon peaks obtained from the thruster fracture surface, an ESCA analysis was performed directly on samples of this PFPE lubricant. A comparison between the line positions obtained from Krytox 143AC and the additional (leftmost) fluorine, oxygen, and carbon lines on the thruster hardware surfaces indicated an excellent match. Furthermore, it should be noted that the PFPE lubricant migrated at least 1 mm away from its original liquid meniscus during ESCA analysis, and thus it was determined that the material has a low surface tension. Therefore, it is not hard to imagine that the Krytox material may have also migrated into the relief radius, and possibly into a preexisting crack, after being applied to the bolt hole regions of the injector.

Ion-milling was also performed at locations A and B and D to F (fig. 73) to remove surface layers in order to determine depth profiling trends. The maximum sputtering duration was 300 s, which removed about 100 nm of material, and binding energy spectra were obtained during the sputtering operation. It was found that as material was being removed from the fracture surface during sputtering, the peaks associated with the Krytox lubricant were reduced in magnitude, and the peaks corresponding to NbO_2F became more prominent. Carbon was not detected in the subsurface layers corresponding to a depth of 100 nm. These results are consistent with the trends determined from Auger depth profiling (ref. 4) and from the x-ray line scans presented in figure 47. Eventually, as more of the fracture surface material was sputtered away with ion-milling, the resulting ESCA spectra only contained peaks representing niobium oxides. The similarity in the ESCA results obtained before and after ion-milling at various locations on the S/N 120 fracture surface suggests that the IGC was not progressive, which supports the hypothesis that the IGC occurred during manufacturing.

The fracture surface from a relief radius crack near bolt hole B in S/N 132 was also examined by ESCA. This was from a deeper crack than that analyzed in S/N 120, and the location of this cracked section within S/N 132 is illustrated in figure 49. It should be noted that reference 48 incorrectly identified this section as being adjacent to acoustic cavity number 16, when it was actually from the cross-hatched section in figure 49 between acoustic cavity numbers 17 and 18. The fracture surface analyzed from S/N 132 is shown in figure 76, and the specific areas that were analyzed by ESCA are indicated in the figure at locations A to G. The fracture surface is entirely intergranular, and no lab overload region is present in figure 76. Although the entire fracture surface examined in S/N 132 is oxidized, the spectra from the ESCA analysis indicate lower peak intensities for oxygen (and hence lower amounts of oxide) at the crack tip near locations C, D, and F, in comparison to those obtained from the crack tip in S/N 120. This result is consistent with the fractography and EDS results, which indicate some minimally oxidized areas in localized regions at the crack tip, previously shown in figures 66(d) and 67. Based on the ESCA spectra line positions, the types of oxides and oxy-fluorides present on the crack surface S/N 132 match those present on the intergranular crack surface of hole L in S/N 120. Evidence for the Krytox lubricant was also found based on additional peaks for fluorine and carbon in the ESCA spectra, although the lower intensity of these peaks indicates that less Krytox was present on the S/N 132 fracture surface compared to that of S/N 120. Moreover, ESCA results also indicate even lower quantities of the lubricant were present in S/N 132 at the crack tip locations D and F compared to the remainder of the S/N 132 fracture surface.

The presence of the PFPE lubricant on the crack surfaces of two thrusters is considered noteworthy, because Krytox 143AC has been shown to break down by reacting with surface oxides to produce metal fluorides (ref. 45). The metal fluorides are strong Lewis acids that further decompose the PFPE lubricant in an autocatalytic process; the smaller segments of the polymer chain react with moisture, and trace amounts of HF are released. Thermogravimetric analyses were performed and coupled to gas cell in a fourier transform infrared spectrometer (ref. 46), in order to confirm the expected reactions between Krytox 143AC and C–103 in the presence of moisture in an air environment. It was determined that the Krytox material unzips into smaller segment oligomers at temperatures close to the thruster bakeout temperature (ref. 46), and trace amounts of HF were detected after 23 min at 399 °C (750 °F). A similar compound, Fomblin Y, with an identical ESCA signature was also analyzed and was found to breakdown in an air environment at 299 °C (570 °F) in the presence of C–103 (ref. 46). The breakdown of either lubricant material would cause the release of small amounts of HF, which would have the potential of causing IGC in a manner similar to that which occurred by the preweld etchant during 316 °C (600 °F) bakeout. Testing of C–103 specimens produced IGC and surface features consistent with that observed in service after exposure to Krytox and heating to 316 °C (600 °F) for 72 hr (ref. 42). However, based on the ESCA analyses performed during ion-milling, the Krytox material appears to be located only in the top layers of the intergranular crack surface, suggesting that the Krytox may have been introduced after the crack formed and the crack surface became oxidized. It should also be noted that, based on the ESCA alone, it cannot be determined if any residual PFPE lubricant on the thruster hardware is still capable of being reactive upon exposure to elevated temperatures, because the breakdown products of the PFPE lubricant are expected to give similar signatures to the lubricant itself.

3.4.3 Summary and Conclusions From ESCA Analyses

The intergranular cracks did not form progressively over time.

(1) The same oxides (NbO and Nb_2O_5) were found across the fracture surface from the crack mouth to the crack tip in approximately the same volume fraction.

(2) Evidence was found for Krytox lubricant in the top layers of the fracture surface.

(3) Ion-milling showed similar depth profiling results through the thickness of the reaction products over the entire fracture surface: niobium oxides and Krytox were found on the surface; Krytox diminished as NbO_2F became more prominent beneath the surface layers; and niobium oxides were present beneath NbO_2F and above the parent material.

(4) Krytox migrates due to its low surface tension. Since it was found only on the surface and not in layers adjacent to the parent material, Krytox may have migrated into a preexisting relief radius crack.

Section 4: Exposures to Sodium Hydroxide via Oakite Rustripper Immersion

4.1 Background

During a chamber repair and rejuvenation process in March 2005 at WSTF, it was discovered that a small number of injector assemblies had been erroneously immersed in Oakite Rustripper (Oakite Products, Inc., Berkeley Heights, NJ) during a cleaning operation. This process had been occurring on all thruster chamber repair and rejuvenations since 1999 (ref. 58). Oakite Rustripper contains a nominal concentration of 13 wt% sodium hydroxide (NaOH), an alkali that is well known to embrittle niobium and its alloys by the absorption of hydrogen. Niobium is attacked by hot (98 °C (208 °F)) NaOH in concentrations from 1 to 10 wt% (refs. 18 and 36) and is also attacked at room temperature by NaOH in concentrations ranging from 1 to 40 wt% (refs. 35 to 37). As part of a prior failure investigation in 1979 on injector S/N 128 (ref. 55), it was demonstrated that long exposures of Oakite Rustripper caused intergranular and transgranular failures at 79 °C (175 °F) in notched C−103 tensile specimens that were preloaded to 414 MPa (60 ksi). More recent testing (ref. 59) showed some loss of ductility and mixed mode fractures with 4-hr exposures to Oakite Rustripper at 79 °C (175 °F), and severe embrittlement was observed after 20-hr exposures; however, no apparent degradation was observed during qualitative testing with 20 min rust stripper exposure times that approximated the process durations at WSTF.

The concern over the Oakite Ruststripper exposures became heightened after the NESC Materials SPRT reevaluated the results from fractography that had been conducted earlier at GRC and Boeing HB on S/N 120 and at GRC, LaRC, and MSFC on S/N 132. S/N 120 had been exposed to Oakite Rustripper during its chamber repair and rejuvenation in 2004, and had exhibited embrittlement in the form of transgranular cleavage on the lab-induced fracture surface that was well ahead of the intergranular cracks and adjacent to acoustic cavities. This was consistently observed on the opened crack surfaces in S/N 120, irrespective of the laboratory in which the fracture was induced, although only a limited number of lab openings had been performed on that injector. It was postulated that the Oakite Rustripper would have come into direct contact with the acoustic cavities during the immersion process, thereby promoting hydrogen absorption and diffusion of hydrogen in the regions where the brittle behavior was observed. In contrast, 16 sections were opened on S/N 132 at 3 different NASA centers, and 100 percent of these crack openings resulted in completely ductile features ahead of the intergranular crack and adjacent to the acoustic cavities. Injector S/N 132 was never exposed to Oakite Rustripper. Fracture behavior appeared at that time to be correlated with exposures to Oakite Rustripper.

Although less than 10 injector assemblies have actually undergone repair and rejuvenation processes at WSTF, 2 such injectors had been installed on OV−103 for STS−114, and thus had been exposed to Oakite Rustripper immersions. Thus, the concern was raised by the NESC Materials SPRT that existing intergranular thruster cracks might propagate during service into the regions between the intergranular crack tips and the acoustic cavities, where elevated hydrogen contents may exist due to these erroneous NaOH immersions. The fractographic evidence that was provided by the NESC Materials SPRT showed the potential adverse effect of sodium hydroxide and contributed to a flight constraint on OV−103 that was initiated by Safety and Mission Assurance. The fractographic evidence also provided the impetus for additional testing of thruster material.

4.2 Testing With Oakite Rustripper

An intensive testing program ensued at WSTF to address this concern regarding Oakite Rustripper immersions. Representatives from the Orbiter Materials and Processing Program and their contractors, Safety and Mission Assurance, and the NESC Materials SPRT participated directly in the mechanical testing and resultant fractography. Test specimens were machined from a fleet lead primary thruster injector in the following conditions: as-is with no Oakite Rustripper exposure; with 30-min Oakite Rustripper exposures performed at 79 °C (175 °F) in the chemical laboratory at WSTF; and with 20-min Oakite Rustripper exposures performed at 66 °C (150 °F) using equipment and procedures closely representing the nominal cleaning procedures at WSTF. Fleet leader specimens with and without Oakite Rustrippper exposures

exhibited ductile rupture and similar tear resistances based on load versus displacement curves, which suggests that the WSTF Oakite Rustripper immersions did not allow sufficient hydrogen absorption to degrade mechanical behavior. Similar testing was also conducted on S/N 120, both in the as-processed condition and after a subsequent 316 °C (600 °F)/48-hr bakeout. The WSTF testing showed only a slight drop in the tear resistance of the S/N 120 material compared to that of the fleet leader specimens, although these small differences could have been due to testing variability with a non-standard specimen design. Fractography of the tested S/N 120 showed mixed-mode fracture and small areas of 100 percent transgranular cleavage, which suggests that S/N 120 has been embrittled by elevated hydrogen levels. The source(s) of the apparent higher hydrogen content in S/N 120 could not be conclusively established, but it appeared that the hydrogen had accumulated from a variety of potential sources, and not solely from the WSTF repair and rejuvenation process. Subsequent tests conducted by the NESC Materials SPRT at LaRC indicated only a very small decrease in the fracture toughness and no significant change in the fatigue crack growth rate when the S/N 120 specimens were compared to the fleet leader specimens.

Therefore, it was concluded that the observed differences in behavior between S/N 120 and the fleet leader with and without Oakite Rustripper exposures were very small. As a result, the tests demonstrated that the C−103 material was not significantly affected by the 20-min Oakite Rustripper exposures at WSTF, and thus all thrusters given the Oakite Rustripper immersions during the chamber repair and rejuvenation were cleared for flight. However, since C−103 has the potential of being adversely affected by NaOH and by hydrogen uptake, it was recommended by the NESC Materials SPRT and Safety and Mission Assurance that the Oakite Rustripper immersion step be removed from the WSTF chamber repair and rejuvenation processing, in order to reduce the risk of additional hydrogen uptake in thrusters repaired in the future. As result of this recommendation, corrective action was taken, and an audit of the thruster repair and rejuvenation processes at WSTF was conducted.

4.3 Summary and Conclusions From Oakite Rustripper Testing

All thrusters given the Oakite Rustripper immersions during the chamber repair and rejuvenation were cleared for flight. Testing results indicated that the C−103 thruster material was not significantly affected by the 20-min Oakite Rustripper exposures at WSTF.

(1) Only a slight drop in the tear resistance, a very small decrease in the fracture toughness, and no significant change in the fatigue crack growth rate were observed in the S/N 120 material compared to that of the fleet leader specimens.

(2) Fractography of the tested S/N 120 showed mixed-mode fracture and small areas of 100 percent transgranular cleavage, which suggests that S/N 120 has been embrittled by elevated hydrogen levels but not sufficiently to degrade mechanical properties.

(3) Recent testing, 1979 testing, and literature data demonstrated that niobium alloys can be degraded significantly by NaOH under certain conditions, particularly by longer exposures.

(4) Due to the risk of additional hydrogen uptake in thrusters immersed in sodium hydroxide, a recommendation was made to remove Oakite Ruststripper immersions from the WSTF chamber repair and rejuvenation process.

Conclusions

1. RCS thruster intergranular cracking (IGC) is due to hydrogen embrittlement.
   a. Hydrogen production on C−103 is thermodynamically assured in the presence of hydrofluoric-acid-containing etchants.
   b. C−103 has been shown to be embrittled when charged with hydrogen.
   c. Dissolution processes (i.e., stress corrosion and hot-salt cracking) will not result in IGC for this C−103 material.
   d. Root cause identified in 1982 failure analyses was not substantiated.

2. Thruster IGC was produced during manufacturing as a result of processing of thrusters in the presence of fluoride-containing acids.
   a. Laboratory tests to simulate processing conditions have produced IGC with surface features consistent with that observed in service. These conditions included exposure to the niobium etchant (33%HF:33%HNO_3:33%H_2O) followed by a 316 °C (600 °F) exposure in air for 48 hr.
   b. Oxide features (termed as “popcorn”) have been observed on the fracture surfaces. These popcorn features have only been replicated in the presence of fluorine and oxygen when heated to temperatures greater than 204 °C (400 °F), suggesting that the thruster fracture surfaces were exposed to the processing bakeout.
   c. A fluorinated lubricant has been found on the fracture surfaces of serial numbers (S/Ns) 120 and 132. Krytox 143AC (DuPont, Wilmington, DE) is the fluorinated lubricant that is applied to the thrusters during processing. These lubricants have been shown to react with metal oxides and breakdown at thruster bakeout temperatures, thereby releasing small quantities of HF (refs. 45 and 46). New test results (ref. 42)

produced IGC and surface features consistent with that observed in service after exposure to Krytox and heating to 316 °C (600 °F) for 72 hr.

d. Failure analyses of cracked thrusters have shown cracking to be 100 percent intergranular. No change in fracture mode has been observed at the crack tip.

3. Appreciable environmental crack propagation does not occur after manufacturing.
   a. Examination of the oxide features has shown similar features from the crack mouth to the crack tip, and has provided no indication of appreciable (greater than 0.08 mm (0.003 in.)) crack propagation.
   b. The same oxides (NbO and Nb_2O_5) were found across the fracture surface from the crack mouth to the crack tip in approximately the same volume fraction. Depth profiling through the thickness of the reaction products on the IGC provided further confirmation that the reaction products did not change from the crack mouth to the crack tip.
   c. Laboratory tests to determine environmental crack propagation conditions during service have not revealed any crack growth. Here, specimens are exposed to the processing conditions (exposure to the niobium etchant and baked at 316 °C (600 °F) for 48 hr under stress) to produce IGC. The specimens are then exposed to a high humidity environment and monitored for crack propagation.

4. The C–103 thruster material was not significantly affected by the 20-min Oakite Rustripper exposures during the thruster repair and rejuvenation processes at WSTF. All thrusters given the Oakite Rustripper immersions during the chamber repair and rejuvenation were cleared for flight.
   a. Only a slight drop in the tear resistance, a very small decrease in the fracture toughness, and no significant change in the fatigue crack growth rate were observed in the S/N 120 material compared to that of the fleet leader specimens.
   b. Fractography of the tested S/N 120 showed mixed-mode fracture and small areas of 100 percent transgranular cleavage, which suggests that S/N 120 had been embrittled by elevated hydrogen levels but not sufficiently to degrade mechanical properties.
   c. Recent testing, literature data, and testing from 1979 all demonstrated that niobium alloys can be degraded significantly by NaOH under certain conditions, particularly by longer exposures.
   d. Due to the risk of additional hydrogen uptake in thrusters immersed in sodium hydroxide, a recommendation was made to remove Oakite Ruststripper immersions from the WSTF chamber repair and rejuvenation process.

References

1. Corrective Action Record AB3655–010, Rockwell International Space Division, page 7 of 9, Sept. 1982.
2. Corrective Action Record AC4684–010, Rockwell International Space Division, page 2 of 6, Nov. 1984.
3. Werner, Brian: RCS Thruster Injector Cracks. Boeing, April 12, 2004.
4. Tarkanian, Michael L.: Failure Analysis; Shuttle Orbiter RCS Primary Thruster, P/N 235216, S/N 120. Lab Report No. M&P–3–1597, Feb. 15, 2005.
5. Smithells, Colin James: Metals Reference Book, fifth ed., Butterworths, Boston, MA, 1976, p. 212.
6. Halides of Various Materials. Clarycon, www.clarycon.com, Jan. 2003. Accessed Dec. 9, 2005.
7. Korb, L.J.: Corrosion in the Aerospace Industry. Metals Handbook, ninth ed., vol. 13, ASM International, Metals Park, OH, 1987, p. 1058.
8. Tarkanian, Mike: Failure Analysis Results as of 6–25–04 Shuttle Orbiter RCS Primary Thruster S/N 120," Presented at RCS TIM, Huntington Beach, CA, June, 30, 2004.
9. The Marquardt Company, Material Specification No. MMS–2216, Columbium Alloy Rod, Bar, Billet, Extrusions, Wire, Shapes, Forging Stock, and Forgings (C–103), revised April 3, 1978.
10. Ryder, D.A.; Davies, T.J.; Brough, I.; and Hutchings, F.R.: General Practice in Failure Analysis. Metals Handbook, ninth ed., vol. 11, ASM, Metals Park, OH 1986, p. 15.
11. Titran, R.H., consultant to NASA Glenn Research Center, May 2004 (personal communication).
12. Luther, R.; Bechtel Bettis, Inc., June 24, 2004 (personal communication).
13. Yang, S., Boeing Rocketdyne, June 29, 2004 (personal communication).
14. Mahoney, M.W.; and Paton, N.E.: Effect of Oxygen, Nitrogen, and Hydrogen on the Mechanical Properties of Cb-752. J. Eng. Mater. Technol. Trans. ASME, 1974, pp. 201–206.
15. Farahani, M.M.; Attia, F.; and Salama, K.: Hydrogen Embrittlement in Single- and Poly-Crystal Niobium. Metall. Trans. A, vol. 12A, no. 4, 1981, pp. 631–638.
16. Spitzig, W.A.; Owen, C.V.; and Scott, T.E.: Effects of Nitrogen on the Mechanical Behavior of Hydrogenated V, Nb, and Ta. Metall. Trans. A, vol. 17A, 1986, pp. 527–535.
17. Fariabi, S.; Collins, A.L.W.; and Salama, K.: Effects of Hydrogen on Near-Threshold Crack Propagation in Niobium. Metall. Trans. A, vol. 14A, 1983, pp. 701–707.
18. Yau, T.L.; and Webster, R.T.: Corrosion of Niobium and Niobium Alloys. Metals Handbook, Ninth ed., vol. 13, ASM International, Metals Park, OH, 1987, pp. 722–724.
19. Hardie, D.; and McIntyre, P.: Low-Temperature Embrittlement of Niobium and Vanadium by Both Dissolved and Precipitated Hydrogen. Metall. Trans., vol. 4, no. 5, 1973, pp. 1247–1254.
20. Matsui, H.; Yoshikawa, N.; and Koiwa, M.: In Situ Observation of Hydrogen Induced Crack in Niobium. Acta Metall., vol. 35, no. 2, 1987, pp. 413–426.
21. Gahr, S.; Grossbeck, M.L.; and Birnbaum, H.K.: Hydrogen Embrittlement of Nb—Macroscopic Behavior at Low Temperatures. Acta Metall., vol. 25, no. 2, 1977, pp. 125–134.

22. Grossbeck, M.L.; and Birnbaum, H.K.: Low Temperature Hydrogen Embrittlement of Niobium—Microscopic Observations. Acta Metall. vol. 25, no. 2, 1977, pp. 135–147.
23. Gahr, S.; and Birnbaum, H.K.: Hydrogen Embrittlement of Niobium—High Temperature Behavior. Acta Metall., vol. 26, no. 11, 1978, pp. 1781–1788.
24. Spitzig, W.A.; Owen, C.V.; and Scott, T.E.: Effects of Interstitials and Hydrogen-Interstitial Interactions on Low Temperature Hardening and Embrittlement in V, Nb, and Ta. Metall. Trans. A, vol. 17A, no. 7, 1986, pp. 1179–1189.
25. Jagannadham, K.; Armstrong, R.W.; and Hirth, J.P.: Low Energy Cleavage Fracture Associated With the Hydrogen Embrittlement of Refractory Metal Alloys. Mat. Sci. Eng., vol. A113, nos. 1–2, 1989, pp. 339–366.
26. Kirchheim, R.; and Hirth, J.P.: Hydrogen Adsorption at Cracks in Fe, Nb, and Pd. Scripta Metall., vol. 16, no. 4, 1982, pp. 475–478.
27. Walter, R.J.; Bentle, G.G.; and Chandler, W.T.: Effect of Water Vapor/Hydrogen Environments on Niobium, B–66 Niobium Alloy, Tantalum, and Ta-10W Alloy. Corrosion, 1991, pp. 272–280.
28. Kerlins, Victor; and Phillips, Austin: Modes of Fracture. ASM Handbook, vol. 12, 1987, pp. 12–71.
29. Parkins, R.N.: Mechanistic Aspects of Stress Corrosion Cracking. Parkins Symposium on Fundamental Aspects of Stress Corrosion Cracking, 1992, pp. 3–40.
30. Parkins, R.N.: Stress Corrosion Cracking. Proceedings of the First International Conference on Environment-Induced Cracking of Metals, NACE, 1990, pp. 1–19.
31. Abe, S.; and Kaneko, M.: Corrosion of Grain Boundaries in Iron—Chromium—Nickel Alloys. Parkins Symposium on Fundamental Aspects of Stress Corrosion Cracking, 1992, pp. 389–398.
32. Yang, S.: Objectives of C-ring Testing. Presented at Technical Interchange Meeting on RCS Thrusters, Boeing Rocketdyne report, Dec. 13, 2004.
33. Korb, L.J.: Logic for RCS Thruster Buyoff. Boeing Huntington Beach Report, Nov. 15, 2004.
34. Craig, Benjamin D.: Environmentally-Assisted Cracking: Comparing the Influence of Hydrogen, Stress, and Corrosion on Cracking Mechanisms. AMPTIAC Quarterly, vol. 9, no. 1, 2005, pp. 17–24.
35. Gerardi, S.: Niobium. Metals Handbook, 10th ed., vol. 2, ASM International, Materials Park, OH, 1990, pp. 565–571.
36. Graham, R.A.; and Sutherlin, R.C.: Niobium and Niobium Alloys in Corrosive Applications. Niobium, Science and Technology, International Symposium on Niobium 2001, Orlando, FL, 2001, Niobium 2001 Ltd., Bridgeville, PA, 2002, pp. 337–355.
37. Fontana, Mars Guy; and Greene, Norbert D.: Corrosion Engineering. McGraw-Hill Book Company, New York, NY, 1967, p. 178.
38. Gileadi, E.; Kirowa-Eisner, E.; and Penciner, J.: Interfacial Electrochemistry: An Experimental Approach. Addison-Wesley Publishing Co., Reading, MA, 1975, pp. 471–493.
39. Subramanyan, P.K.: Comprehensive Treatise of Electrochemistry. Plenum Press, New York, NY, 1981, pp. 411–462.
40. Jones, Russell H.: Stress-Corrosion Cracking, ASM International, Materials Park, OH, 1992, pp. 13–17.
41. Craig, Bruce: Hydrogen Damage. ASM Handbook, vol. 13A, ASM International, Metals Park, OH, 2003, pp. 367–380.
42. Castner, B.; and Jacobs, J.: C–103 Crack Reproduction Studies. Presented to RCS Thruster Materials and Processing Team, March 31, 2005 (teleconference).
43. Gangloff, Richard P., et al.: Direct Current Electrical Potential Measurement of the Growth of Small Cracks. Small-Crack Test Methods, ASTM STP–1149, ASTM, Philadelphia, PA, 1992, pp. 116–168.
44. Pawel, R.E.; Cathcart, J.V.; and Campbell, J.J.: Columbium Metallurgy. Proceedings of Symposium of AIME, Interscience Publishers, New York, NY, 1961, p. 667.
45. Jones, William R., Jr.: The Properties of Perfluoropolyethers Used for Space Applications. NASA TM–106275, 1993.
46. Sutter, J.K.; Scheiman, D.; and Capadona, L.: TGA–FTIR of Fomblin, Krytox, and Krytox With Niobium Alloy. April 19, 2005 (unpublished results).
47. Kelly, T.: Boeing WSTF, March 23, 2005 (personal communication).
48. Sueme, D.R.: Examination of RCS Thruster S/N 132 Injector Cracks (CAR AE2746), Boeing HB Report, Nov. 2, 2004.
49. Chou, Y.T.; and Wei, R.P.: Dilation Field in Front of a Moving Crack. Scripta Metall., vol. 6, no. 10, 1972, pp. 965–968.
50. Fitzgerald, E.J.: RCS Primary Thruster Rationale for Flight. Presented at Orbiter Project Office Tagup, Johnson Space Center, June 1, 2005.
51. Curtis, C.: United Space Alliance. Materials and Processes RCS Thruster Technical Interchange Meeting #2, Huntington Beach, CA, Dec. 15, 2004.
52. Shin, K.S.; Austin, N.J.; and Kim, S.S.: Effect of Hydrogen on Mechanical Behavior of a 2090 Al-Li Alloy. Hydrogen Effects on Material Behavior, Neville R. Moody and Anthony W. Thompson, eds., TMS, Warrendale, PA, 1990, pp. 1023–1031.
53. Pressouyre, G.M.: Trap Theory of Hydrogen Embrittlement. Acta Metall., vol. 28, no. 7, 1980, pp. 895–911.
54. Reid, M.: Boeing Rocketdyne, Nov. 2004 (unpublished results).
55. Failure Investigation Intergranular Crack Causing Injector Flange Leakage—T.A. P/N 235216, S/N 128, F.M.R. No. 779–056, S–1494, MPM No. 18.343, July 1979 (The Marquardt Company Process Memorandum).
56. Bahl, M.K.: ESCA Studies of Some Niobium Compounds. J. Phys. Chem. Sol., vol. 36, no. 6, 1975, pp. 485–491.
57. Fontaine, R., et al.: Chemical ESCA Shift in Niobium Oxide Series. J. Electron Spectrosc. Relat. Phenom., vol. 10, no. 4, 1977, pp. 349–357.
58. Kelly, T.: Boeing WSTF. Presented to RCS Thruster Materials and Processing Team, March 24, 2005 (teleconference).
59. Jacobs, J.: RCS Thruster Processing Escape: Oakite Rustripper. Presented to RCS Thruster Materials and Processing Team, April 21, 2005 (teleconference).

Glenn Research Center
National Aeronautics and Space Administration
Cleveland, Ohio, December, 2005

TABLE I.—ORIGINAL SPECIFICATIONS FOR NIOBIUM INJECTOR MATERIAL

Element	Nominal composition		Permitted variation
	Minimum	Maximum	(Under minimum or over maximum)
Hafnium	9.0 wt%	11.0 wt%	0.15 wt%
Titanium	0.7 wt%	1.3 wt%	0.07 wt%
Zirconium		0.7 wt%	0.05 wt%
Tungsten		0.5 wt%	0.03 wt%
Tantalum		0.5 wt%	0.05 wt%
Carbon		150 ppm	None
Oxygen		225 ppm	None
Nitrogen		150 ppm	None
Hydrogen		15 ppm	None
All others		3000 ppm	None
Niobium		Balance	

Grain size of forgings shall be predominantly ASTM–E112 5 or finer with occasional grains as large as 3 permissible.
Hardness (Rockwell B): 70–95

TABLE II.—OPEN CIRCUIT POTENTIALS (E_{OC}) for C–103 AND Ti-6Al-4V

	E_{OC} (V vs. SCE) C–103	E_{OC} (V vs. SCE) Ti-6Al-4V	E_{OC} (V vs. SCE) C–103/ Ti-6Al-4V couple	E_r* (V vs. SCE) Water reduction
Dilute HF (pH ≈ 3.5)	–0.478	–1.076	–1.010	–0.451
1 wt% NaCl	–0.383	–0.280	–0.355	–0.625

*E_r (water reduction) = –0.241 V_{SCE} – (0.06 V × pH).

TABLE III.—SCRATCH POTENTIALS ($E_{scratch}$) AND CALCULATED HYDROGEN FUGACITY (f_{H_2}) for C–103 IN THE DILUTE HF AND 1 wt% NaCl SOLUTIONS

	$E_{scratch}$ (V vs. SCE) C–103	E_r* (V vs. SCE) Water reduction	f_{H_2} (atm) C–103 scratch	f_{H_2} (atm) C–103 open circuit
Dilute HF (pH ≈ 3.5)	–0.910	–0.451	2×10^{15}	7.94
1 wt% NaCl	–1.285	–0.625	1×10^{22}	8.58×10^{-9}

*E_r (water reduction) = –0.241 V_{SCE} – (0.06 V × pH)

TABLE IV.—UNIAXIAL TENSION TESTING FOR ENVIRONMENTAL CRACKING

Specimen	Solution	Exposure stress	Bakeout	Failure	Microscopy
1	$HF/H_20/NaCl$	≈ 198 MPa (28.8 ksi) –900 mV_{SCE}	None	Failure < 40.5 hr	Nearly 100 percent cleavage
2	$HF/H_20/NaCl$	≈ 177 MPa (25.6 ksi) –750 mV_{SCE}	None	Failure 26.5 hr	Nearly 100 percent cleavage
3	HF/H_20	≈ 177 MPa (25.6 ksi) –750 mV_{SCE} 24 hr	None	Strained to failure	Embrittled zone visible No intergranular cracking or cleavage
4	HF/H_20	≈ 177 MPa (25.6 ksi) –600 mV_{SCE} 48 hr	177 MPa (25.6 ksi) 316 °C (600 °F) 48 hr	Strained to failure	Embrittled zone visible No intergranular cracking or cleavage
5	HF/H_20	≈ 39.8 MPa (5.76 ksi) –1 V_{SCE} 90 hr	None	Strained to failure Failed in grip section	Transgranular cleavage plus intergranular cracking
6	HF/H_20	≈ 39.8 MPa (5.76 ksi) –1 V_{SCE} 90 hr	39.8 MPa (5.76 ksi) 316 °C (600 °F) 17 hr	Strained to failure	Ductile rupture
7	HF/H_20	No load –1 V_{SCE} 90 hr	None	Strained to failure Failed in grip section	Nearly 100 percent cleavage
8	HF/H_2O	No load –1 V_{SCE} 90 hr	None	Strained to failure Failed in grip section	Nearly 100 percent cleavage
9	HF/H_2O	No load –1 V_{SCE} 90 hr	26.5 MPa (3.85 ksi) 316 °C (600 °F) 17 hr	Strained to failure	Intergranular cracking up to 0.25 mm along outer surface
10	$HF/H_20/NaCl$	≈ 221 MPa (32.0 ksi) –100 mV_{SCE} 91.5 hr	None	Uniform attack	No observed local attack

TABLE V.—SUMMARY OF CRACK MEASUREMENTS FROM POLISHED SURFACES

S/N 132 10° slice	NASA center	Degrees from AC number 1	Projected crack depth, in.	Percent of total distance to acoustic cavity (projected crack depth), percent	Actual crack depth, in.	Ligament distance to acoustic cavity, in.	Angle of crack (degrees CCW from acoustic cavity wall)
AA	GRC	50	0	0	0	0.195	No crack
BB	MSFC	60	0	0	0	No cavity	No crack
CC polished side	LaRC	70	0	0	0	No cavity	No crack
CC opposite side	LaRC	80	N/A	>50	N/A	No cavity	~135
DD	GRC	80	0.125	58	0.166	0.092	132
EE	MSFC	90	0.080	48	0.107	0.087	131
FF remnant[a]	LaRC	107	0.208	90	0.295	0.023	135
GG	GRC	155	0.216	94	0.286	0.015	133
HH	LaRC	175	0.057	N/A	0.065	No cavity	144
II	MSFC	205	0.139	80	0.208	0.035	138
JJ	GRC	225	0.145	72	0.190	0.055	131
KK max. crack polished side	LaRC	240	0.123	79	0.160	0.032	140
KK opposite side	LaRC	250	0.113	66	0.148	0.058	139
LL	MSFC	260	0.096	48	0.133	0.106	134
MM	LaRC	275	0.113	68	0.156	0.053	136
NN	GRC	295	0.181	68	0.236	0.085	133
OO	MSFC	325	0.166	99	0.228	0.002	133
PP max. crack polished side	LaRC	335	0.172	99	0.217	0.002	142
PP opposite side	LaRC	345	0.041	N/A	0.080	N/A	120
QQ	GRC	345	0.052	24	0.069	0.164	132
RR remnant[a]	GRC	358	0.014	8	0.016	0.161	116

[a]Remnants are less than 10°.

TABLE VI.—SUMMARY OF CRACK MEASUREMENTS FROM OPENED CRACK FACES

S/N 132 10° slice	NASA center	Approx. degrees from AC number 1 for cut section	Maximum projected crack depth, in.	Maximum actual crack depth, in.	Minimum ligament distance to acoustic cavity, in.	Ligament distance to acoustic cavity at maximum crack depth, in.
AA	GRC	55	0	0	N/A	N/A
BB	MSFC	65	0	0	N/A	N/A
CC	LaRC	75	0.152	0.215	0.093	0.093
DD	GRC	85	0.105	0.115	0.071	0.071
EE	MSFC	95	0.151	0.199	0.016	0.016
FF remnant[a]	LaRC	104	0.193	0.273	0.019	0.057
GG	GRC	160	0.214	0.300	0	0.028
HH	LaRC	170	0.119	0.146	0.065	0.065
II	MSFC	210	0.146	0.229	0.033	0.087
JJ	GRC	220	0.197	0.236	0.021	0.066
KK	LaRC	245	0.122	0.159	0.047	0.070
LL	MSFC	255	0.095	0.154	0.062	0.062
MM	LaRC	280	0.132	0.184	0.023	0.039
NN	GRC	290	0.190	0.262	0	0.020
OO	MSFC	330	0.165	0.249	0	0.060
PP	LaRC	340	0.154	0.196	0.031	0.045
QQ	GRC	350	0.066	0.083	0.099	0.099
RR remnant[a]	GRC	356	N/A	N/A	N/A	N/A

[a]Remnants are less than 10°.

TABLE VII.—ELECTRON SPECTROSCOPY FOR CHEMICAL ANALYSIS DATA FROM RELIEF RADIUS CRACK NEAR BOLT HOLE L OF S/N 120

	Low oxide line (Nb3d5/2)		High oxide line (Nb3d3/2)	
Sample location	Position, eV	Percentage	Position, eV	Percentage
A	204.8	65.4	210.5	34.6
B	203.9	71.9	209.5	28.1
C	[a]202.0	[a]83.7	210.3	16.2
D	204.4	81.7	210.4	18.3
E	204.4	71.8	210.5	28.2
F	204.4	65.2	210.3	34.7

[a]Line position indicates metallic Nb.

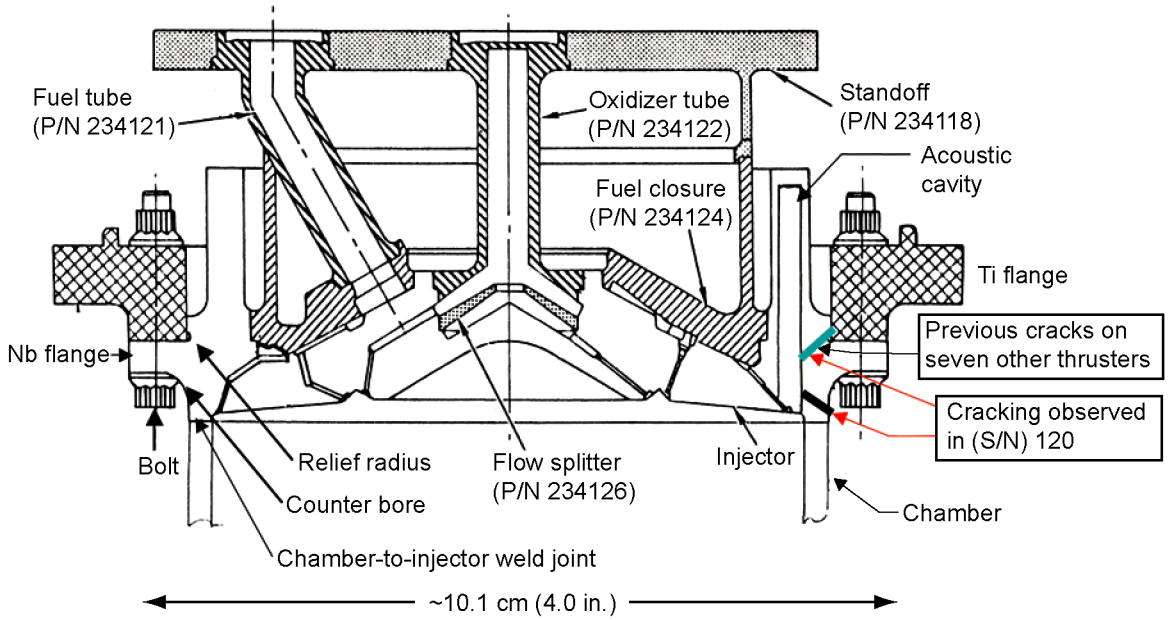

Figure 1.—Schematic of RCS thruster injector (from ref. 3, reprinted with permission from Boeing).

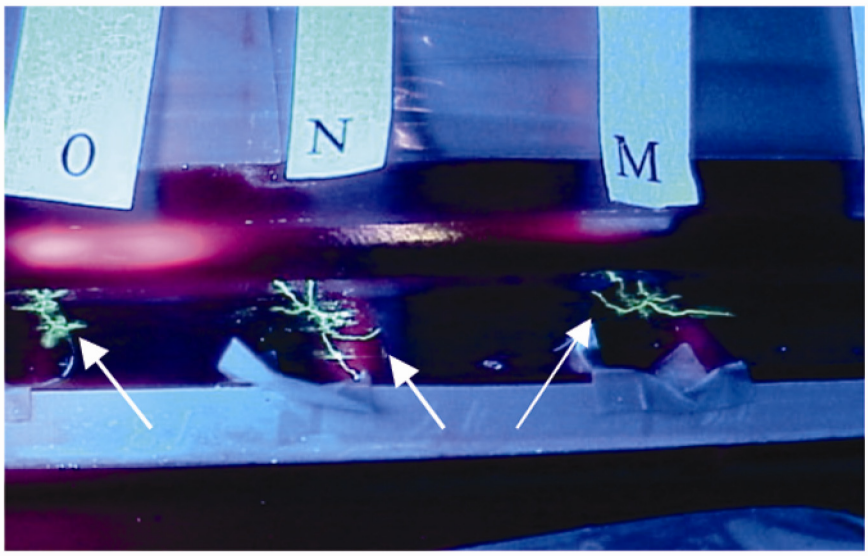

Figure 2.—Cracks in three counter bores are indicated by arrows (from ref. 4, reprinted with permission from Boeing). Counter bores from holes M, N, and O are shown.

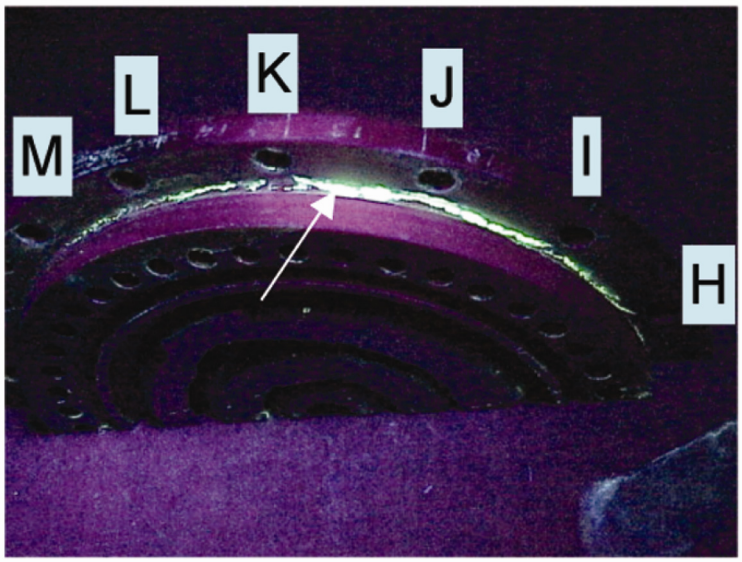

Figure 3.—Relief radius cracking is evident over a large fraction of the injector circumference (from ref. 4, reprinted with permission from Boeing) near holes H through M.

Figure 4.—Portion of S/N 120 that was set aside for failure analysis. Counter bores and bolt holes are labeled H through O (from ref. 4, reprinted with permission from Boeing).

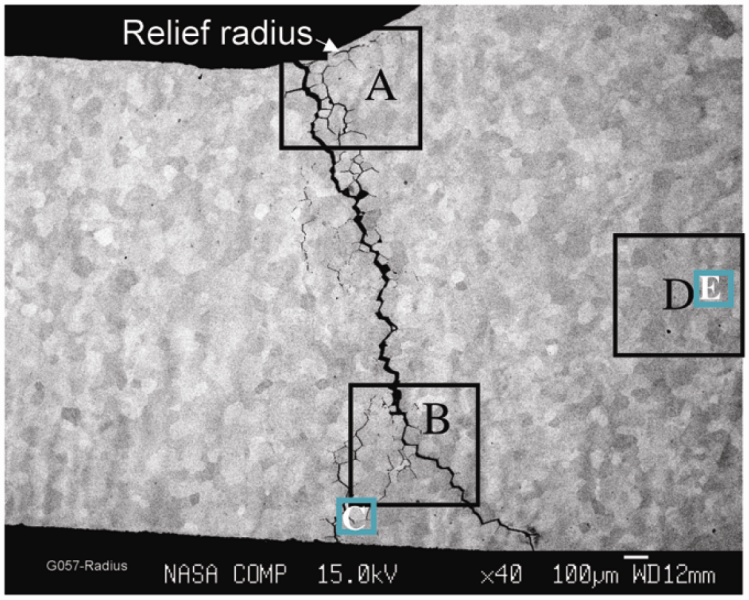

Figure 5.—Large crack in relief radius near hole J is shown. Areas A through E were selected for microprobe analyses to examine cracked areas near (A) and away (B and C) from the surface, as well as uncracked areas (D and E). Area dot maps were obtained at magnifications of 200× in locations A, B, and D and at 1000× in locations C and E.

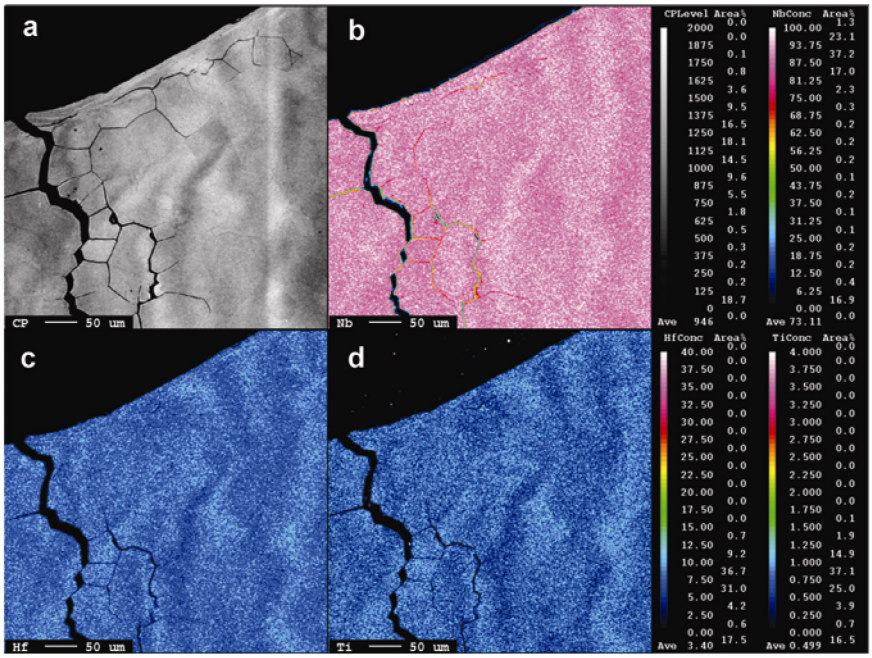

Figure 6.—Microprobe dot maps showing relief radius crack near hole J at surface for location A in figure 5. (a) Backscattered electron image and levels of (b) niobium, (c) hafnium, and (d) titanium. Brighter areas in b, c, and d indicate higher concentrations of each element; qualitative levels are shown in the keys on the right.

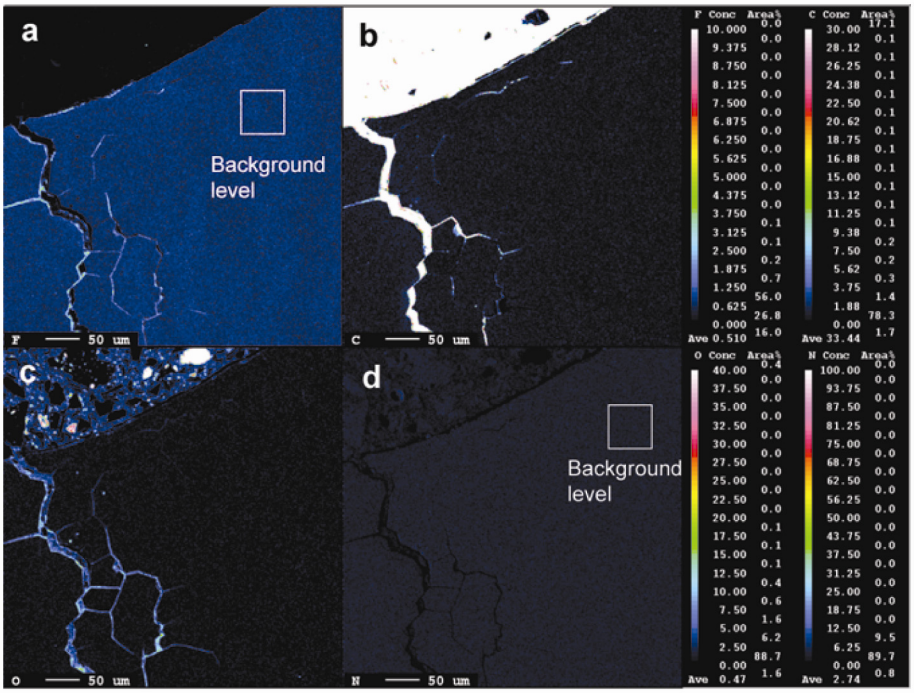

Figure 7.—Microprobe dot maps showing relief radius crack near hole J at the surface (location A) and levels of (a) fluorine, (b) carbon, (c) oxygen, and (d) nitrogen. Brighter areas indicate higher concentrations of each element; qualitative levels are shown in the keys on the right.

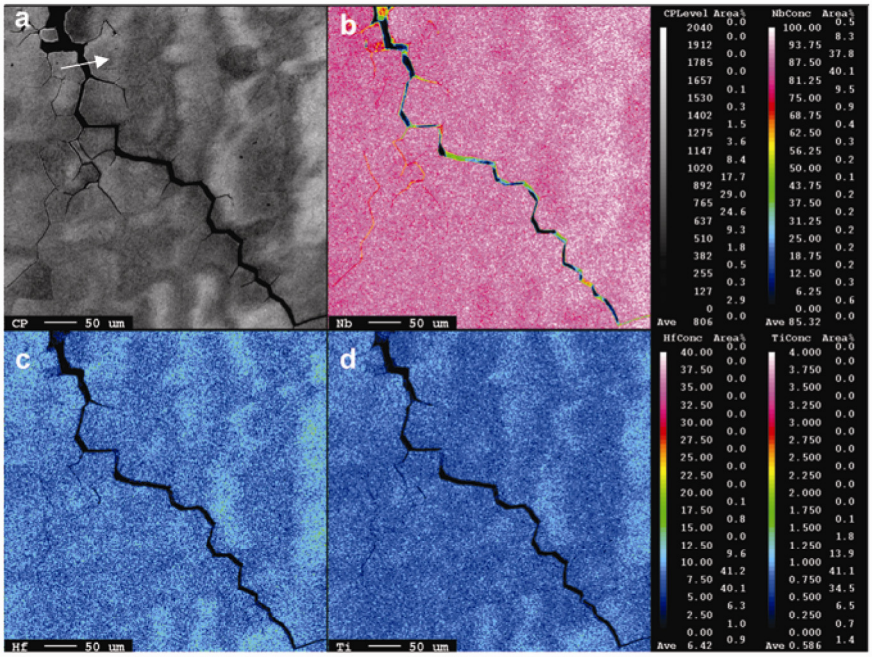

Figure 8.—Microprobe dot maps showing relief radius crack near hole J at location B, approximately 1.8 mm (0.07 in.) away from surface. (a) Backscattered electron image and levels of (b) niobium, (c) hafnium, and (d) titanium. Brighter areas indicate higher concentrations of each element. Qualitative levels are shown in the keys on the right. Subsequent line scans were performed and typical orientations of line scan with respect to the crack direction is indicated by arrow in (a).

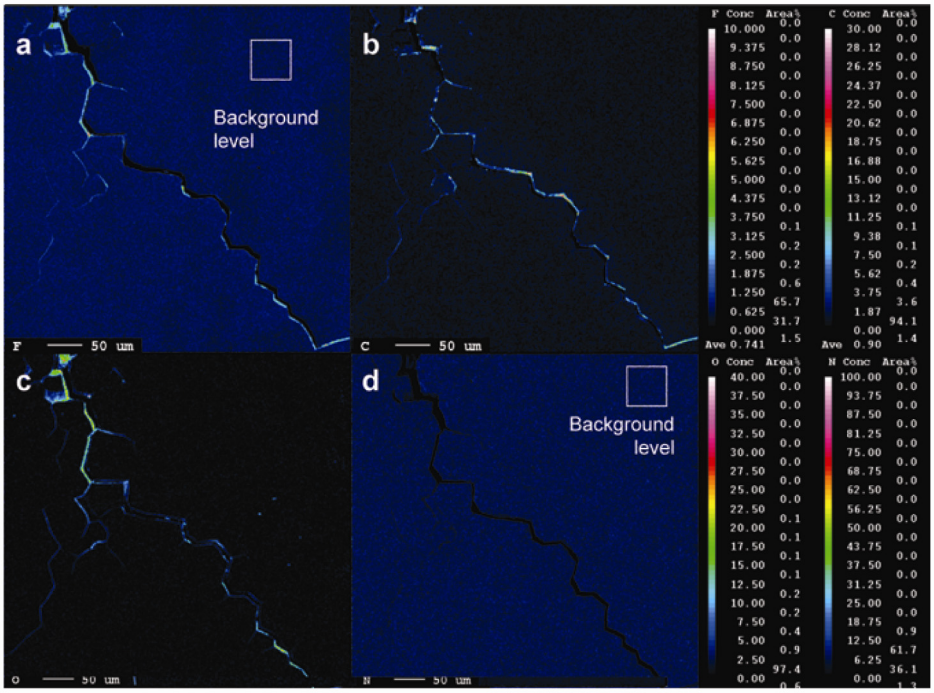

Figure 9.—Microprobe dot maps showing relief radius crack near hole J at location B, approximately 1.8 mm (0.07 in.) away from surface. Levels of (a) fluorine, (b) carbon, (c) oxygen, and (d) nitrogen. Brighter areas indicate higher concentrations of each element. Qualitative levels are shown in the keys on the right.

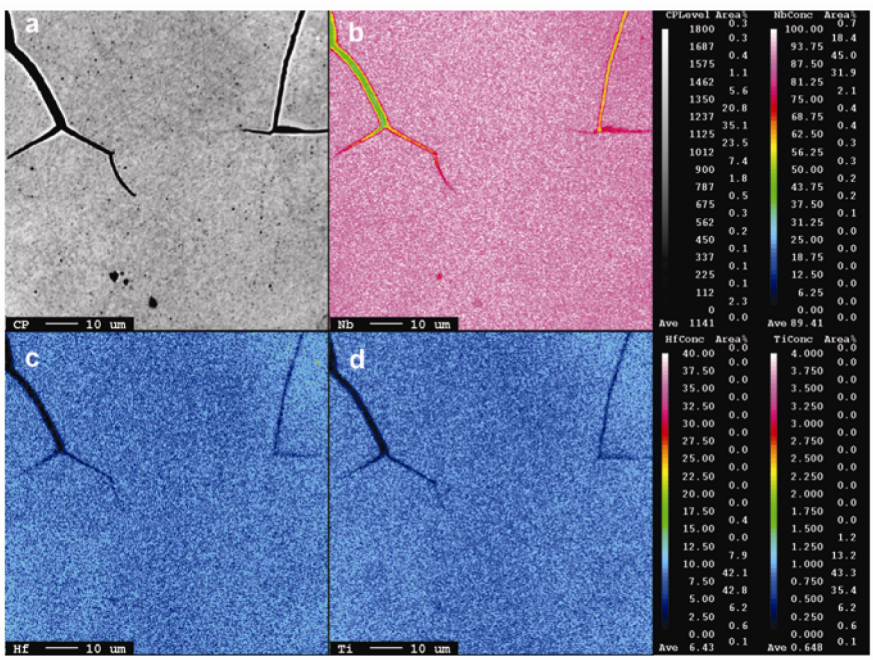

Figure 10.—Microprobe dot maps showing terminations of branches of relief radius crack near hole J at location C approximately 1.8 mm (0.07 in.) away from relief radius surface. (a) Backscattered electron image and levels of (b) niobium, (c) hafnium, and (d) titanium. Brighter areas indicate higher concentrations of each element. Qualitative levels are shown in the keys on the right.

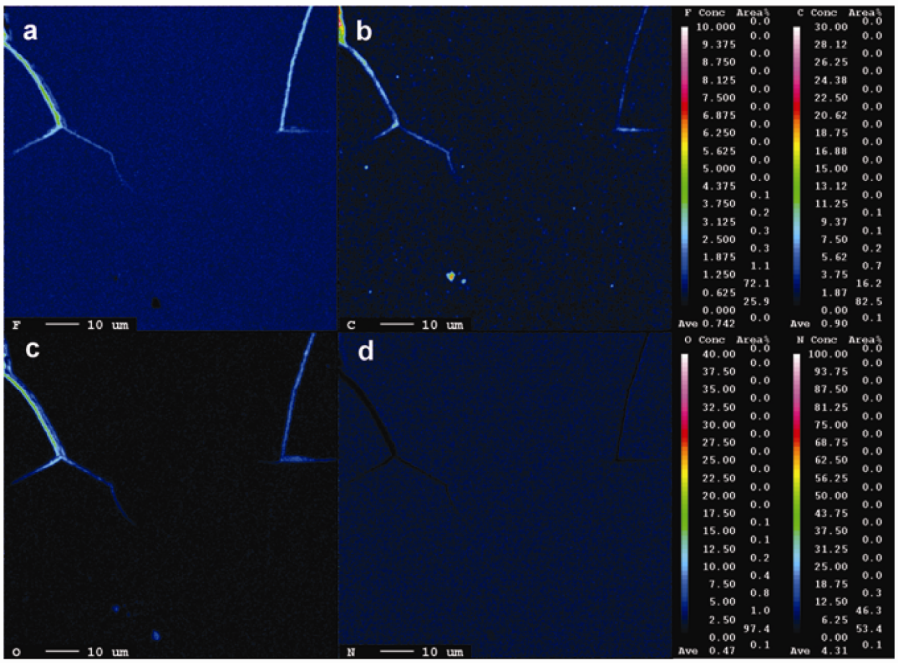

Figure 11.—Microprobe dot maps showing terminations of branches of relief radius crack near hole J at location C, approximately 1.8 mm (0.07 in.) away from relief radius surface. Levels of (a) fluorine, (b) carbon, (c) oxygen, and (d) nitrogen. Brighter areas indicate higher concentrations of each element. Qualitative levels are shown in the keys on the right.

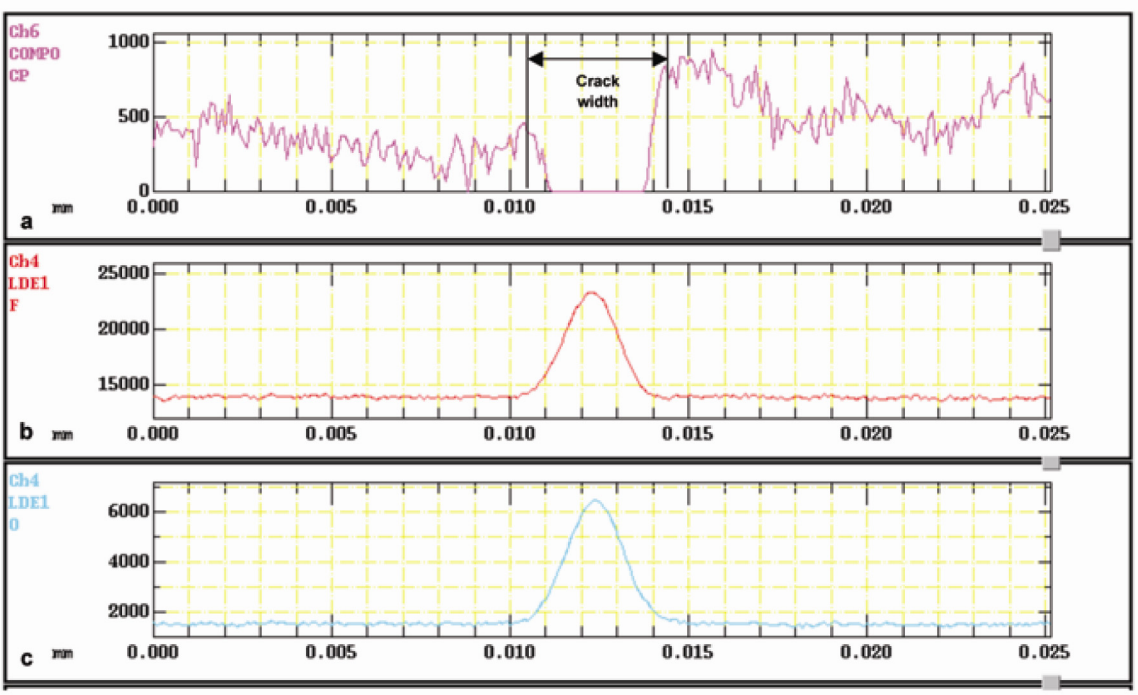

Figure 12.—Line scan analyses of intergranular crack in S/N 120 showing counts versus distance in millimeters for (a) gray scale, backscattered electron image with approximate crack width delineated; (b) fluorine; and (c) oxygen.

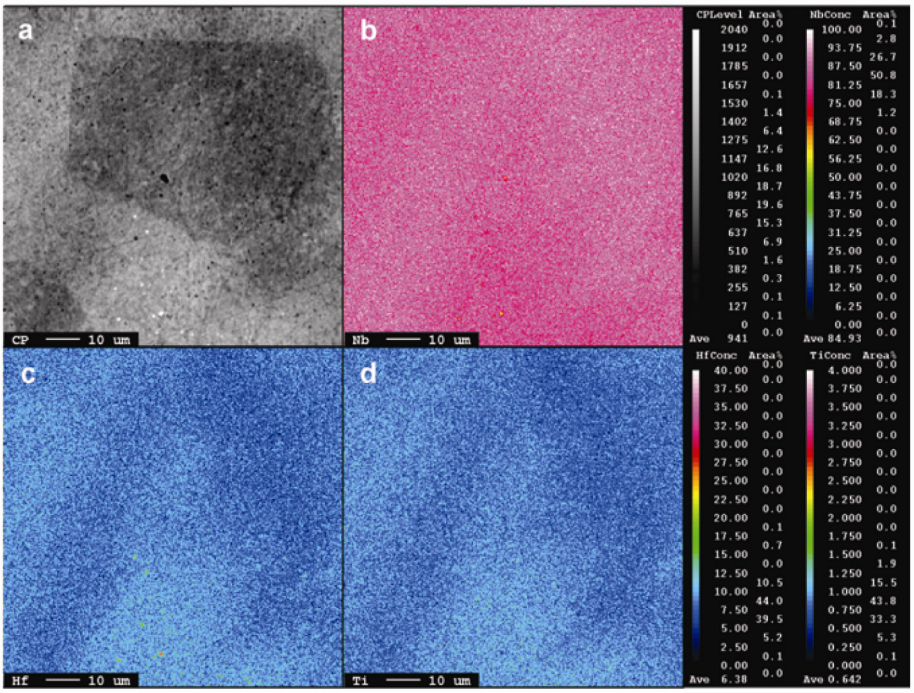

Figure 13.—Microprobe dot maps showing region away from relief radius crack near hole J at location E. (a) Backscattered electron image and levels of (b) niobium, (c) hafnium, and (d) titanium. Brighter areas indicate higher concentrations of each element. Qualitative levels are shown in the keys on the right.

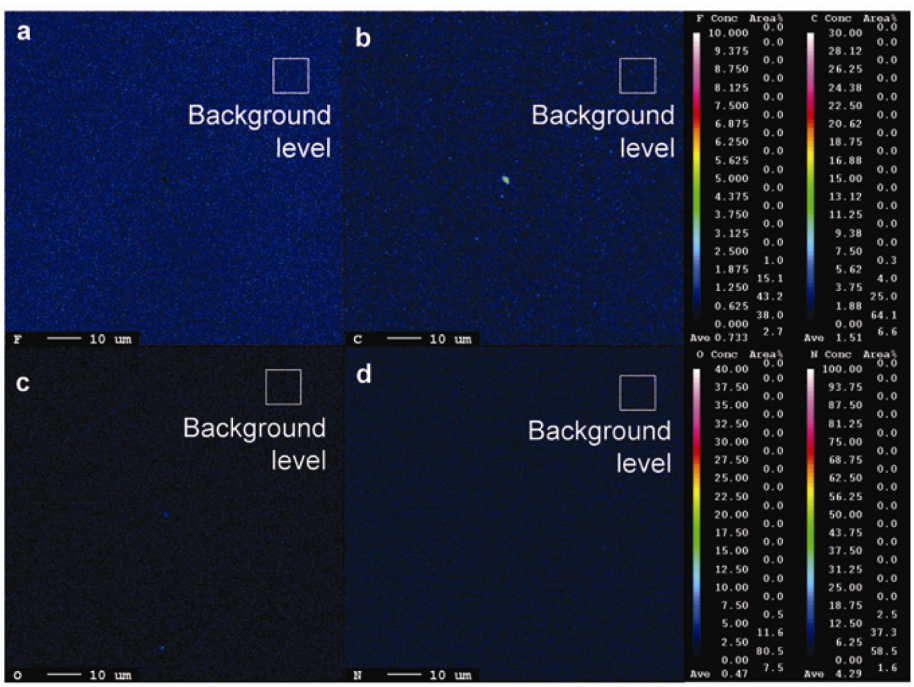

Figure 14.—Microprobe dot maps showing region away from relief radius crack near hole J at location E. Levels of (a) fluorine, (b) carbon, (c) oxygen, and (d) nitrogen. Brighter areas indicate higher concentrations of each element. Qualitative levels are shown in the keys on the right.

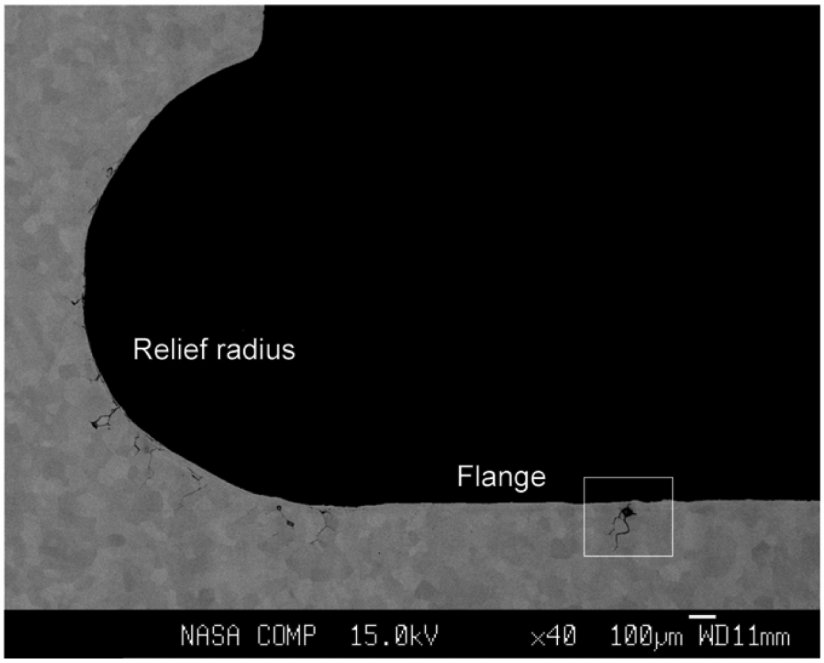

Figure 15.—Backscattered electron image showing region in vicinity of relief radius near bolt hole H. Several shallow, intergranular cracks are evident near the machined surface of the relief radius and injector flange. Area for dot mapping is indicated by the white box.

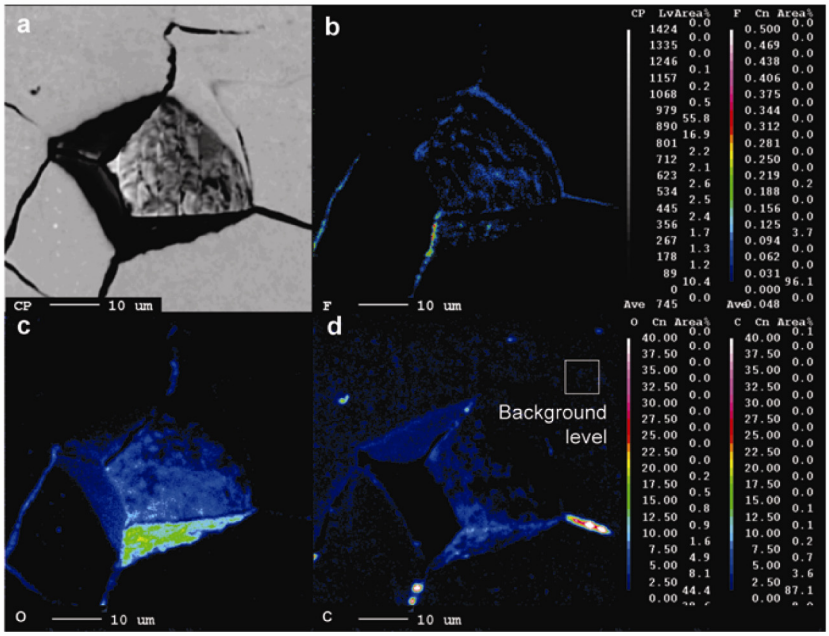

Figure 16.—(a) Backscattered electron image of a cracked region on the flange near hole H. Image shows a void left behind by a grain that fell out during metallographic preparation, which enabled broad surfaces of the grain boundaries surrounding that grain to be analyzed. Microprobe dot maps are given for (b) fluorine, (c) oxygen, and (d) carbon; brighter areas indicate higher concentrations of each element. Qualitative levels are shown in the keys for each element on the right.

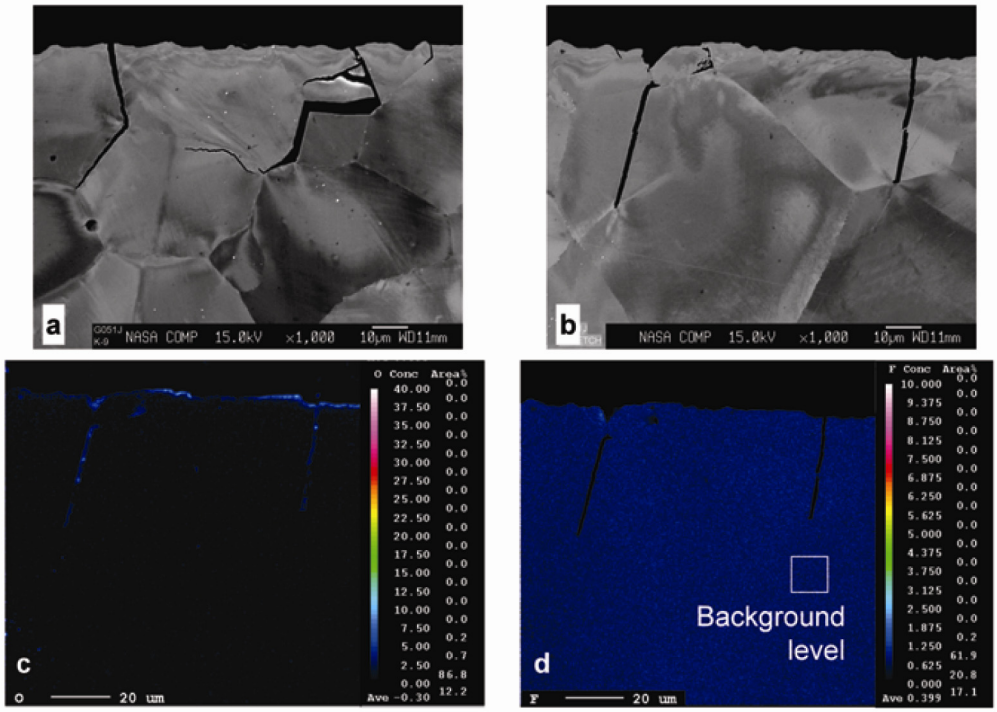

Figure 17.—Backscattered electron images of (a) intergranular cracks and (b) transgranular cracks in the counter bore of bolt hole K. Microprobe dot maps for (c) oxygen and (d) fluorine from the field of view in (b).

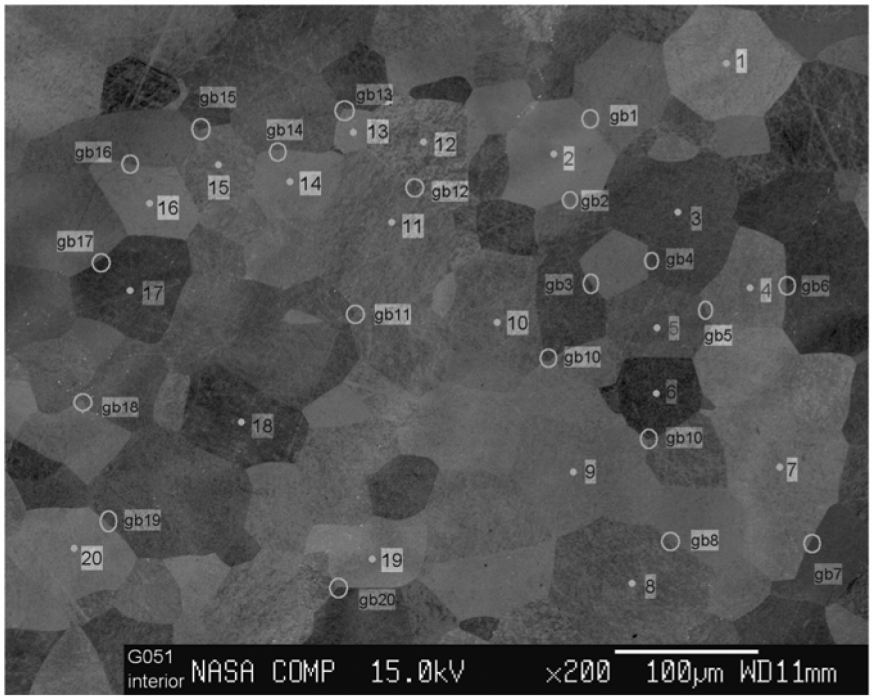

Figure 18.—Backscattered electron image of grain structure in uncracked region near counter bore of bolt hole K. Forty locations for quantitative point analyses by microprobe are indicated at grain boundaries and within grain interiors.

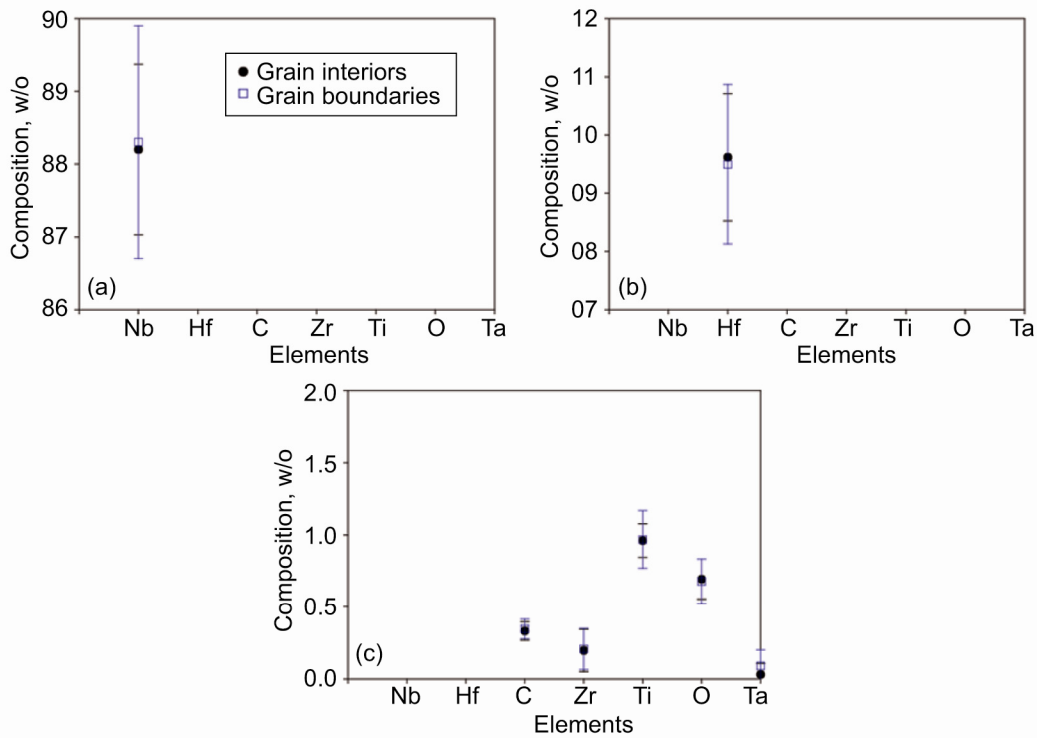

Figure 19.—Composition levels for (a) niobium (Nb), (b) hafnium (Hf), and (c) carbon (C), zirconium (Zr), titanium (Ti), oxygen (O), and tantalum (Ta) in an uncracked region near counter bore of bolt hole K. Filled circles represent data obtained within grain interiors and unfilled squares represent data from grain boundaries. Forty locations are represented by these data, which show no evidence for chemical segregation of the major, minor, and interstitial elements in uncracked C–103.

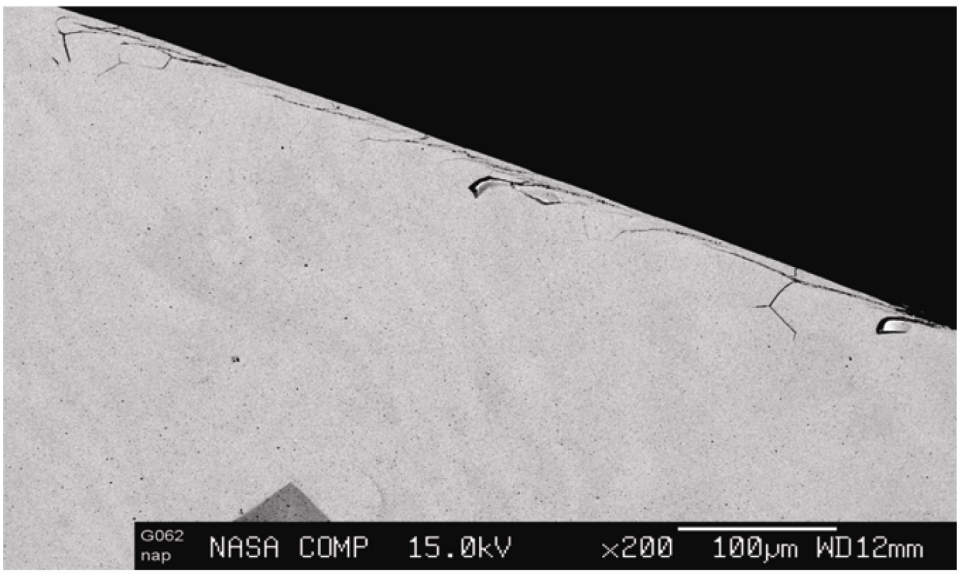

Figure 20.—Backscattered electron image of cracking observed in the 316 °C/207 MPa (600 °F/30 ksi) C-ring test specimen. Cracks are typically up to two grains deep and are also evident running parallel to the surface, beneath the cold-worked region from the machined surface. Specimen supplied by S. Yang at Boeing Rocketdyne.

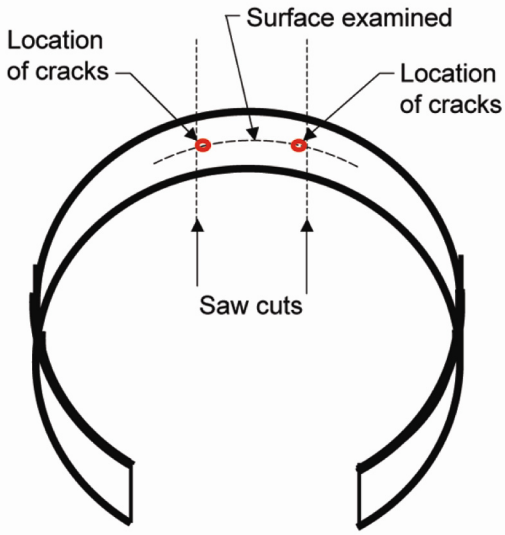

Figure 21.—Schematic illustrating the C-ring test specimen for attempted reproduction of hot-salt cracking. Cracks were examined from section having complete coverage of hot salt and applied stress at the maximum tensile stress. Cracks were consistently located near saw cut ends (within red circles) and were never observed along the tensile surface in the middle of the sample.

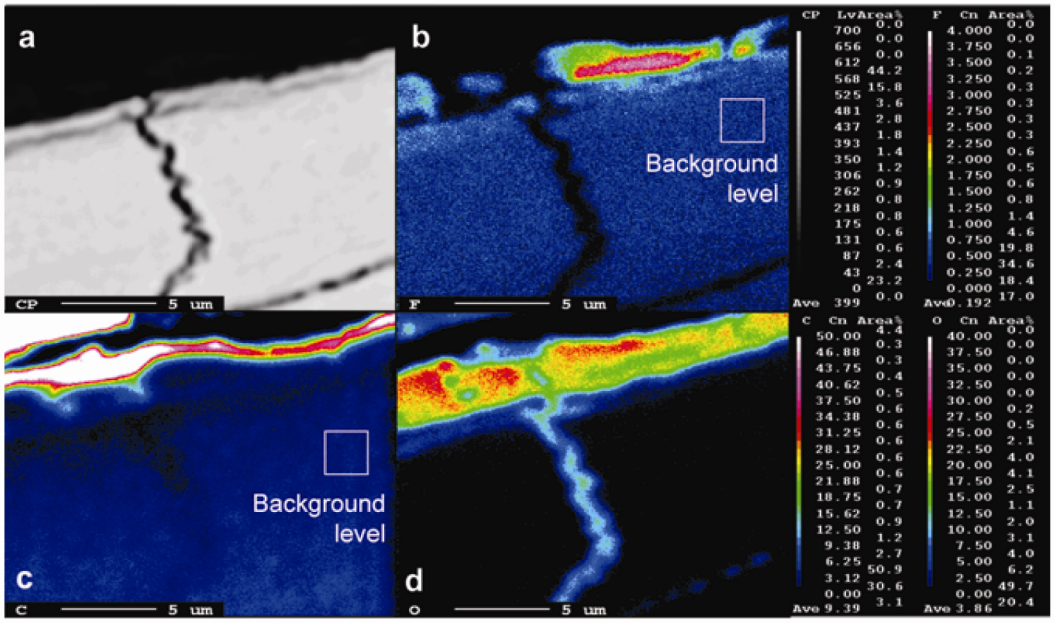

Figure 22.—(a) Backscattered electron image showing surface-connected cracking in 316 °C (600 °F) C-ring test specimen for reproduction of hot-salt cracking. Electron microprobe dot maps shown for (b) fluorine, (c) carbon, and (d) oxygen. Unlike S/N 120, the C-ring test specimen showed no fluorine within the surface-connected cracks.

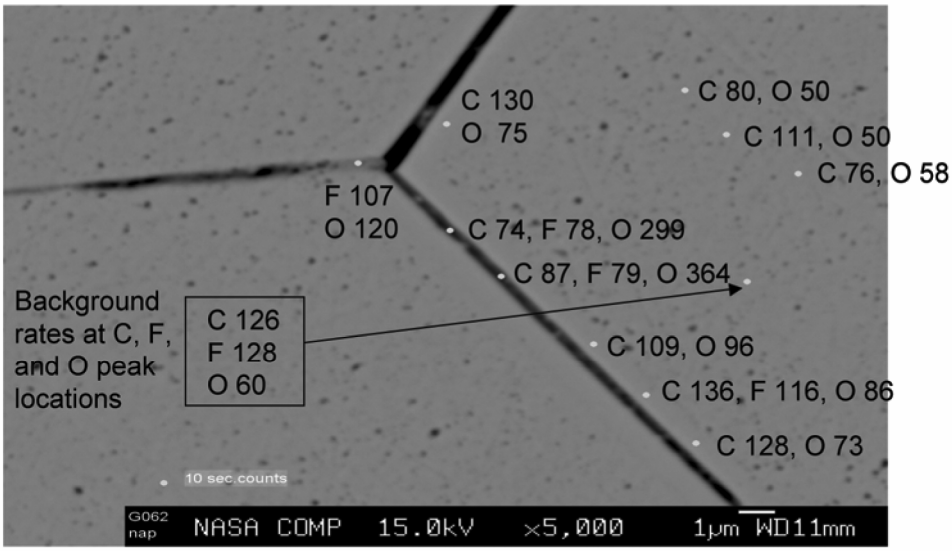

Figure 23.—Electron microprobe count rates from various locations in 316 °C (600 °F) C-ring specimen indicate that higher oxygen (O) levels were present within the cracks. Elevated levels of carbon (C) and fluorine (F) were not found within the cracks when compared to background rates for C and F peak locations. Count rates provided were obtained from a 10-sec analysis for each element at each point in the microstructure.

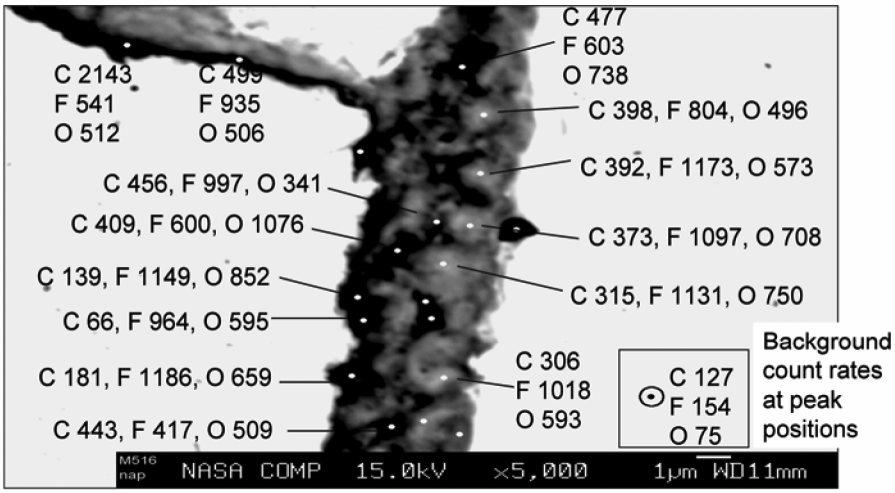

Figure 24.—Electron microprobe count rates are given for carbon (C), fluorine (F), and oxygen (O) for numerous locations within the relief radius crack in S/N 120 near bolt hole J. The C, F, and O rates within the crack are significantly higher than the background count rates at the C, F, and O peaks. Note that the intergranular crack in S/N 120 is significantly wider than that within the 316 °C (600 °F) C-ring specimen.

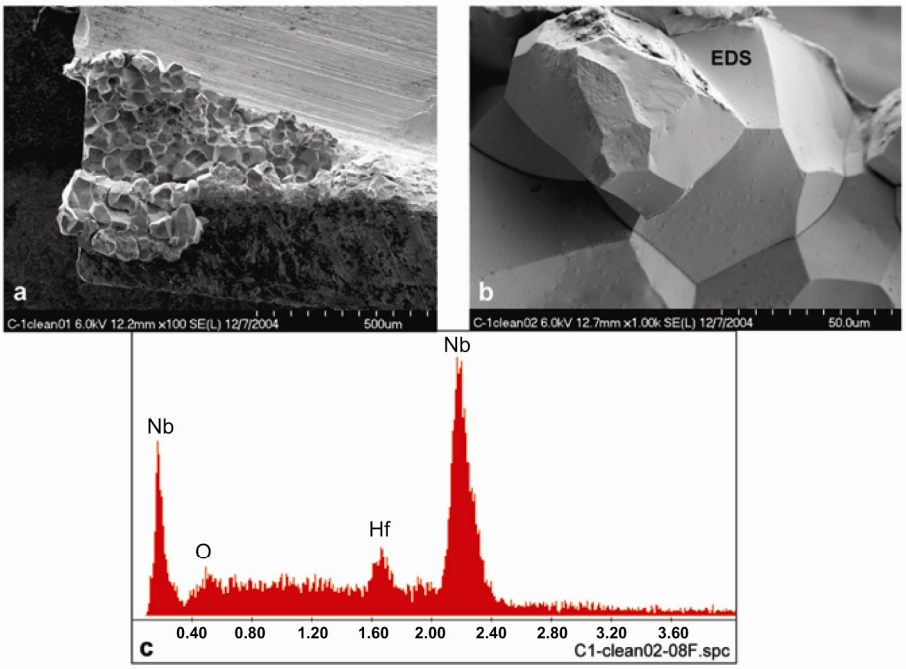

Figure 25.—Opened intergranular crack from 316 °C/207 MPa (600 °F/30 ksi) C-ring test: (a) overall view at low magnification; (b) higher magnification view of crack surface showing the absence of reaction products and Energy Dispersive Spectroscopy (EDS) label indicating grain facet analyzed by EDS; and (c) EDS scan showing low oxygen (O) peak and no fluorine (F) peak. EDS scan is similar to that for baseline C–103 material.

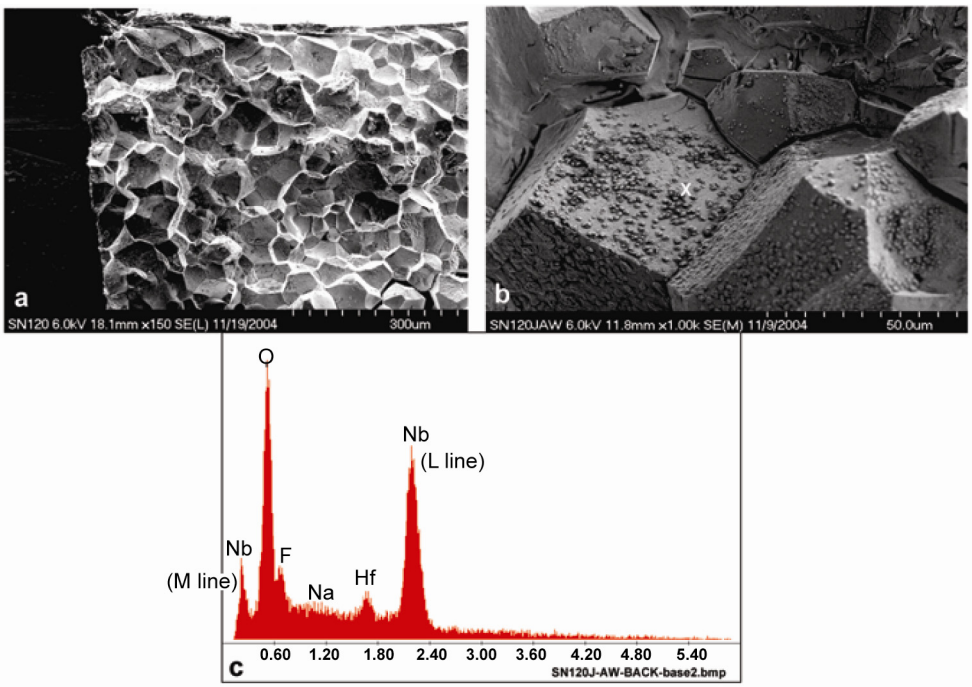

Figure 26.—Opened intergranular crack from relief radius near hole J of S/N 120: (a) low magnification view; (b) higher magnification view of crack surface showing the reaction products and grain facet analyzed (at location X) by Energy Dispersive Spectroscopy (EDS); and (c) typical EDS scan showing high O peak and presence of F peak.

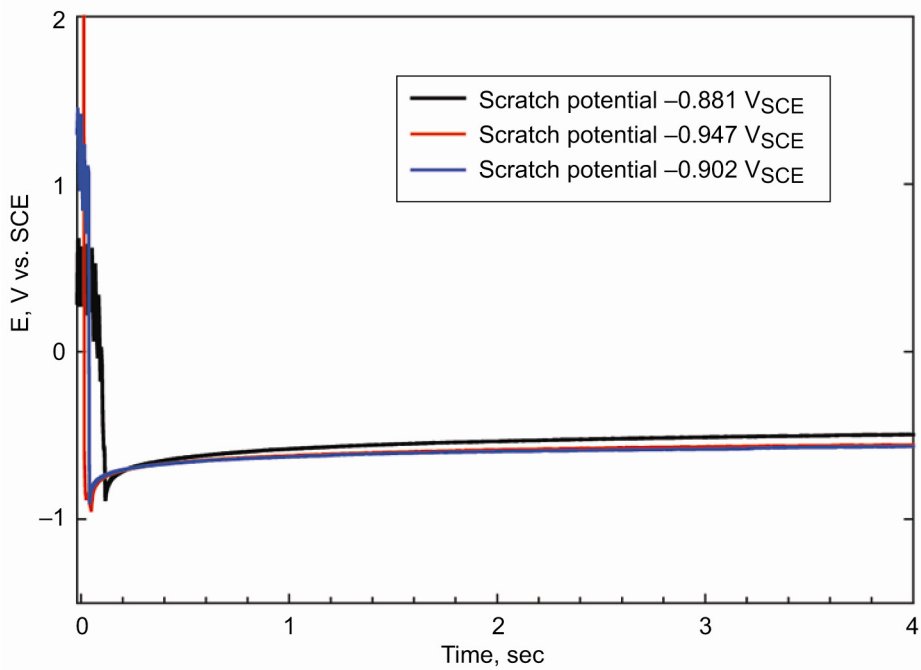

Figure 27.—Potential transients for three scratch tests of C–103 in dilute HF solution.

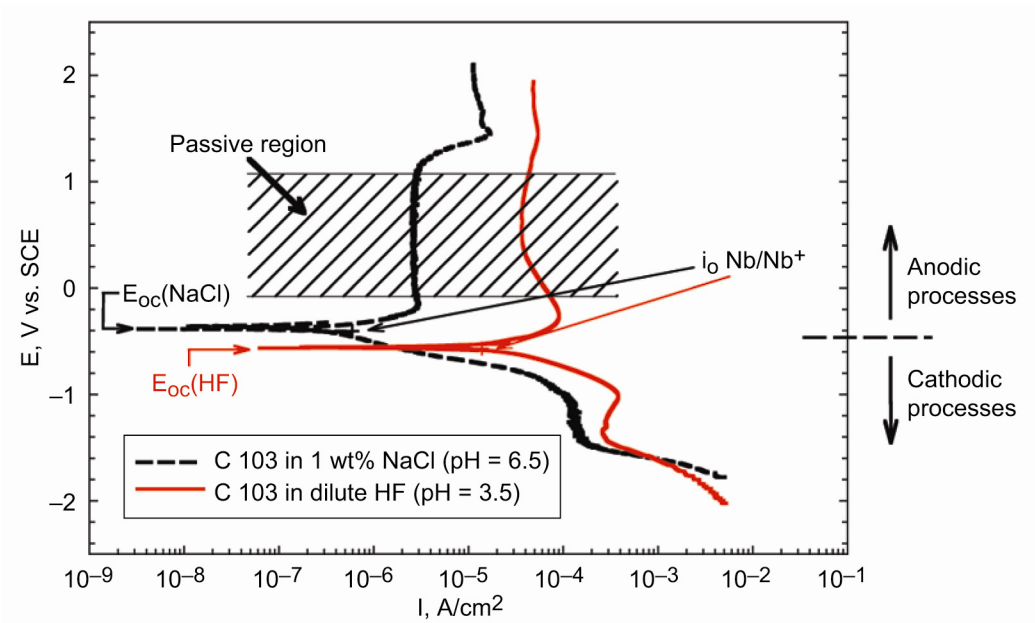

Figure 28.—Polarization curves for C–103 in dilute HF and 1 wt% NaCl solutions.

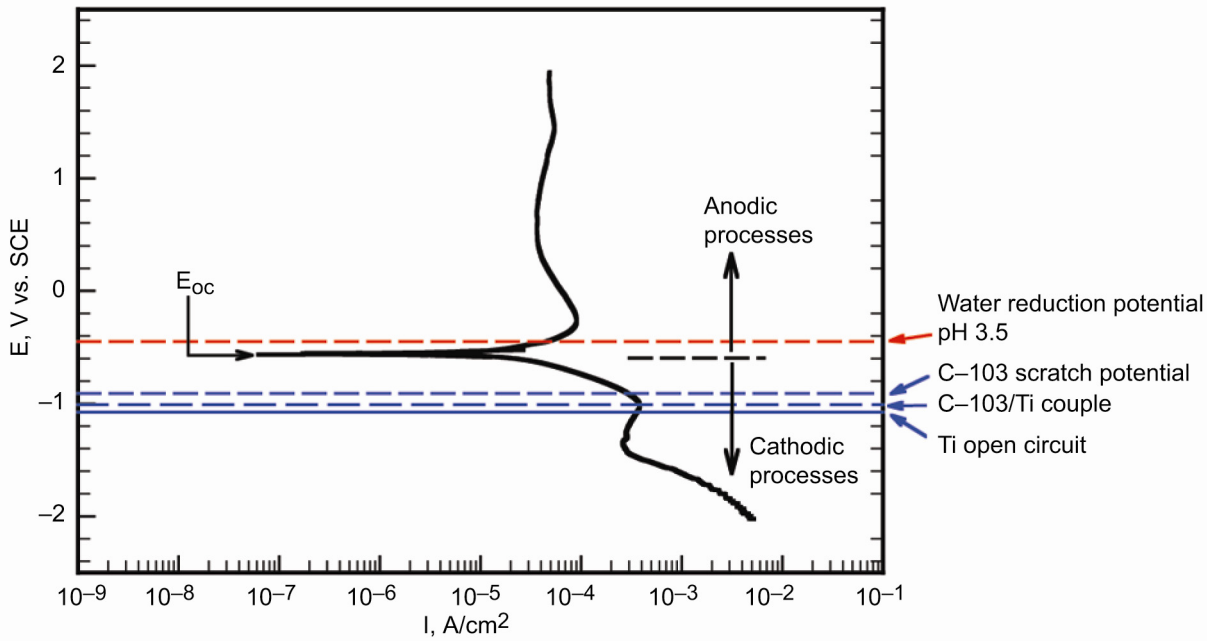

Figure 29.—Polarization curve for C–103 in dilute HF solution.

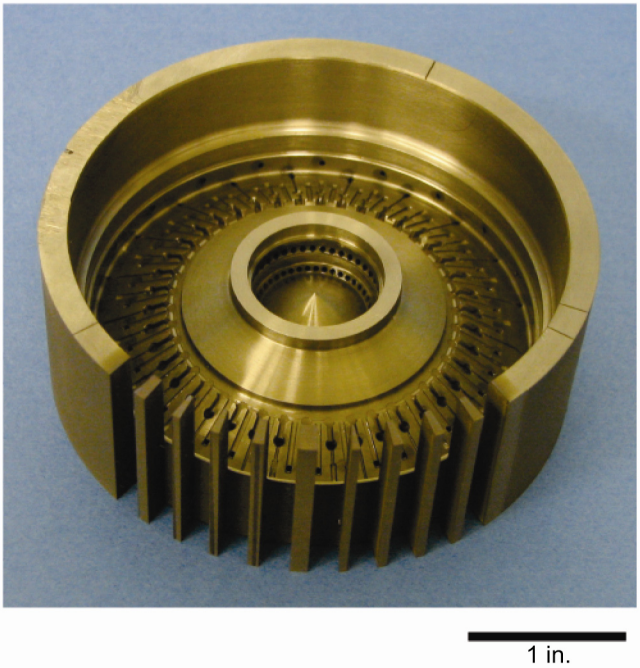

Figure 30.—A partially machined RCS thruster injector was used to produce mechanical test specimens. In this view, material has been removed to produce 10 mechanical test specimens.

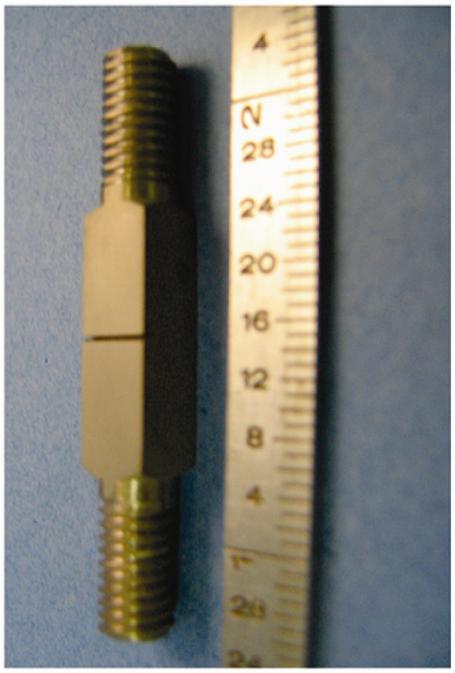

Figure 31.—Uniaxial test specimen used in this study.

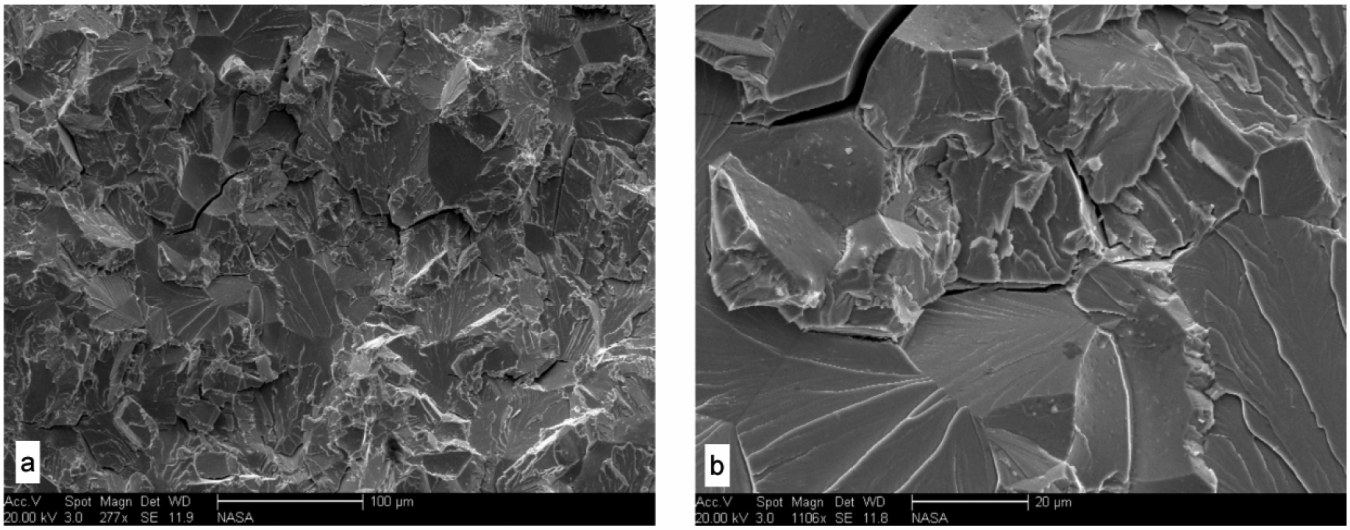

Figure 32.—Fracture surface for a uniaxial tension specimen (specimen 2) exposed to dilute HF solution and loaded to 25.6 ksi at –750 mV_{SCE}. Specimen failed after 26.5 hr of exposure.

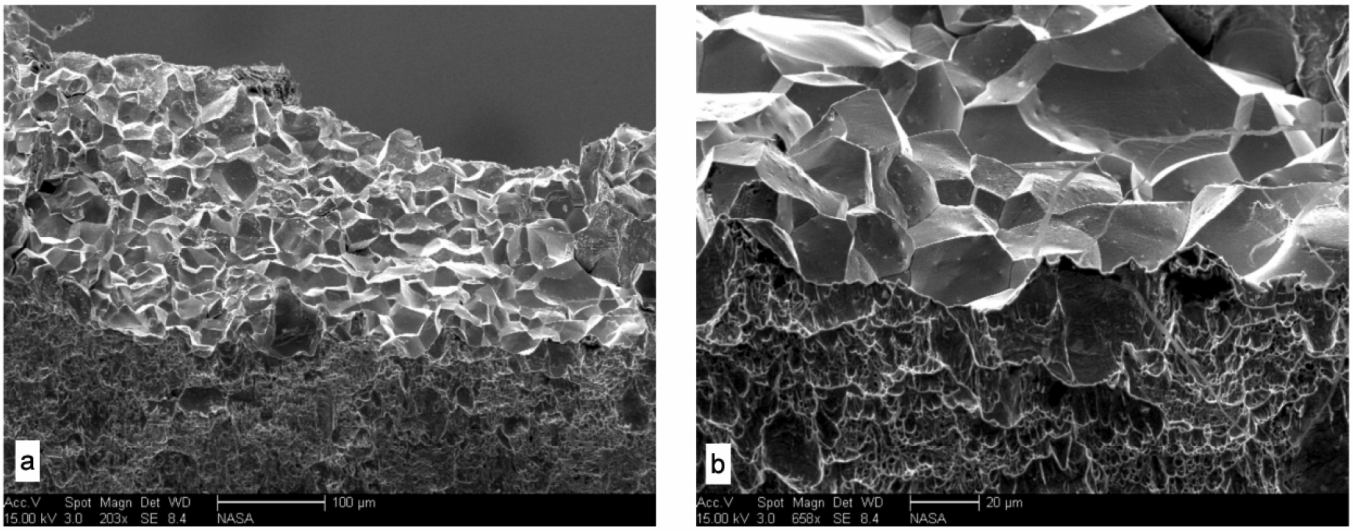

Figure 33.—Fracture surface for a uniaxial tension specimen (specimen 9) exposed to a dilute HF solution without any applied load for 90 hr at –1 V_{SCE}. Specimen was then baked at 316 °C (600 °F) for 17 hr under an applied load of 54 kg (120 lb) and then strained to failure. Periphery of fracture surface exhibits intergranular fracture, while majority of fracture surface (internal regions) shows ductile failure.

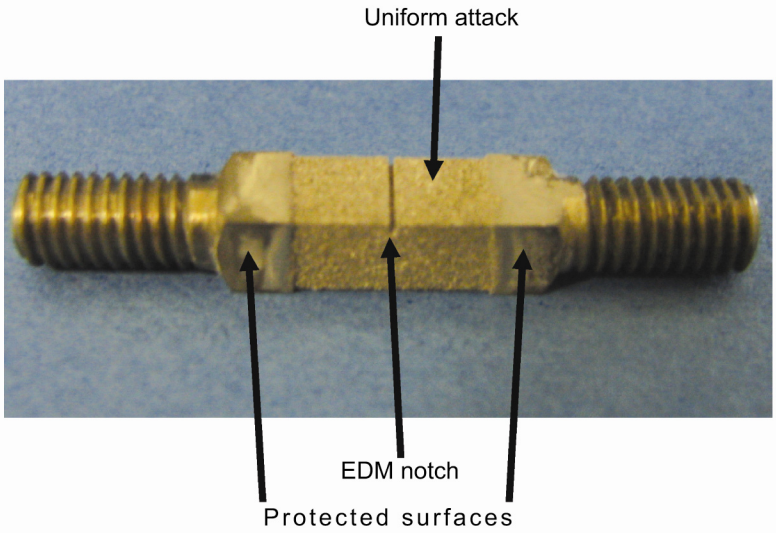

Figure 34.—Uniaxial test specimen (specimen 10) exposed to dilute HF solution and under load at 221 MPa (32 ksi) at –100 mV_{SCE} for 91.5 hr. Specimen exhibits extensive corrosion, but no cracking was observed.

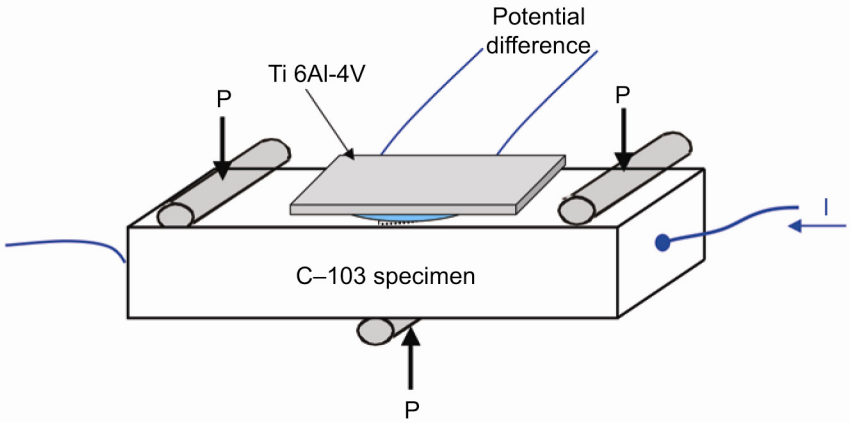

Figure 35.—Schematic illustrating bend testing of C–103 material.

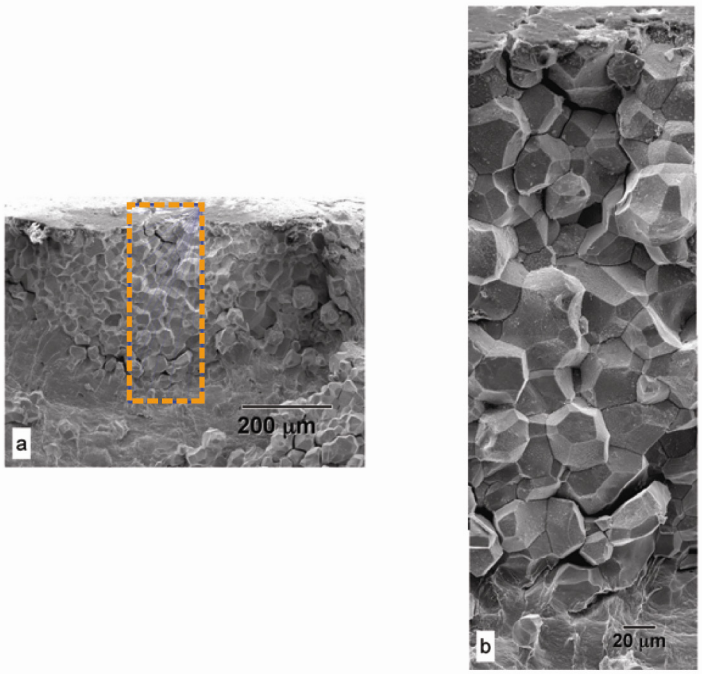

Figure 36.—(a) Overall fracture surface and (b) higher magnification view of a C–103 bend specimen exposed to a dilute niobium etchant solution loaded to 276 MPa (40 ksi) for 36 hr, baked at 316 °C (600 °F) for 48 hr, and exposed to >70% relative humidity for 7 days at room temperature. The applied bending load of 276 MPa (40 ksi) was maintained during bakeout and during subsequent 7-day exposure.

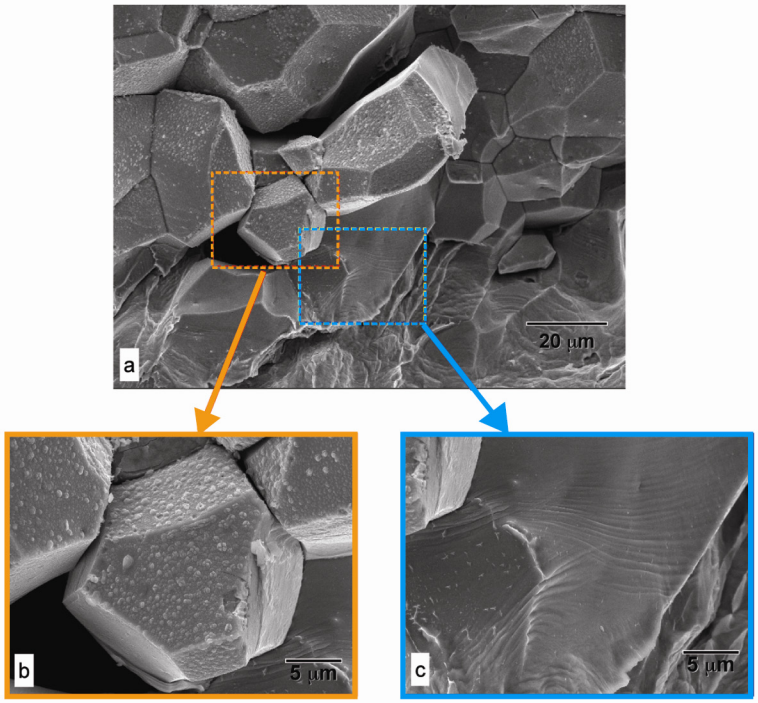

Figure 37.—Base of fracture surface for a C–103 bend specimen exposed to dilute niobium etchant solution loaded to 276 MPa (40 ksi) for 36 hr, baked at 316 °C (600 °F) for 48 hr, and exposed to >70 percent relative humidity for 7 days at room temperature. The applied bending load of 276 MPa (40 ksi) was maintained during bakeout and during subsequent 7-day exposure.

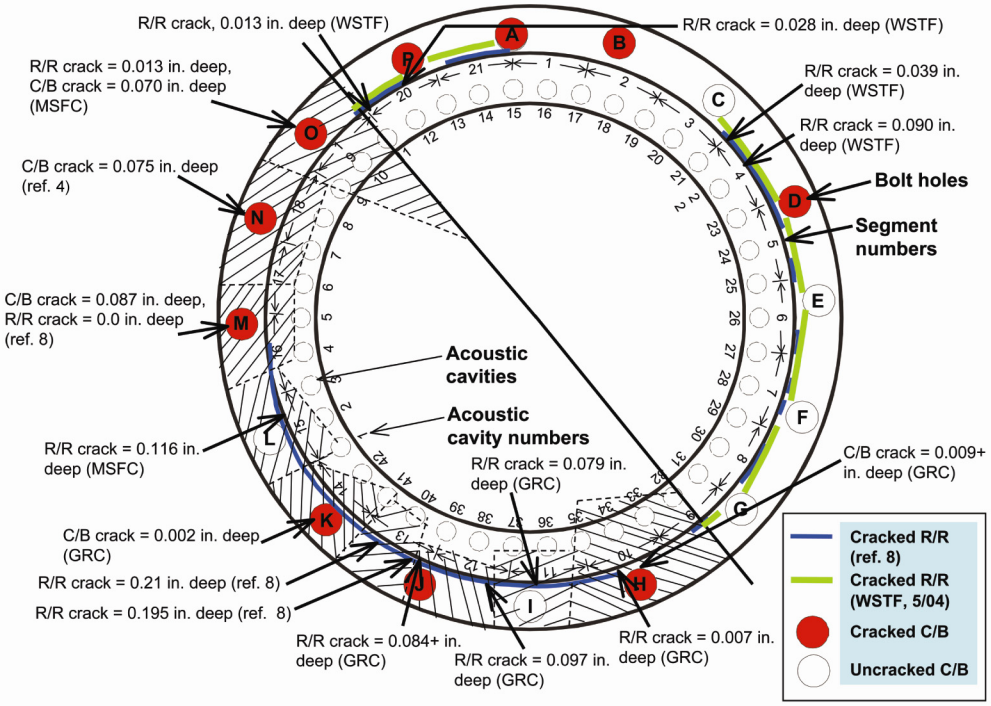

Figure 38.—Schematic diagram of S/N 120 showing approximate locations of examined sections (crosshatched) with measured depths of relief radius (R/R) and counter bore (C/B) cracking indicated. Dye penetrant indications are illustrated by the blue and green lines for R/R cracking and by the red circles for C/B cracking.

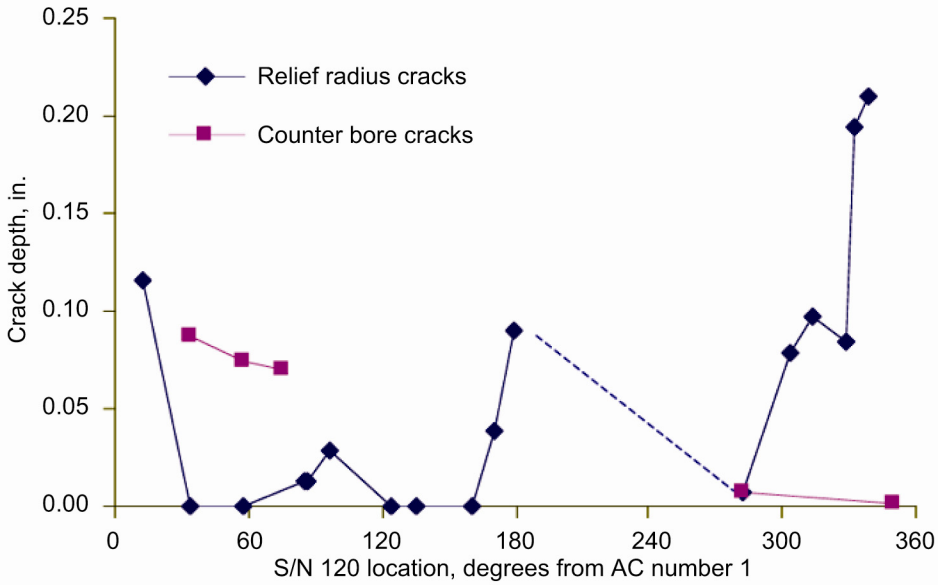

Figure 39.—Depth of cracking in relief radius and counter bores is measured as a function of location in serial number (S/N) 120. Location is given as the number of degrees from acoustic cavity (AC) number 1 shown in figure 38.

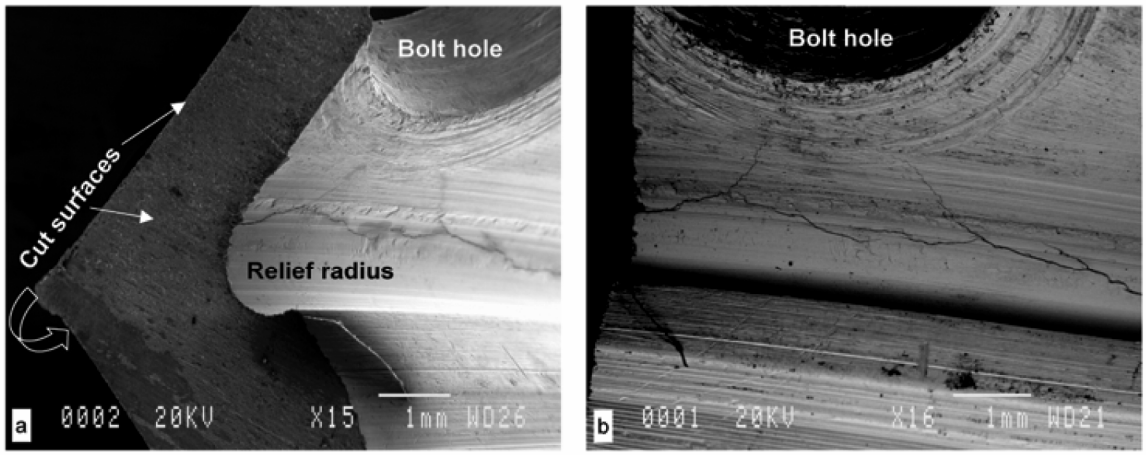

Figure 40.—Relief radius cracking observed in section of S/N 120 near bolt hole J. (a) Low magnification image showing proximity of relief radius to bolt hole. (b) Multiple cracks observed in relief radius.

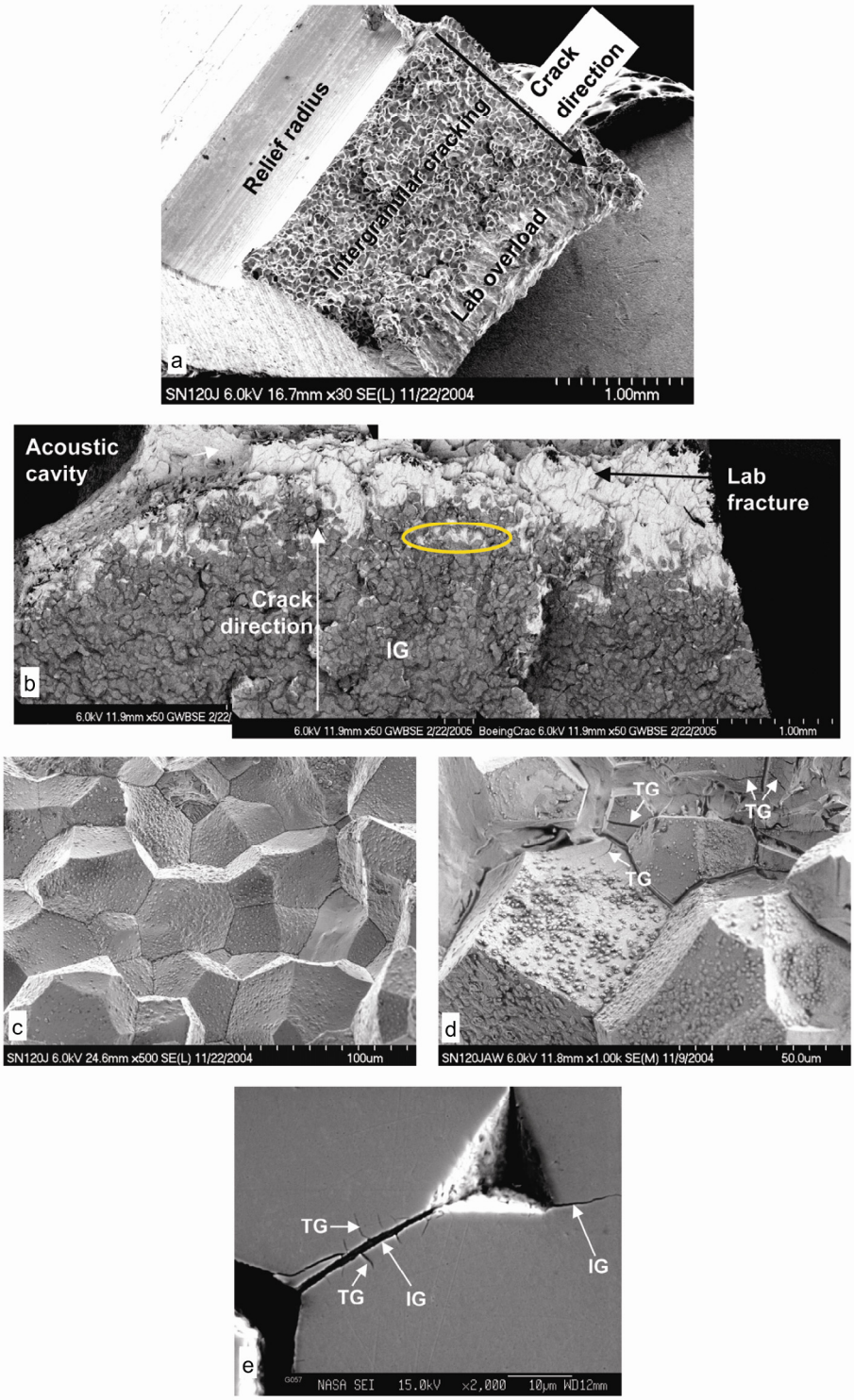

Figure 41.—(a) Overall view showing relief radius, intergranular (IG) cracking, and lab overload area for small section of S/N 120 between bolt holes I and J. (b) Montage of backscattered electron images for another section of S/N 120 having a deeper IG crack between bolt holes J and K. Relief radius is not shown in montage. (c) Higher magnification view showing IG and products on fracture surface. (d) Products are evident on some grain facets of the predominantly IG fracture. Examples of transgranular cracking (TG) were also observed and are indicated by the white arrows. (e) TG was also evident in polished sections of S/N 120, which demonstrates that their presence was not associated with lab openings of fracture surfaces.

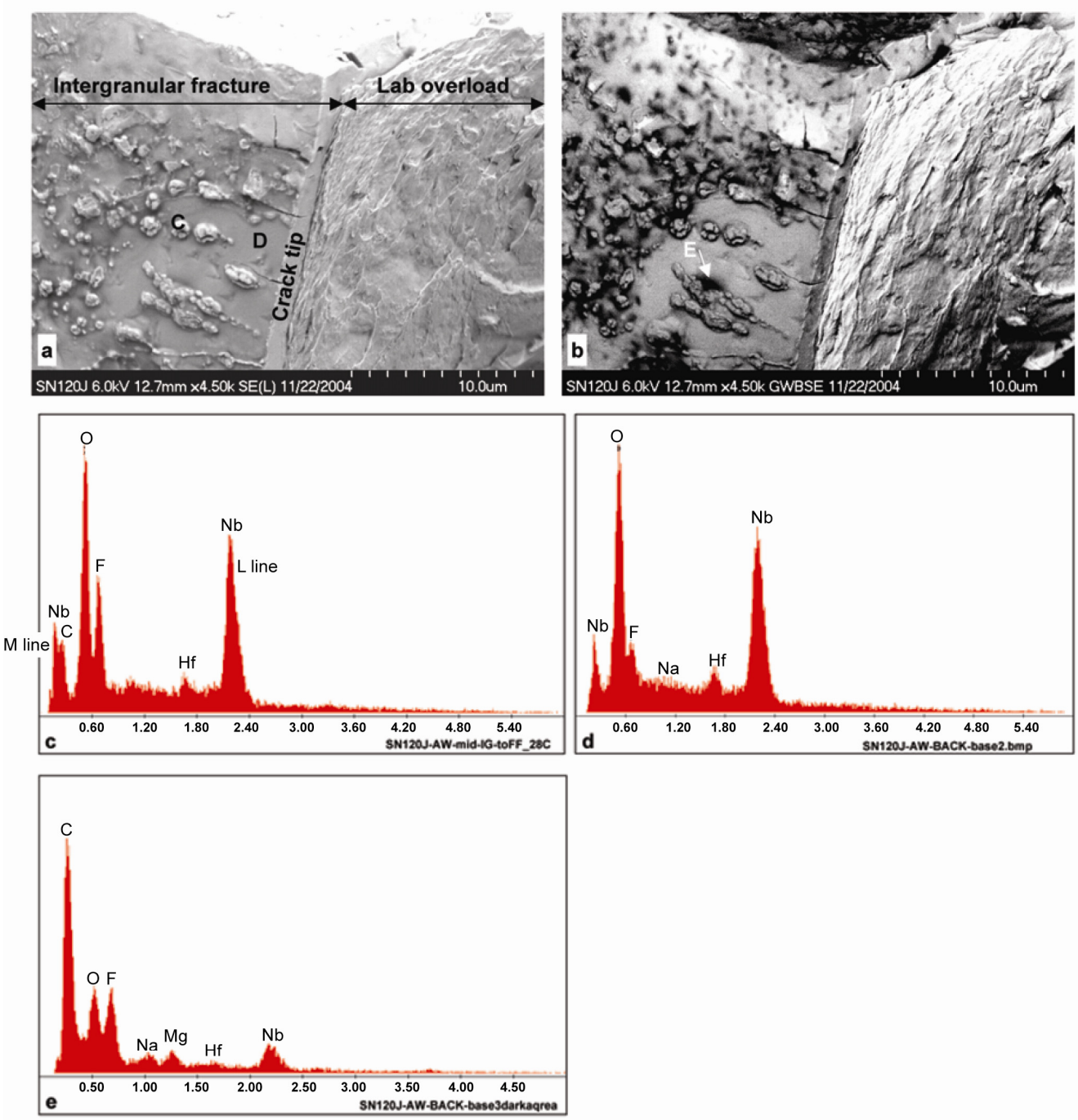

Figure 42.—S/N 120 fracture surface at the tip of the intergranular relief radius crack between bolt holes I and J. Lab overload region is also shown. Reaction products and possible contaminants are evident on the fracture surface. (a) Secondary electron image showing selected areas C and D for Energy Dispersive Spectroscopy (EDS) scans. (b) Backscattered electron image of the same region showing atomic number differences of the features present; darker regions contain lower atomic number elements. Selected area E is shown for EDS scan. Representative EDS scans for (c) popcorn, area C; (d) bright region of oxidized crack surface, area D; and (e) dark region on intergranular crack, area E.

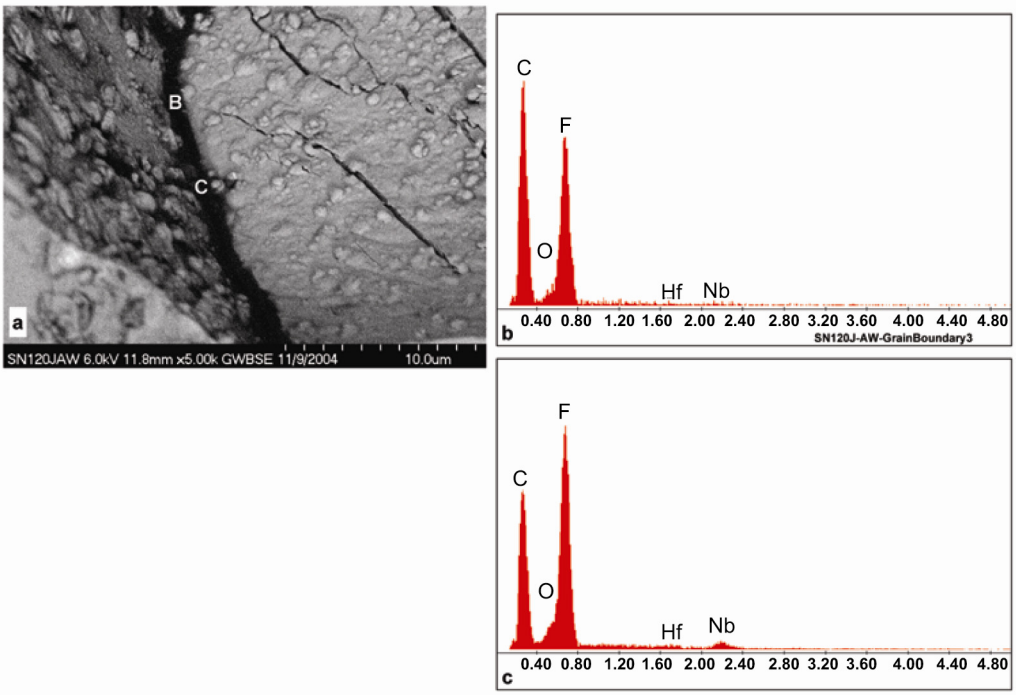

Figure 43.—Carbon and fluorine-rich material was found in numerous dark areas on the S/N 120 fracture surface. (a) Trough along a grain boundary is shown in backscattered electron image. Energy dispersive spectroscopy scans are shown for the dark material in (b) area B and (c) area C.

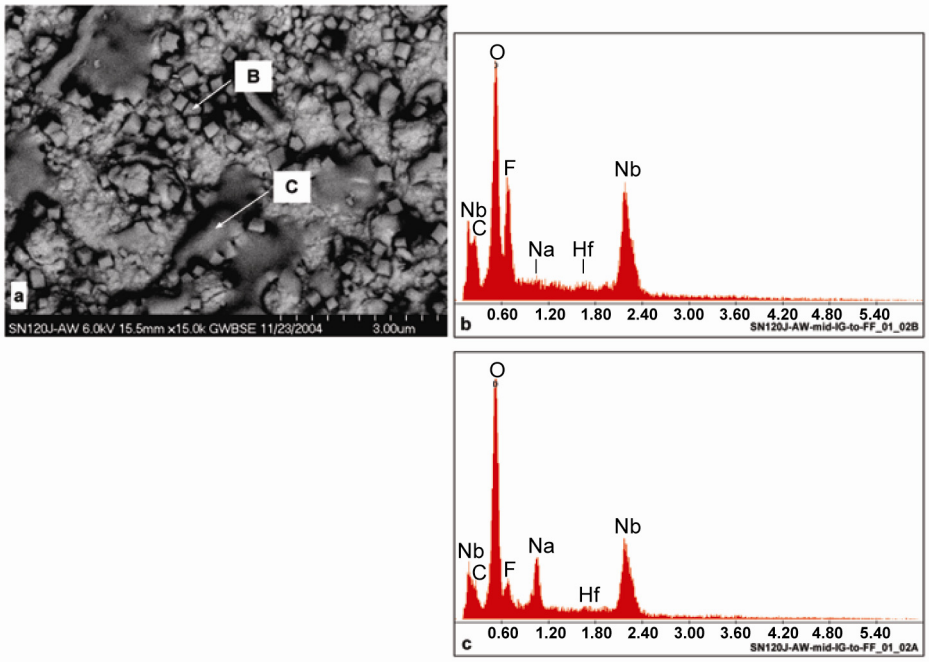

Figure 44.—S/N 120 fracture surface in an isolated region of the crack mouth for relief radius crack between bolt holes I and J. Reaction products and possible contaminants are evident on the fracture surface. (a) Backscattered electron image showing cubic-shaped products at “B” and “mud-flat” areas at “C.” Energy Dispersive Spectroscopy scans are shown for features in (b) area B and (c) area C.

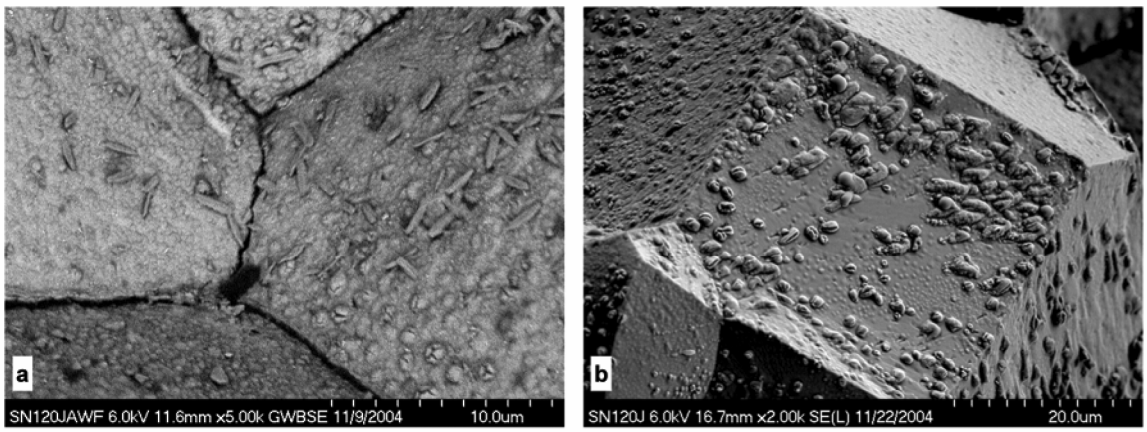

Figure 45.—Intergranular fracture surface from S/N 120 showing (a) acicular products and popcorn-like nodules and (b) popcorn-like nodules, uncracked rounded particles, elongated clusters, and small bumps.

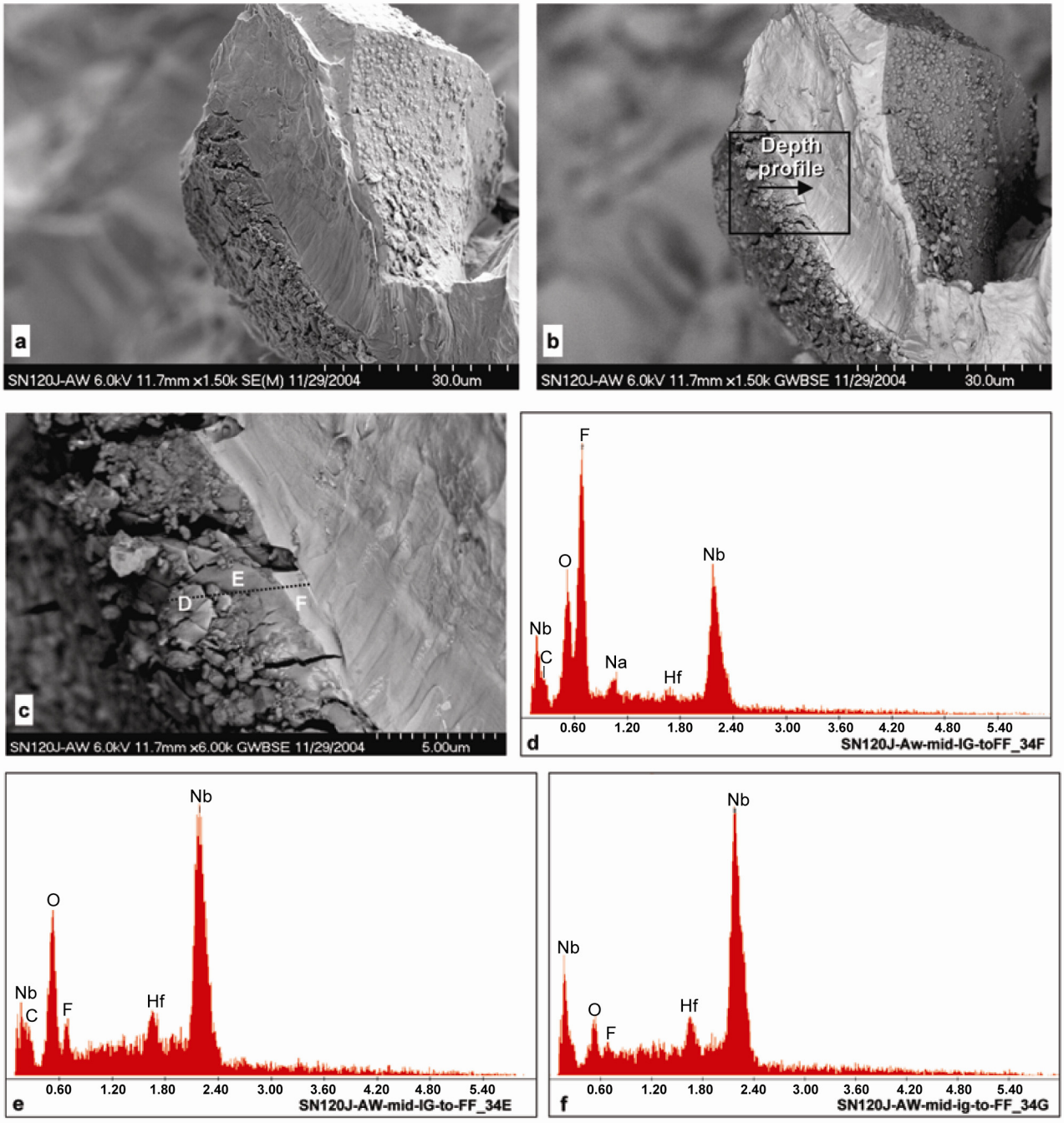

Figure 46.—Grain on S/N 120 fracture surface used for depth profiling through the oxide scale from the top of the intergranular surface down to the newly exposed C–103. The grain boundaries around this grain were cracked nearly all the way around, except for one remaining ligament, which kept the grain attached to the opened fracture surface. (a) Secondary electron image showing topography of uniquely positioned grain. (b) Backscattered electron (BSE) image showing topography and atomic number differences between various features. Here the freshly exposed C–103 is lighter in color than the oxidized scale on the intergranular surface. (c) Higher magnification BSE image of oxide scale with locations D, E, and F shown for Energy Dispersive Spectroscopy scans in (d), (e), and (f), respectively.

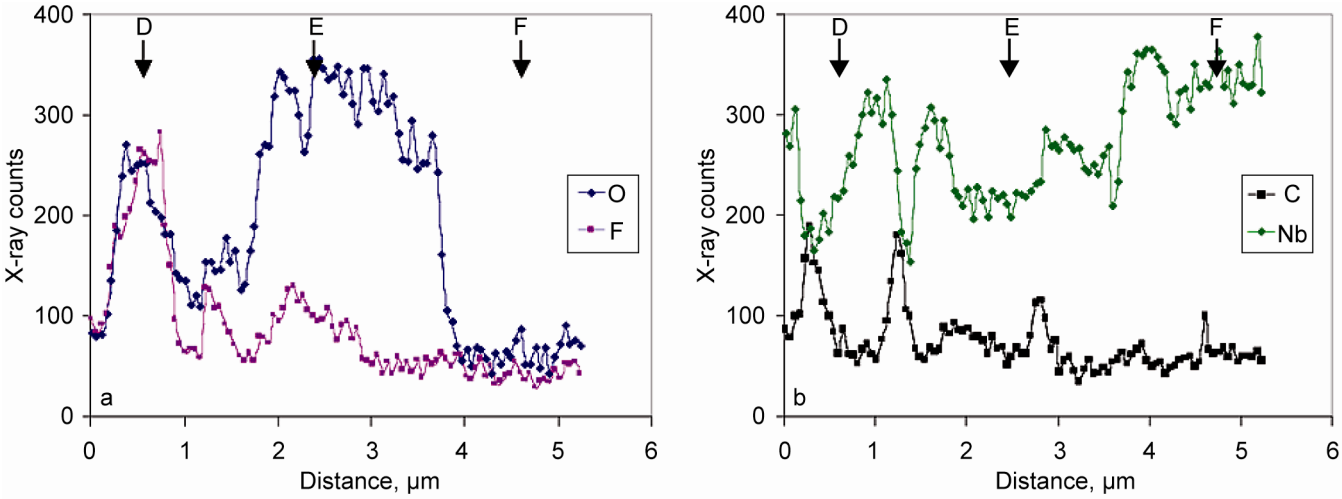

Figure 47.—X-ray line scans showing depth profiling through the oxide scale in figure 46(c). (a) Oxygen and fluorine counts and (b) carbon and niobium counts are shown as a function of distance from the surface inward to the C–103 substrate. The approximate distances for locations D, E, and F from figure 46(c) are also shown for reference.

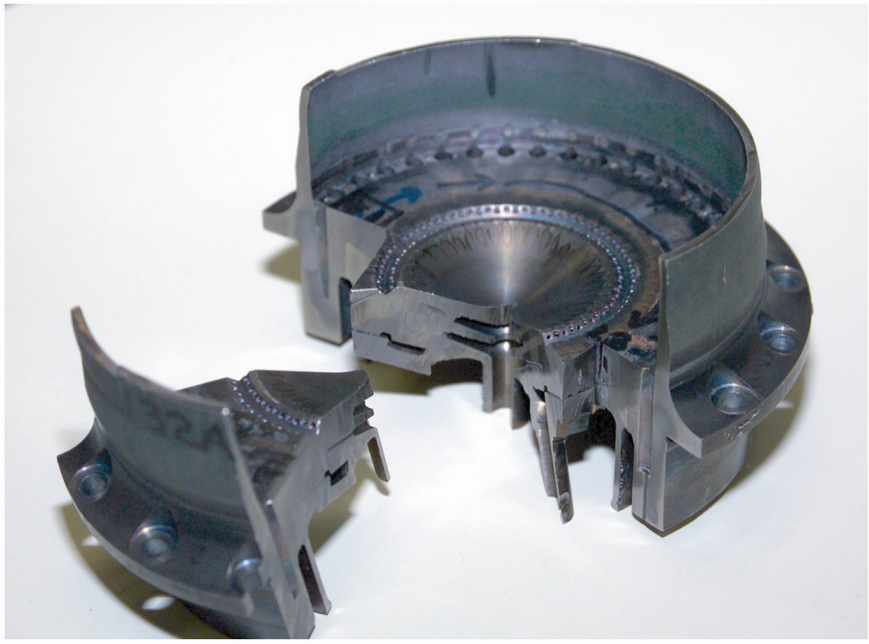

Figure 48.—Two sections of S/N 132 that were used for the destructive analysis are shown. The smaller piece was a 57° section and the large piece was a 203° section. These sections are also shown schematically in figure 49.

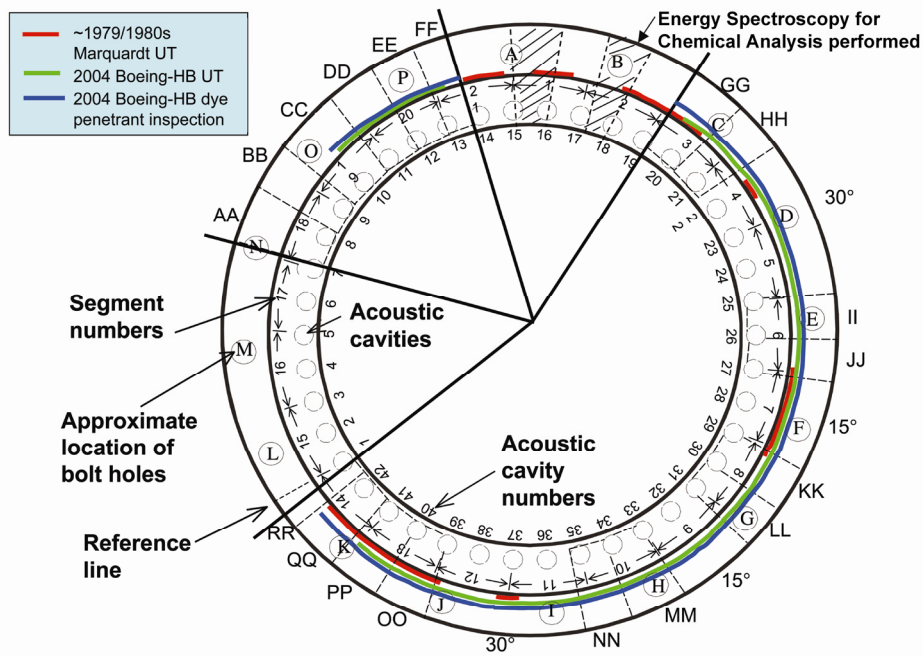

Figure 49.—Schematic diagram of S/N 132. Sections AA through RR were destructively examined by the SPRT, and two small pie-shaped pieces were examined by Boeing HB (corrected locations are indicated by cross hatching). Ultrasonic (UT) indications are shown by the red and green lines from two separate inspections, and dye penetrant indications are given by the blue lines. Two 15° and two 30° sections were left intact with the injector face for future development of nondestructive evaluation methods.

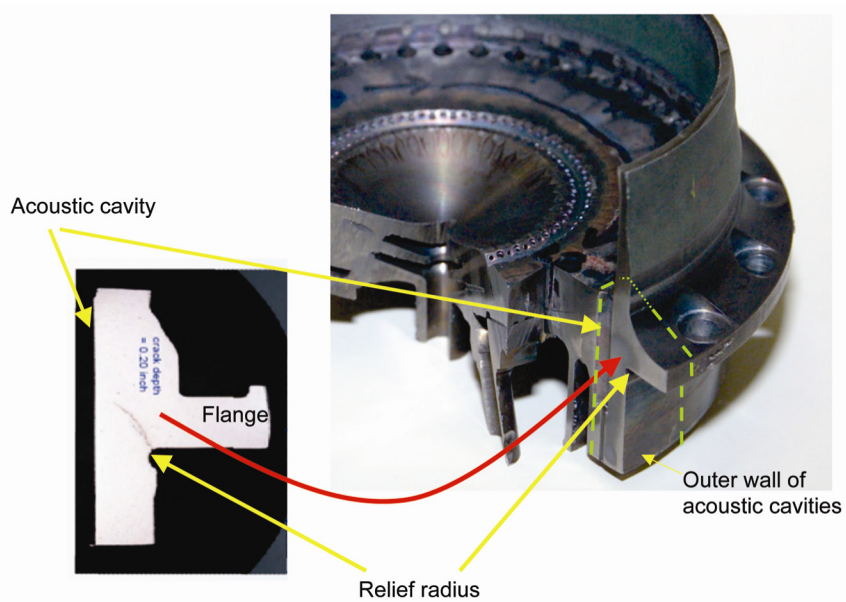

Figure 50.—Example of sectioning in S/N 132 for destructive analysis. Inset shows resultant section available for mounting and polishing for metallographic determination of crack depths.

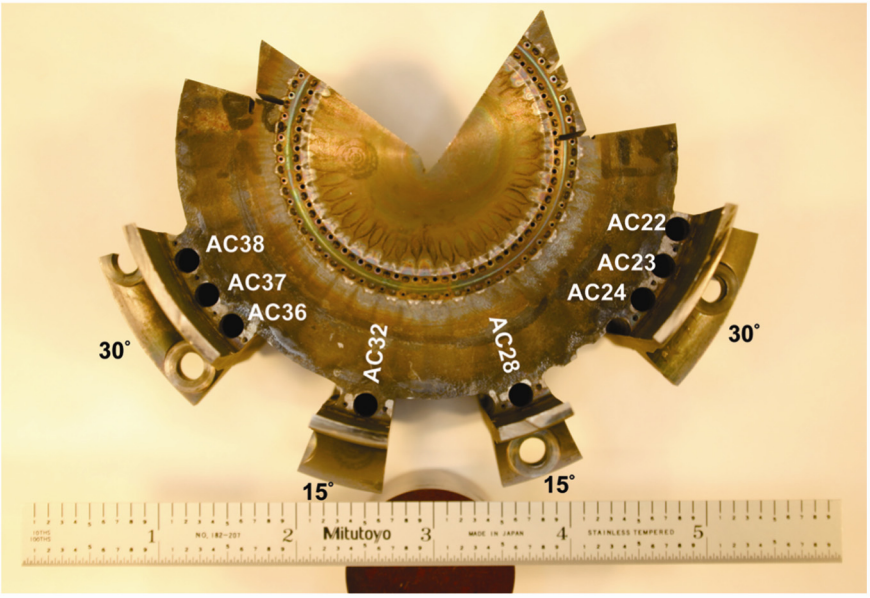

Figure 51.—The remainder of S/N 132 is shown after sectioning was completed for destructive analysis. Two 15° and two 30° sections were intentionally left intact with the injector face to facilitate subsequent development of nondestructive evaluation methods.

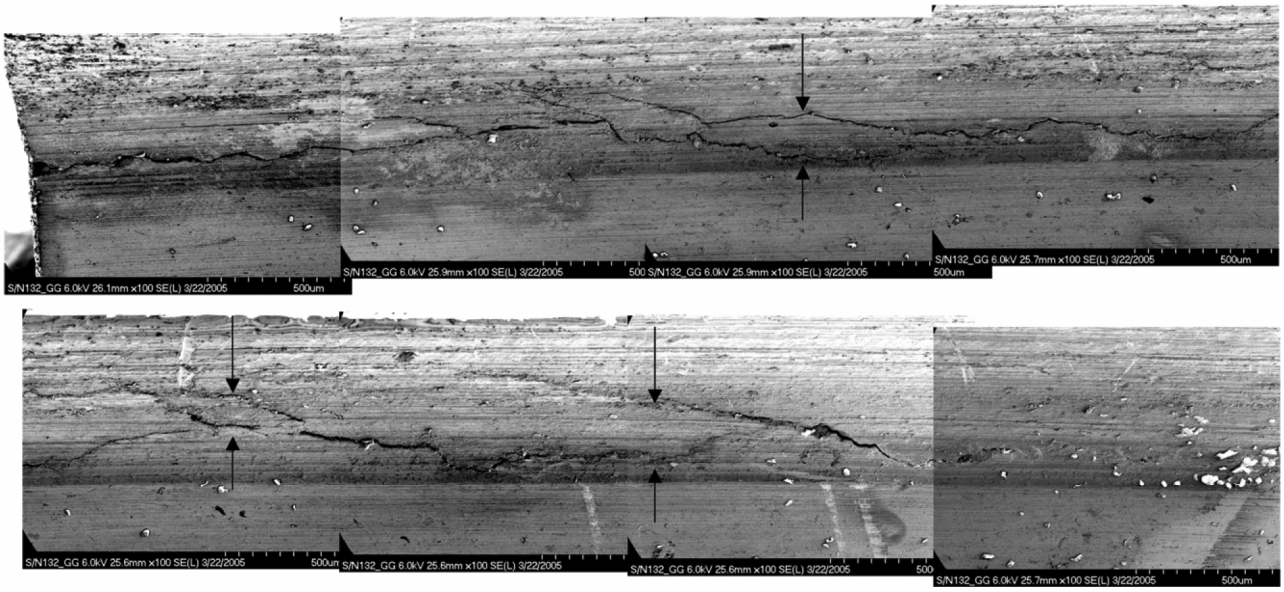

Figure 52.—Montage of scanning electron micrographs showing relief radius cracking in section GG of S/N 132. Multiple crack initiations were frequently observed. Arrows show examples of cracks running parallel to each other; if cross sections were obtained from locations at arrows, then multiple cracks will become evident in those polished cross sections.

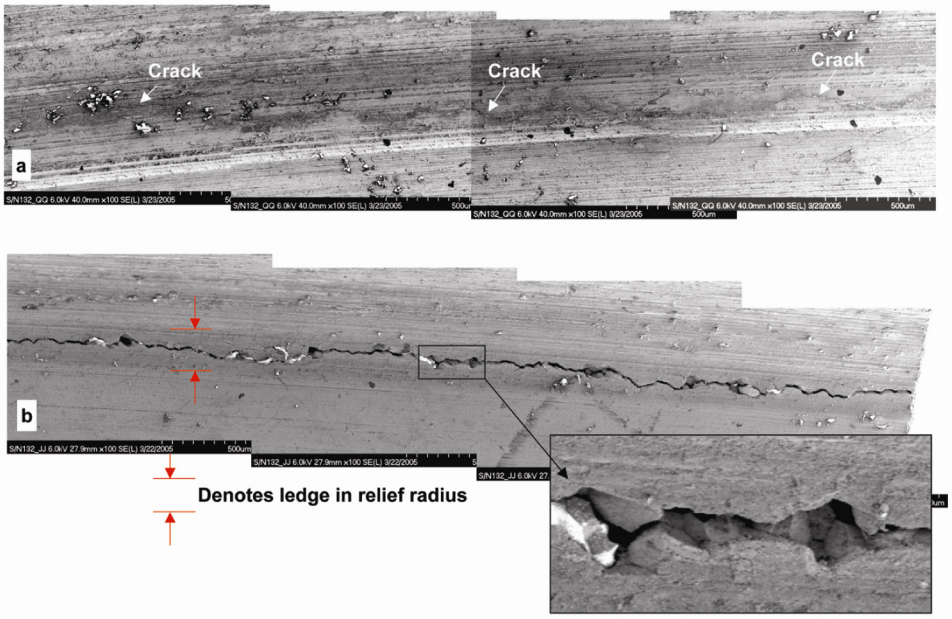

Figure 53.—Portions of S/N 132 relief radius from two different sections that show a range of tightness at the crack mouth. (a) Section QQ and (b) section JJ. Inset clearly shows intergranular cracking.

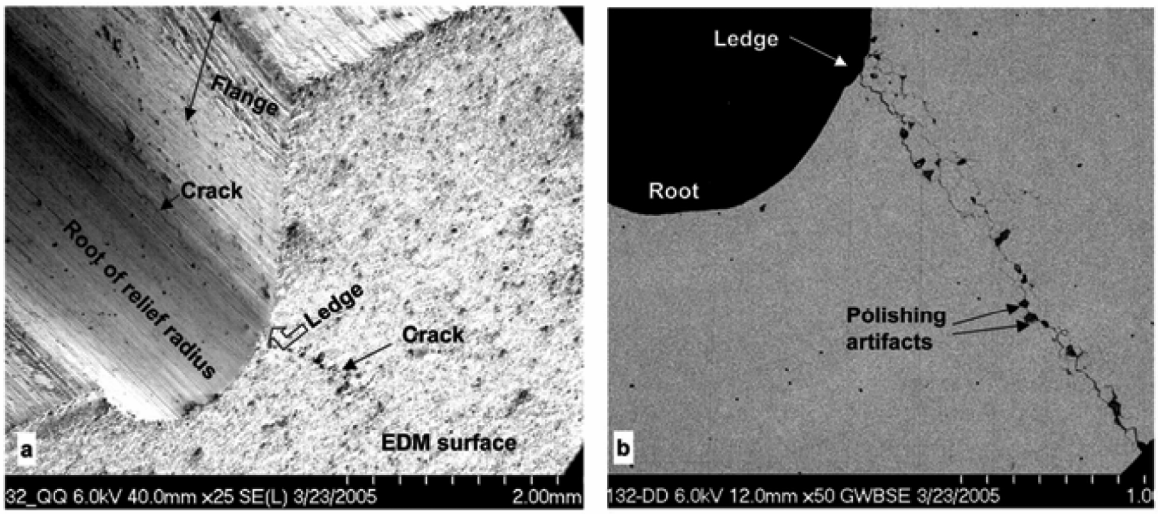

Figure 54.—Many of the relief radius cracks were initiated along a ledge in the relief radius adjacent to the injector flange. (a) Section QQ after electrodischarge machining. (b) Section DD after metallographic polishing. Polishing artifacts are present from grain pullout during metallographic preparation.

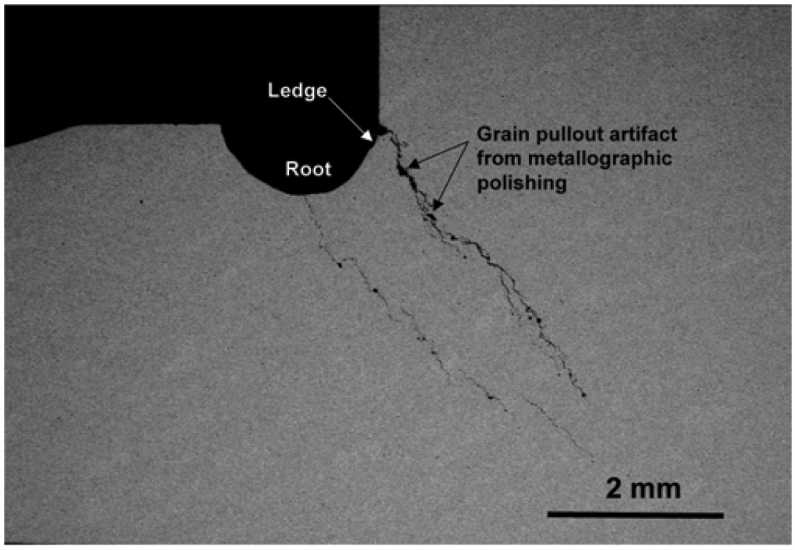

Figure 55.—Multiple cracks were observed in some polished sections. In section KK, a crack is observed to initiate along the ledge in the relief radius adjacent to the injector flange and at the base of the root of the relief radius. Polishing artifacts are present from grain pullout during metallographic preparation.

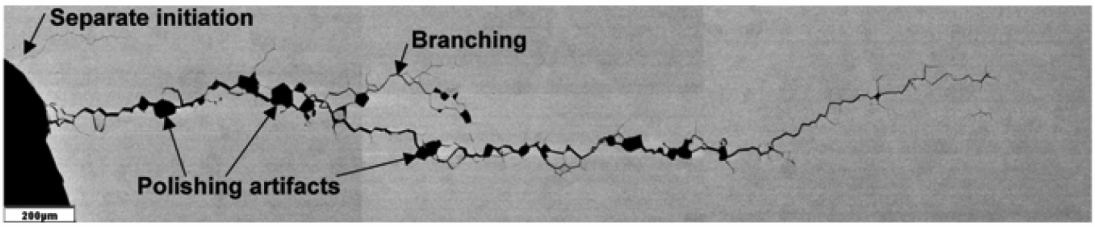

Figure 56.—Cracks were intergranular and no change in crack mode was apparent in the polished sections. Examples of separate crack initiations were observed, in addition to crack branching, in section EE. Polishing artifacts are present from grain pullout during metallographic preparation.

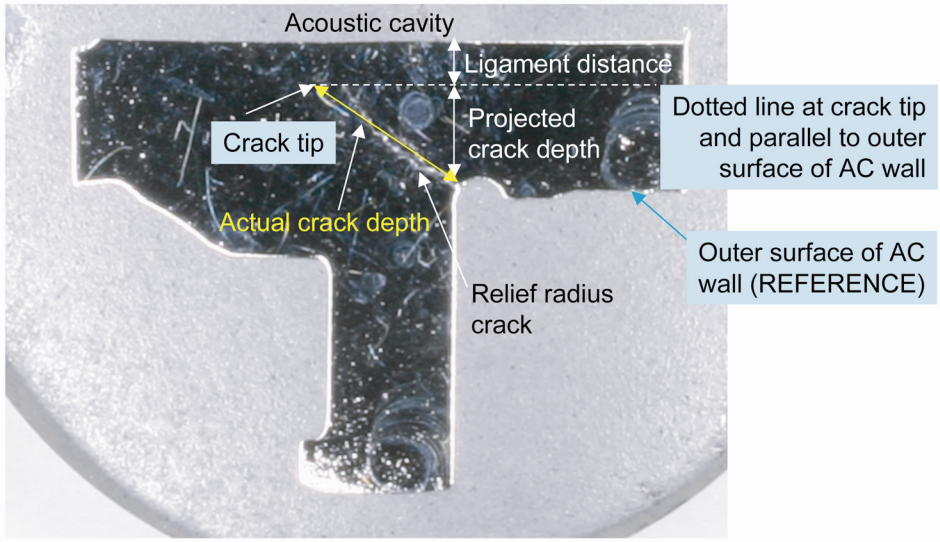

Figure 57.—Definitions of crack measurements for actual crack depth, projected crack depth, and ligament distance are indicated on a polished injector section. Angle of inclination of the crack is defined as the counterclockwise angle from outer surface of AC wall (REFERENCE) to the straight line drawn between crack mouth and crack tip.

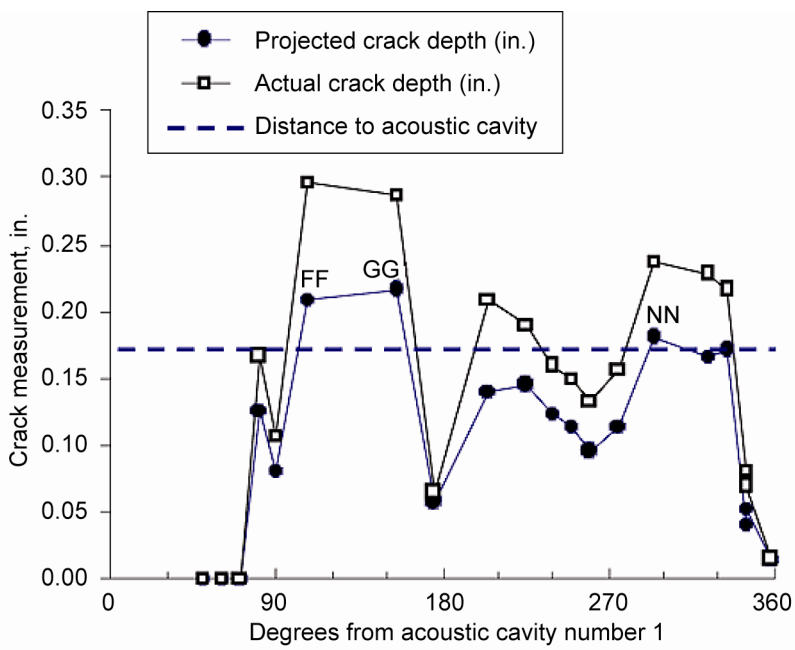

Figure 58.—Crack profile for polished cross sections from S/N 132. The crack front in sections FF, GG, and NN tunneled between two neighboring acoustic cavities, and thus had projected crack depths greater than the distance to the acoustic cavities.

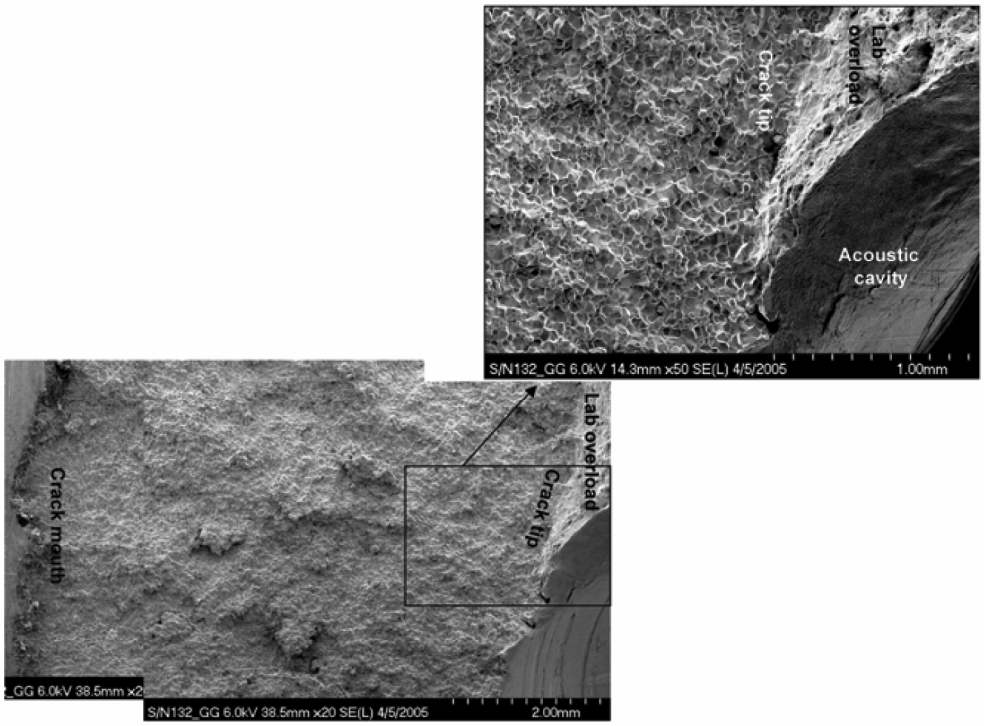

Figure 59.—Fractography confirms that the crack surface was entirely intergranular in S/N 132 with no change in crack mode from the mouth to the tip of the crack.

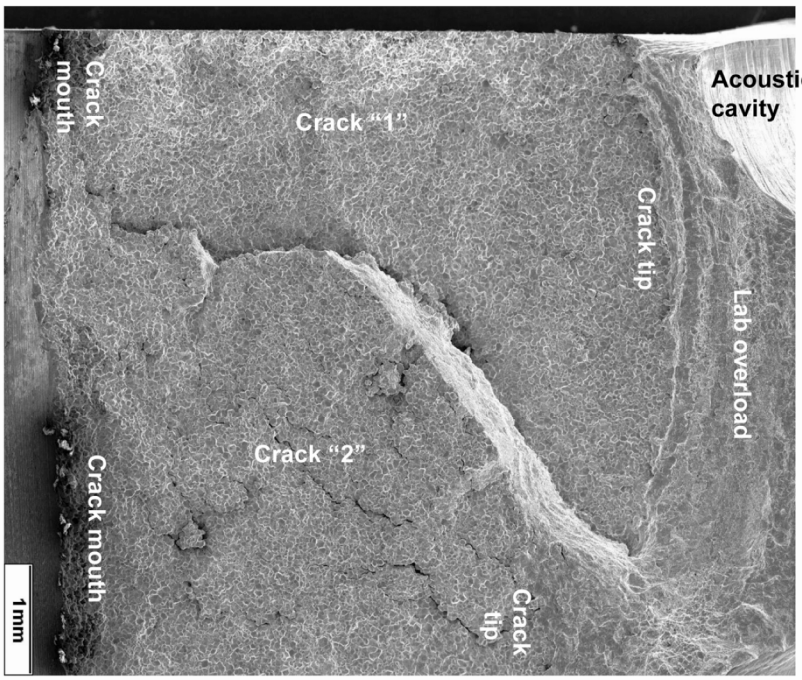

Figure 60.—Multiple cracks that initiated separately on the relief radius did not always connect subsurface to form a single crack front. Cracks are at slightly different elevations and are separated by a ductile ledge that formed during lab opening. Section II is shown for S/N 132.

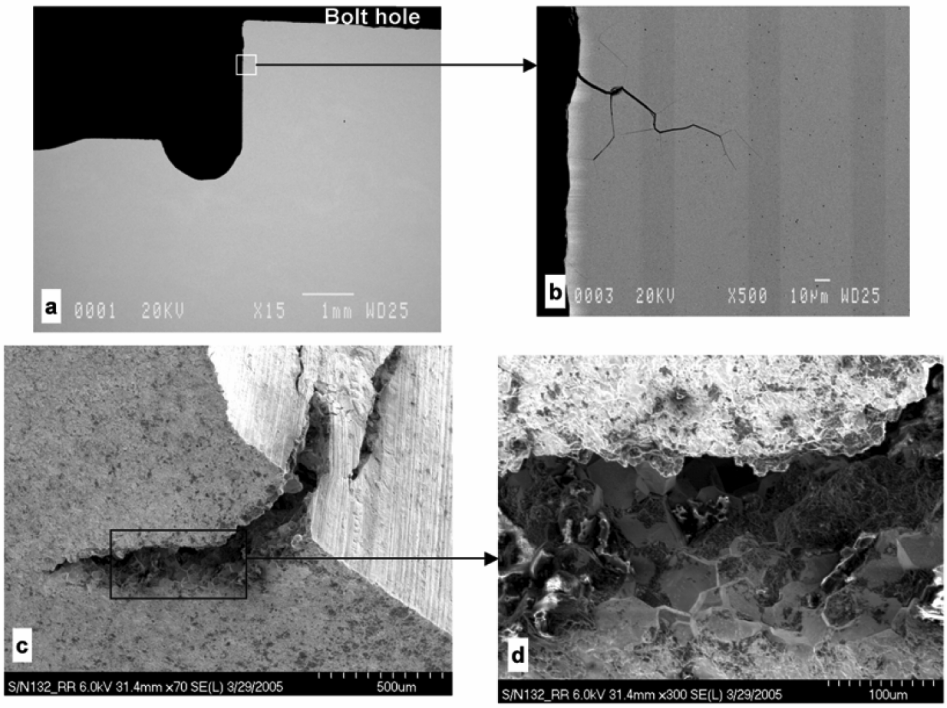

Figure 61.—Shallow intergranular cracks were occasionally observed in S/N 132 on the injector flange well outside of the relief radius region: (a) and (b) section AA after polishing; and (c) and (d) section RR after attempt to open the relief radius crack. In both cases, the intergranular cracking on the flange was only a few grains deep.

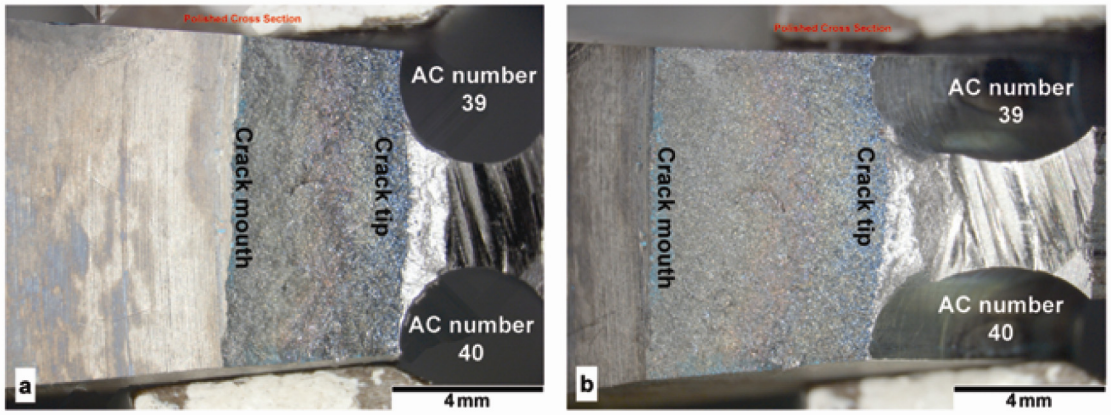

Figure 62.—Crack front in section OO extended into acoustic cavity (AC) number 39 in S/N 132, but was just short of penetrating into AC number 40. (a) Viewing axis is parallel to the AC wall. (b) Viewing axis is perpendicular to the crack face. Crack tip is seen beginning to tunnel between ACs.

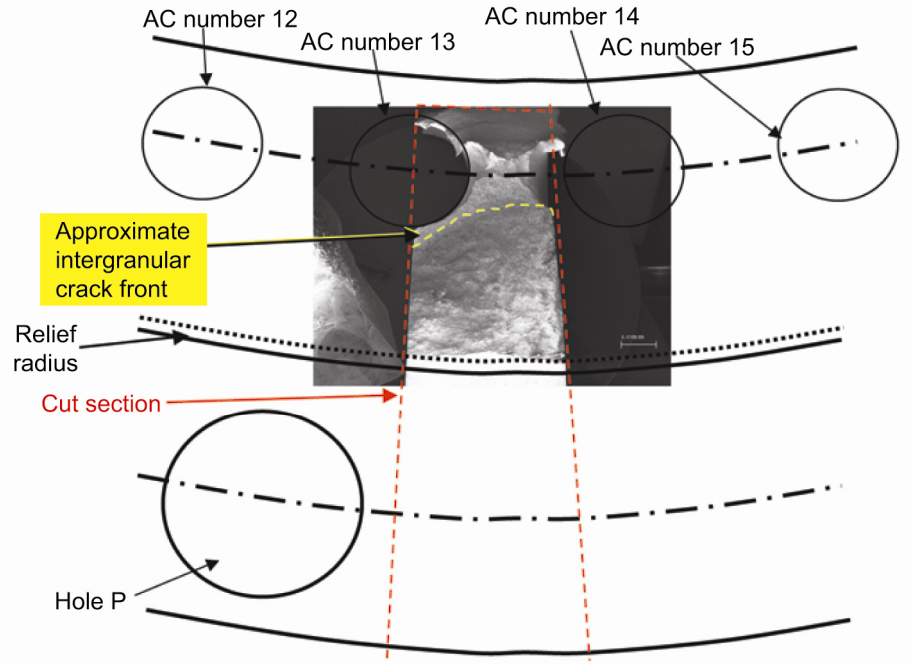

Figure 63.—Schematic of injector with superimposed photomicrograph showing the intergranular crack front in section FF of S/N 132. Crack front tunneled between neighboring acoustic cavities but did not penetrate either acoustic cavity. This clearly illustrates how the maximum crack depth can be greater than the distance from the relief radius to the acoustic cavity.

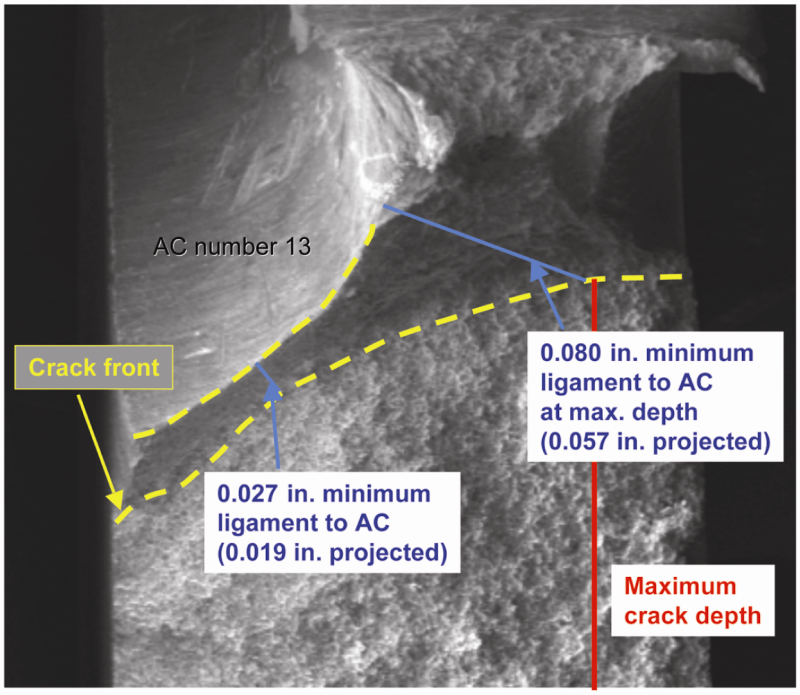

Figure 64.—Minimum ligament distances are determined on the fracture surface of section FF in S/N 132. The minimum ligament distance to the acoustic cavity (AC) is compared to the minimum ligament distance to the AC at the maximum crack depth.

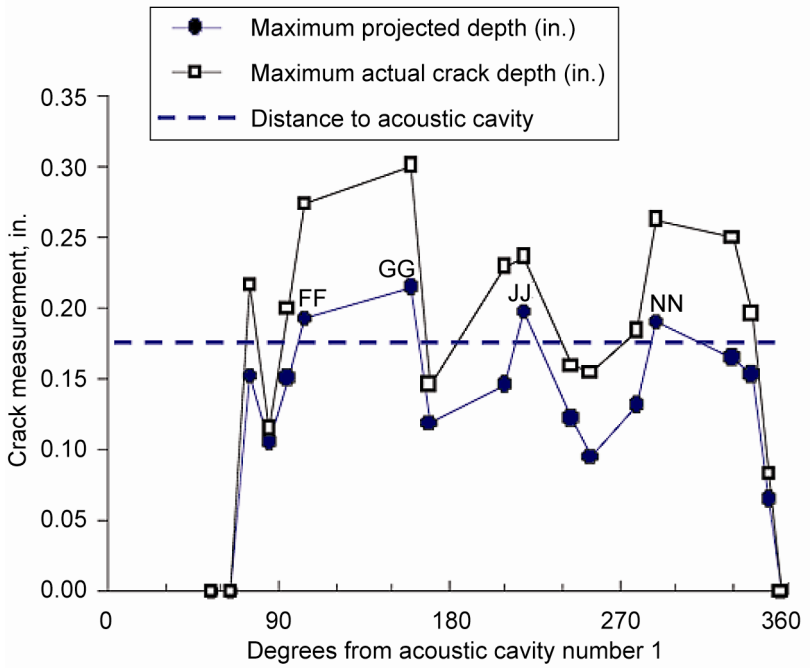

Figure 65.—Crack profile for opened crack faces from S/N 132. The crack front in sections FF, GG, JJ, and NN tunneled between two neighboring acoustic cavities, and thus had projected crack depths greater than the distance to the acoustic cavities.

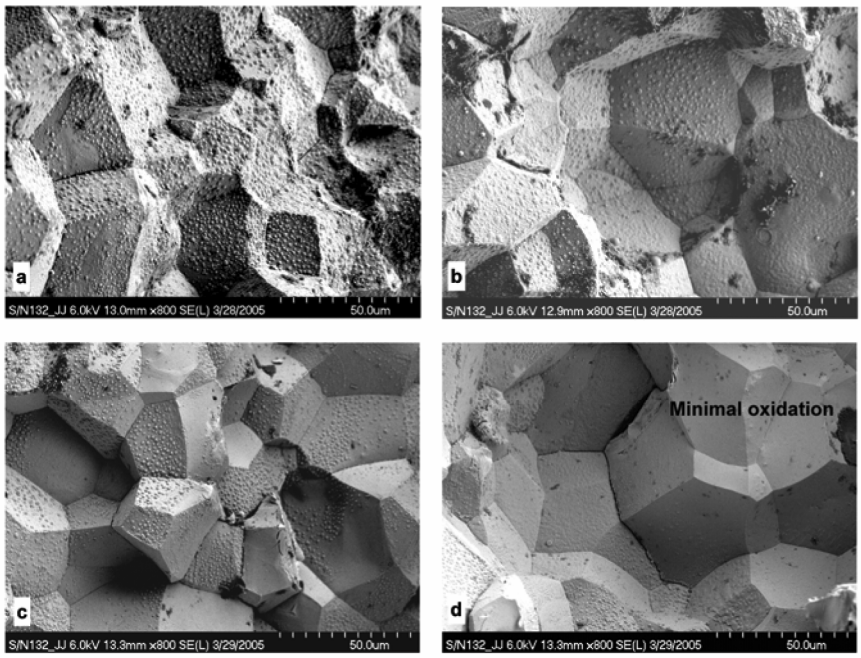

Figure 66.—Popcorn oxidation was typically observed across the entire fracture surface of S/N 132; the fracture surface of section JJ is shown. (a) Crack mouth. (b) Mid-depth of crack. (c) Popcorn at the crack tip. (d) “Clean” grains also observed at the crack tip.

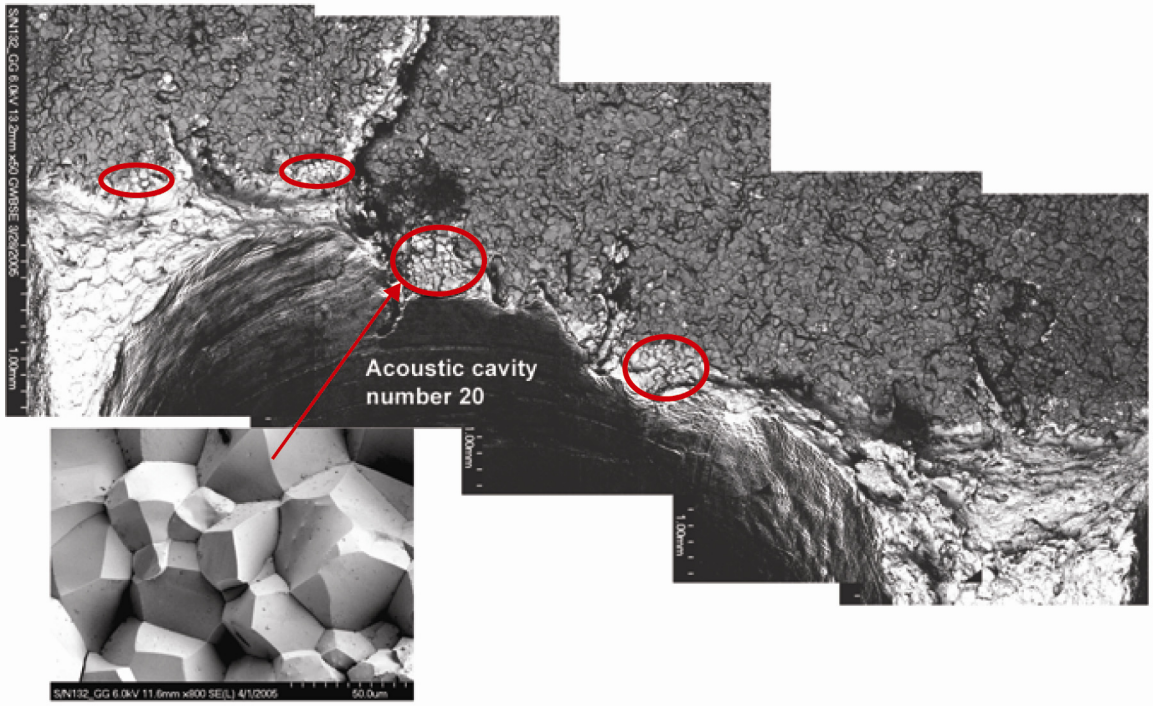

Figure 67.—Minimally oxidized grains, which showed no popcorn oxidation, were located in discrete pockets along the crack front. Typical distribution of these “clean” grains at the crack tip is indicated by the red ovals. Section GG of S/N 132 is shown here.

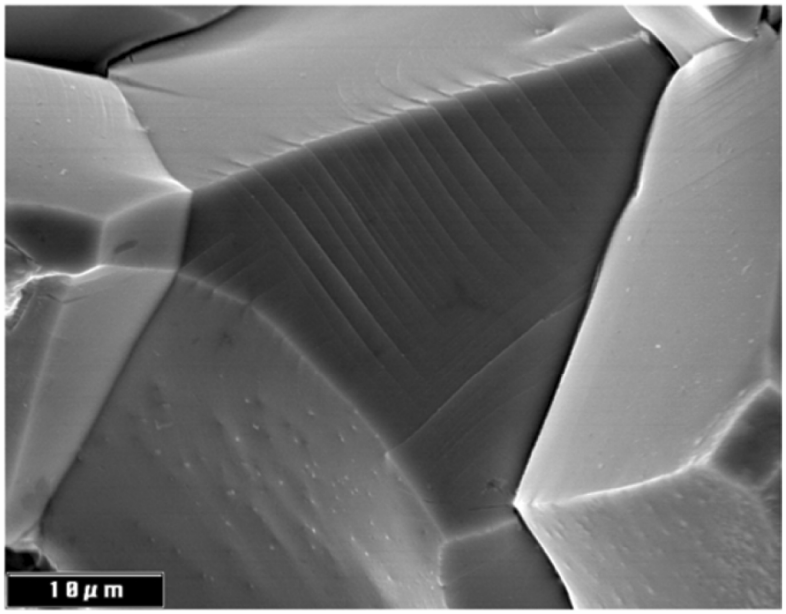

Figure 68.—Slip planes were observed on clean grain facets at the opened crack tip of section LL in S/N 132. This observation is consistent with a hydrogen embrittlement mechanism that involves slip localization due to the trapping of hydrogen at the crack tip.

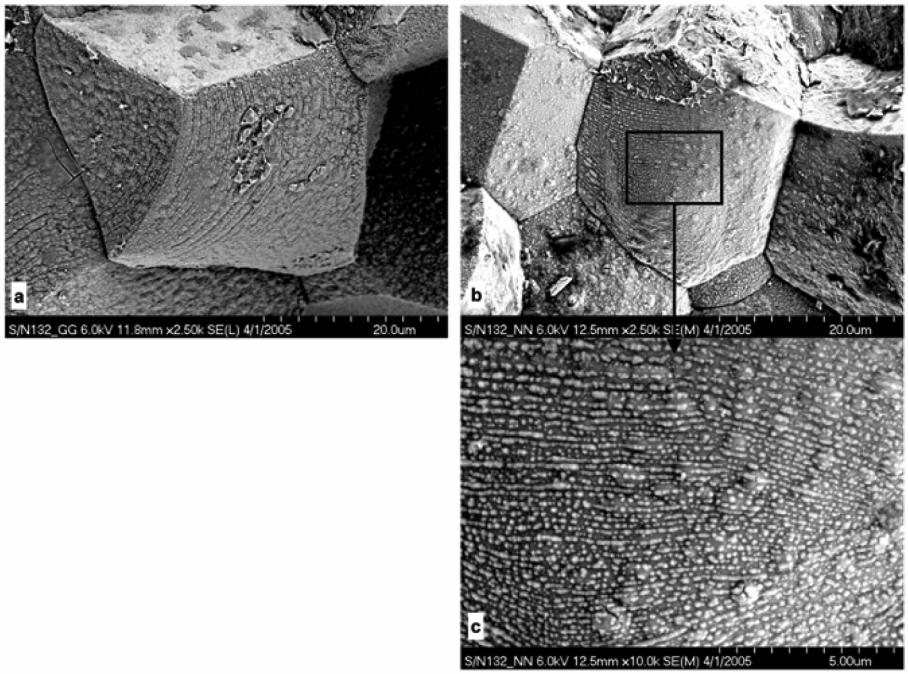

Figure 69.—Intergranular fracture surfaces of S/N 132 also contained areas where deposits had a striated appearance. This was also observed in S/N 120.

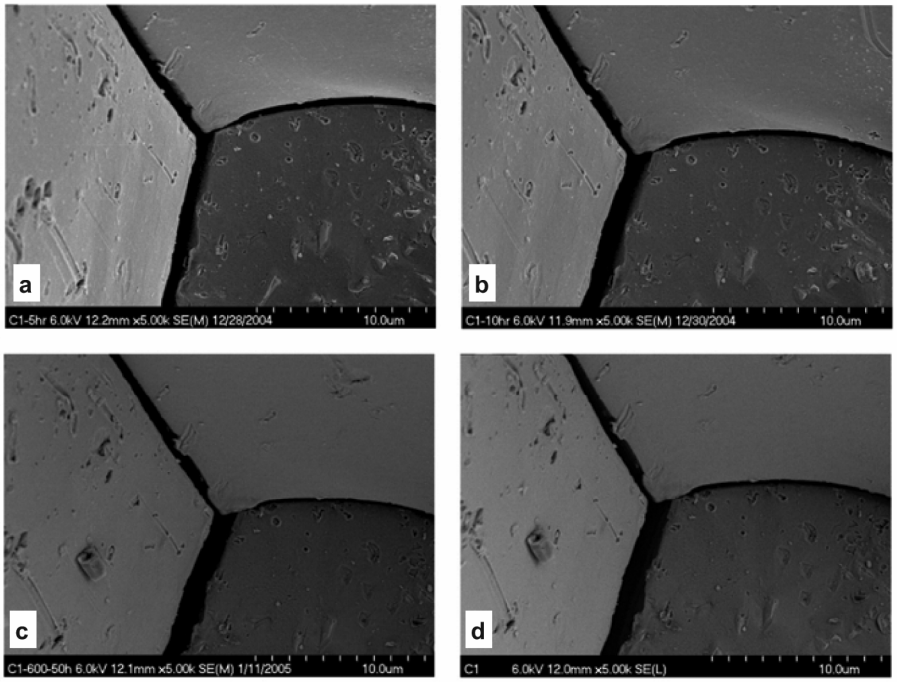

Figure 70.—Grain surfaces at triple point of C–103 fracture surfaces after 316 °C (600 °F) oxidation exposures in air for (a) 5 hr; (b) 10 hr; (c) 50 hr; and (d) 100 hr. No popcorn formation occurred.

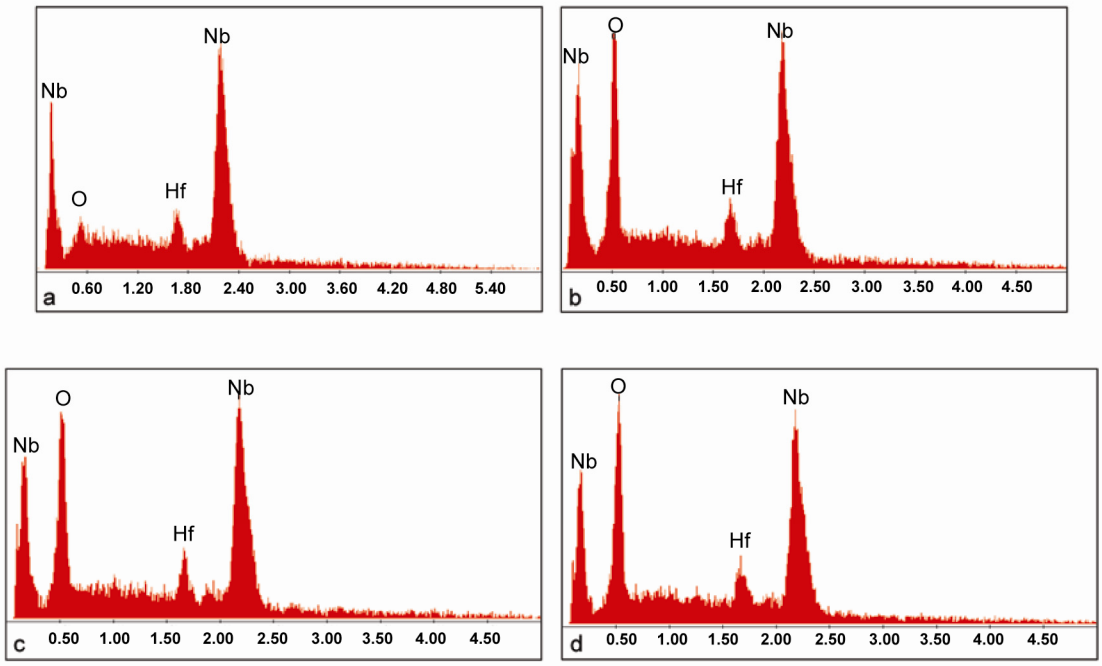

Figure 71.—Energy Dispersive Spectroscopy for 316 °C (600 °F) oxidation of C–103 intergranular fracture surfaces as a function of time: (a) 0 hr; (b) 10 hr; (c) 50 hr; and (d) 100 hr. The biggest change in oxygen peak is evident after 10 hr.

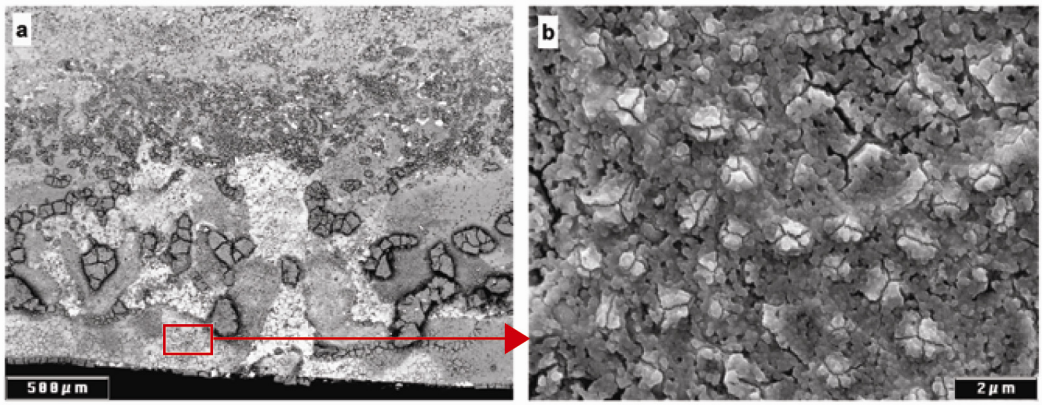

Figure 72.—Polished C–103 specimen was exposed to HF-containing etchant, which was then entrapped between another piece of C–103 and allowed to dry overnight. The C–103 “sandwich” was heated in air to 316 °C (600 °F) for 24 hr and then separated for examination: (a) C–103 surface showing various surface reaction products; and (b) popcorn features present in rectangle near specimen edge.

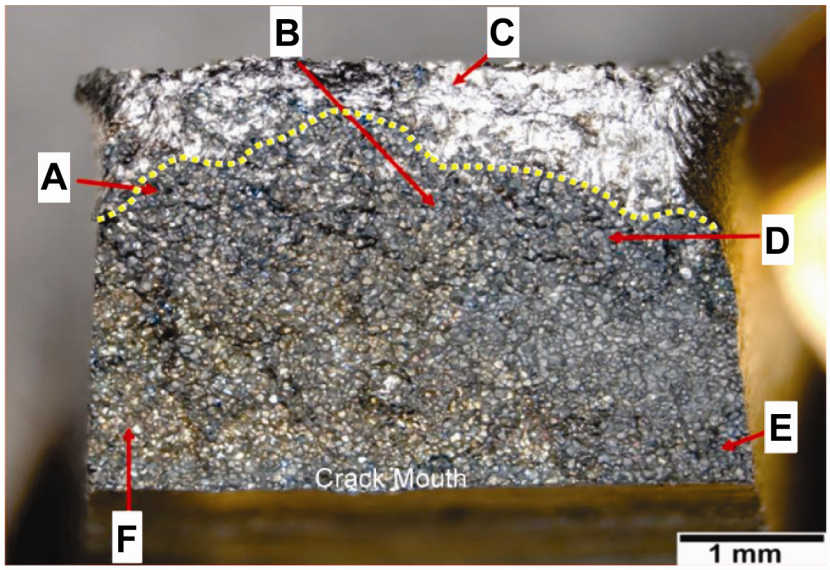

Figure 73.—Intergranular crack from relief radius of hole L from S/N 120. Locations A through F indicate the areas where Electron Spectroscopy for Chemical Analysis was performed. The bright areas near C represent the lab overload region, whereas the duller gray and brown regions represent the intergranular crack surface. Dotted line represents the approximate location for the crack tip.

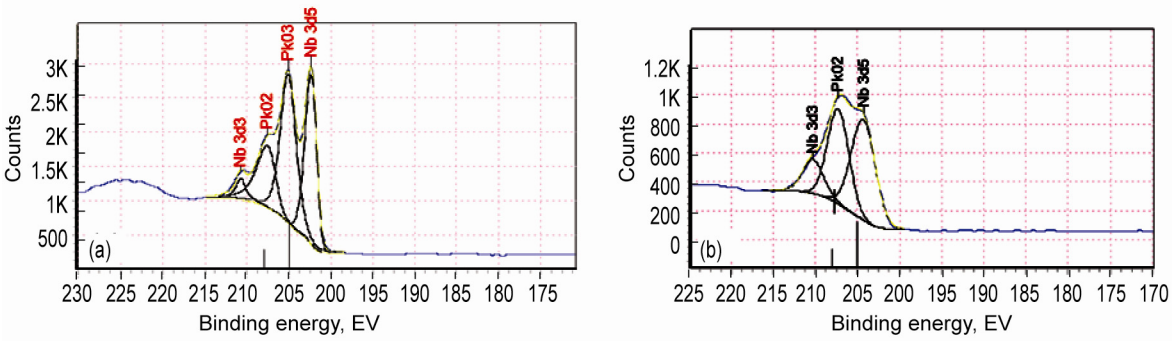

XPS Line	Adj'ed Be	CrossSec	Norm Area	Atom %
Nb 3d3	210.675	3.35	30.398	16.249
Nb 3d5	202.336	4.86	156.675	83.751

XPS Line	Adj'ed Be	CrossSec	Norm Area	Atom %
Nb 3d3	210.273	3.35	39.238	30.794
Nb 3d5	204.303	4.86	88.185	69.206

Figure 74.—Electron Spectroscopy for Chemical Analysis spectra obtained from intergranular crack region from relief radius of hole L from S/N 120. Niobium region only is shown in (a) spectra from the lab overload at location C from figure 73 and (b) representative spectra of intergranular crack surface from locations A and B and D to F from figure 73.

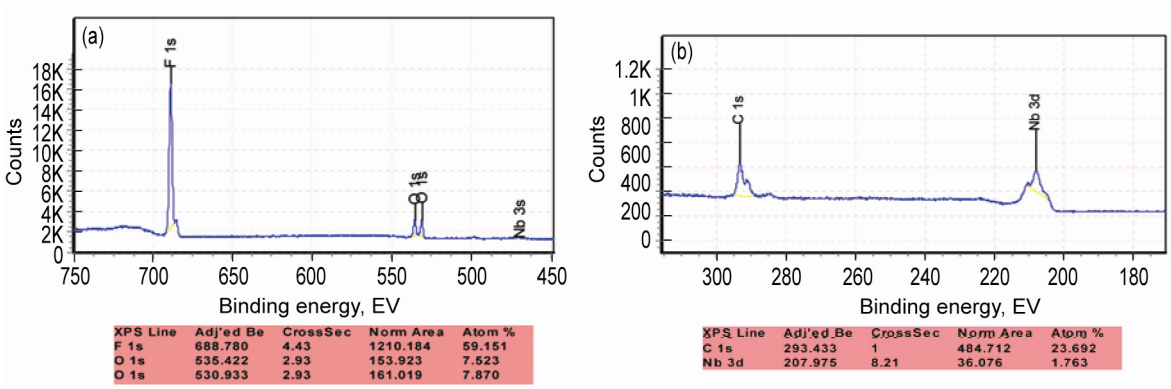

Figure 75.—Typical Electron Spectroscopy for Chemical Analysis spectra obtained from intergranular crack surface in relief radius near hole L from S/N 120. (a) Spectra containing fluorine (F), oxygen (O), and niobium (Nb) peaks. The left peaks of F and O are from Krytox (DuPont, Wilmington, DE) and the right peaks of F and O are from NbO_2F. (b) Spectra containing C and Nb peaks. The two left C peaks are from Krytox and the right C peak is from contamination. The three unresolved Nb peaks are from Nb oxides.

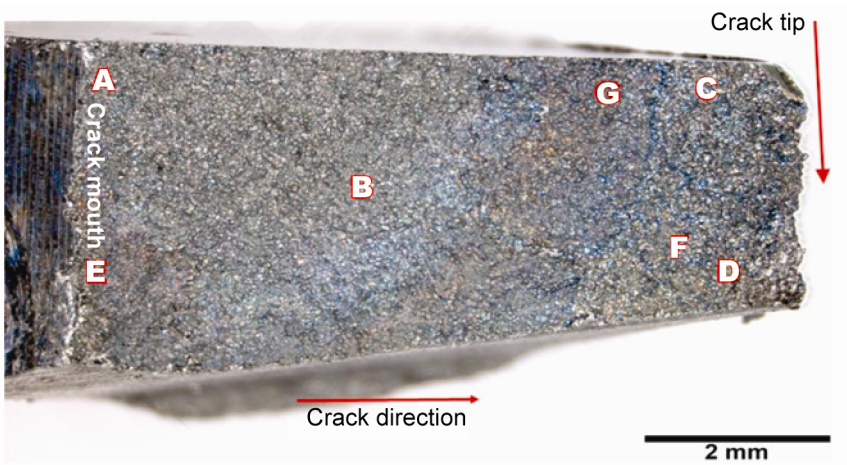

Figure 76.—Fracture surface of relief radius crack near bolt hole B and between acoustic cavity numbers 17 and 18 from S/N 132. (Note, ref. 48 incorrectly identifies this section as being near acoustic cavity number 16.) Locations A through G indicate areas where electron spectroscopy for chemical analysis was performed.

REPORT DOCUMENTATION PAGE

Form Approved
OMB No. 0704-0188

Public reporting burden for this collection of information is estimated to average 1 hour per response, including the time for reviewing instructions, searching existing data sources, gathering and maintaining the data needed, and completing and reviewing the collection of information. Send comments regarding this burden estimate or any other aspect of this collection of information, including suggestions for reducing this burden, to Washington Headquarters Services, Directorate for Information Operations and Reports, 1215 Jefferson Davis Highway, Suite 1204, Arlington, VA 22202-4302, and to the Office of Management and Budget, Paperwork Reduction Project (0704-0188), Washington, DC 20503.

1. AGENCY USE ONLY (*Leave blank*)

2. REPORT DATE
December 2005

3. REPORT TYPE AND DATES COVERED
Technical Paper

4. TITLE AND SUBTITLE
Reaction Control System Thruster Cracking Consultation: NASA Engineering and Safety Center (NESC) Materials Super Problem Resolution Team (SPRT) Findings

5. FUNDING NUMBERS
WBS 843515.02.01.03.03.01.07

6. AUTHOR(S)
Rebecca A. MacKay, Stephen W. Smith, Sandeep R. Shah, and Robert S. Piascik

7. PERFORMING ORGANIZATION NAME(S) AND ADDRESS(ES)
National Aeronautics and Space Administration
John H. Glenn Research Center at Lewis Field
Cleveland, Ohio 44135–3191

8. PERFORMING ORGANIZATION REPORT NUMBER
E–15410

9. SPONSORING/MONITORING AGENCY NAME(S) AND ADDRESS(ES)
National Aeronautics and Space Administration
Washington, DC 20546–0001

10. SPONSORING/MONITORING AGENCY REPORT NUMBER
NASA TP—2005-214053

11. SUPPLEMENTARY NOTES
Rebecca A. MacKay, NASA Glenn Research Center; Stephen W. Smith, NASA Langley Research Center; Sandeep R. Shah, NASA Marshall Space Flight Center; and Robert S. Piascik, NASA Engineering and Safety Center, NASA Langley Research Center. Responsible person, Rebecca A. MacKay, organization code RX, 216–433–3269.

12a. DISTRIBUTION/AVAILABILITY STATEMENT
Unclassified - Unlimited
Subject Category: 26
Available electronically at http://gltrs.grc.nasa.gov
This publication is available from the NASA Center for AeroSpace Information, 301–621–0390.

12b. DISTRIBUTION CODE

13. ABSTRACT ***(Maximum 200 words)***

The shuttle orbiter's reaction control system (RCS) primary thruster serial number 120 was found to contain cracks in the counter bores and relief radius after a chamber repair and rejuvenation was performed in April 2004. Relief radius cracking had been observed in the 1970s and 1980s in seven thrusters prior to flight; however, counter bore cracking had never been seen previously in RCS thrusters. Members of the Materials Super Problem Resolution Team (SPRT) of the NASA Engineering and Safety Center (NESC) conducted a detailed review of the relevant literature and of the documentation from the previous RCS thruster failure analyses. It was concluded that the previous failure analyses lacked sufficient documentation to support the conclusions that stress corrosion cracking or hot-salt cracking was the root cause of the thruster cracking and lacked reliable inspection controls to prevent cracked thrusters from entering the fleet. The NESC team identified and performed new materials characterization and mechanical tests. It was determined that the thruster intergranular cracking was due to hydrogen embrittlement and that the cracking was produced during manufacturing as a result of processing the thrusters with fluoride-containing acids. Testing and characterization demonstrated that appreciable environmental crack propagation does not occur after manufacturing.

14. SUBJECT TERMS
Metals; Alloys; Niobium; Hydrogen embrittlement; Refractory metals; Testing and evaluation; Stress corrosion cracking; Corrosion; Thruster; Fractography

15. NUMBER OF PAGES
77

16. PRICE CODE

17. SECURITY CLASSIFICATION OF REPORT
Unclassified

18. SECURITY CLASSIFICATION OF THIS PAGE
Unclassified

19. SECURITY CLASSIFICATION OF ABSTRACT
Unclassified

20. LIMITATION OF ABSTRACT